TRANSMISSION OF THIN LIGHT BEAMS THROUGH TURBULENT MIXING LAYERS

Thesis by

John B. Wissler

In Partial Fulfillment of the
Requirements for the Degree of
Doctor of Philosophy

California Institute of Technology
Pasadena, California

1992

(Submitted September 6, 1991)

Acknowledgment

There are a large number of people who helped me while I was doing the research for this thesis; I could not have done it alone.

First of all, I would like to thank my advisor, Professor Anatol Roshko, for his patience, insight, and approachability. I never came out of a discussion with him feeling worse than when I went in.

Also, my thanks to Professors Don Coles and Brad Sturtevant for what later turned out to be crucial suggestions on how to do the experiments.

I want to thank George Lundgren, Phil Wood, and Larry Frazier for the timely machine shop support and the friendly advice. I owe Sharon Bryant thanks for prompt and cheerful administrative support, and for being a "TEX guru."

While every new graduate achieves his or her status by standing on the shoulders of fellow students, I have to especially thank three in particular – Greg Cardell, Dennis Moore, and Dr. Ichiro Sugioka – whose help were absolutely vital.

From my pre-Caltech life I would like to thank Lt Col (Ret) Eric Jumper of the University of Notre Dame, Dr. Mike Robinson of the University of Colorado, and Col Mike Smith of the U.S. Air Force Academy for encouraging me to pursue a Ph.D. Financial support from the U.S. Air Force, especially the Air Force Office of Scientific Research and the Phillips Laboratory for funding the research under Grant Number AFOSR-89-0552, is acknowledged.

I would like to thank my parents for always having faith in their son even though at times he did not have faith in himself.

Finally, and most of all, I would like to thank my family – Beth, my wife, and my children John A., Joey, and Laurie – for putting up with me for the last three years. It has been a hard time, and I can honestly say we are all glad it is behind us.

ABSTRACT

Light transmission through incompressible gaseous turbulent mixing layers is investigated with the objective of understanding the effects of large-scale coherent structures and mixing transition on the optical quality of the mixing layer. Experiments are done in a vertically flowing mixing layer which is enclosed inside a pressure tank and fed by two banks of high-pressure gas bottles. The study considers both the unequal density (high-speed He and low-speed N_2) and equal density (high-speed N_2 and low-speed He-Ar) cases; the mixing of dissimilar gases is the source of the optical aberrations. Large-scale Reynolds numbers range between 3500 and 80000 over pressures from 2 to 6 bar. Light transmission characteristics are first studied qualitatively using a network of thin sheets of short-exposure ($\sim 1\mu$sec) white light which are aberrated by the mixing layer and then image directly onto photographic film. Light transmission characteristics are then studied quantitatively using a lateral effect detector to dynamically track a thin He-Ne laser beam as it wanders under the influence of the passing coherent structures.

The study finds that the spanwise coherent structures generate systematic deflections of the light beam in the streamwise direction; the greatest deflections occur near the trailing edges of the structures at a formation called the cusp, where the high-speed fluid and low-speed fluid are entrained into the vortex core. The streamwise coherent structures, which form later in the mixing layer's development than the spanwise structures, generate substantial beam deflections in the spanwise direction which are closely associated with the streamwise streaks in plan-view shadowgraphs. The rms fluctuations of the streamwise and spanwise deflection angles increase rapidly during mixing transition, peaking at 380 high-speed-side momentum thicknesses downstream from the splitter plate, then decrease far downstream to asymptotic values of 0.6 to 0.8 as scaled by the static pressure and the Gladstone-Dale constant shift across the mixing layer. The data suggest that a possible mechanism for the deflections is the interaction of the beam with the thin interfaces which bound relatively uniform bodies of fluid inside the structures.

TABLE OF CONTENTS

LIST OF SYMBOLS

Symbol

c	concentration
d	light beam diameter
dr	interface thickness in ray trace exercise
K_1	scaling constant for ray trace integral (see Eq 3.10)
K_2	scaling constant for ray trace integral (see Eq 3.11)
L	mixing layer edge cooridnate
n	refractive index
p	static pressure
R	gas constant
Re	Reynolds number
r	radius
SR	Strehl Ratio
s	distance along a ray
T	Temperature
t	time
W	wavefront surface
x	downstream distance
y	spanwise distance
z	light path direction of propagaton
β	Gladstone-Dale constant
δ	mixing layer thickness, turbulent region thickness
η	wavefront variation
θ	deflection angle
θ_1	momentum thickness on the high speed side
Λ	turbulence eddy size
λ	interface thickness
λ_0	most amplified initial wavelength

μ	kinematic viscosity
ν	dynamic viscosity
ξ	ray path length
ρ	density
σ	rms fluctuation
$\vec{\tau}$	unit vector along the ray
ϕ	wavefront angle

Subscript

SC	fully scaled for gas differences and pressure
s	standard conditions
x	streamwise direction
y	spanwise direction
δ	based on mixing layer thickness
θ	based on deflection angle
1	high-speed side
2	low-speed side
$2D$	two-dimensional

Superscript

$*$	pressure-scaled

TRANSMISSION OF THIN LIGHT BEAMS THROUGH TURBULENT MIXING LAYERS

1. INTRODUCTION

1.1 Objective and Philosophy

Aero-optics is the study of light transmission through aerodynamic flows, wherein "density inhomogeneities in the flow-field can perturb...the ability to propagate [light] beams through the flow-field (Sutton, 1985)." The field has its roots in atmospheric light transmission, which is the study of how the atmosphere distorts astronomical observations of celestial objects. Aero-optics has applications in the transmission of both laser beams and images through aerodynamic flows.

The general effect of inhomogeneous flows, such as those over viewing ports or nose-cones, is to aberrate the light in such a way as to degrade the quality of the laser beam or the image (Gilbert and Otten, 1982). The predominant effort in aero-optical theory has been to attempt to deal with this local problem via statistical treatment of the nature of the fluid flow. This approach is based on the assumption that a turbulent flow is isotropic and homogeneous, which in turn influences the manner in which data are collected and analyzed.

With the relatively recent discovery of large-scale coherent structures in turbulent flow (Kline et al., 1967; Brown and Roshko, 1974), the assumptions of isotropy and homogeneity are no longer entirely valid, particularly when applied to turbulent mixing layers, and the classical assumption that the dynamic flow variables are stochastic does not provide a complete picture of the flow (Dimotakis and Brown, 1976).

The question of relative scale sizes of the light beam, the path length through the turbulent region, and the size of the turbulence is important, because it facilitates the organization of the research into groups having common characteristics and

it determines scaling relationships in theoretical analysis. In this sense, the relative scales for a mixing layer can be thought of in much the same way as is considered for light transmission through a boundary layer by Liepmann (1952). Scale sizes are indicated by beam diameter (d), turbulent region thickness (δ), and turbulence eddy size (Λ). Traditionally, aero-optics has been characterized by assumptions and analysis in which the following relationships hold true.

$$\Lambda << \delta << d \tag{1.1}$$

Investigations have been concerned with transmitting large beams through shear layers or boundary layers. When applied to transmission through the atmosphere, the relationships become as follows.

$$d << \Lambda << \delta \tag{1.2}$$

In order to achieve the spatial resolution required for understanding how the flow structure affects beam transmission, this study uses the following relationship.

$$d << \Lambda \sim \delta \tag{1.3}$$

In the mixing layer, because of the presence of large-scale structures, the turbulence scale size Λ is on the order of the transmission path length δ. It is interesting to note that, from a scaling point-of-view, the problem attacked in this study is closer to atmospheric optics, i.e., Equation (1.2), than to classical aero-optics, i.e., Equation (1.1).

This research seeks to capitalize on the knowledge of the existence of coherent structure by connecting the behavior of a thin beam to flow structure. The result of the research, then, is to generate an alternative view of aero-optics as it applies to turbulent mixing layers, in a way which takes into account recent advances in the understanding of these flows. The research does this by studying how an incompressible turbulent mixing layer composed of two dissimilar gases produces optical distortions, particularly deflections, of thin light beams.

The study is done in two complementary parts in order to achieve both spatial and temporal resolution. The first part, consisting of short duration spark photography of a network of thin collimated sheets of white light, provides an instantaneous yet global view of the optics of a turbulent mixing layer. Spatial resolution is achieved by keeping the beams and sheets thin; classic shadowgraphy provides the same information, but the broad collimated light beams obscure the spatial details of the effects of the flow-field.

The second part of the experiment uses a high-speed lateral effect detector to dynamically measure the deflection of a thin laser beam in response to the passage of large-scale structures. The tracking experiment does not provide the overall perspective of the spark pictures; instead it provides a time history of a single thin beam at a particular fixed location in the mixing layer. This approach is different from most previous aero-optical studies; the previous work uses long time averages and broad beams, which do not provide the resolution necessary for understanding how the flow-field structure affects light transmission.

1.2 Overview

This work begins with a brief background on aero-optics and on current turbulent mixing layer knowledge, mostly based on experimental investigations since Brown and Roshko's 1974 article (Chapter 2). The background is followed by an examination of refractive index effects in flows composed of two dissimilar gases, in order to gain an insight into the behavior of thin light beams (Chapter 3). The groundwork for the experimental results is laid by a description of the experimental apparatus and procedures used (Chapter 4). The results of the high-speed thin sheet photography experiments and the position-tracking experiments for He/N_2 turbulent mixing layers (Chapters 5 and 6) and position-tracking experiments for a uniform density turbulent mixing layer (Chapter 7) are then presented. Finally, there is a discussion of the results obtained in which the various experiments are put into context with each other (Chapter 8) and a summary of the work (Chapter 9).

2. BACKGROUND

As previously mentioned, classical aero-optics has been based on several universally applied assumptions about fluid flow in order to arrive at some means of predicting the optical effects of various flows. The basis of aero-optics has been developed from the study of atmospheric light transmission, which assumes homogeneous turbulence. The statistics of homogeneous, isotropic turbulence are arrived at using time-averaged signals, in which all knowledge of the instantaneous flow has been lost. With regard to mixing layers, for example, these assumptions ignore the presence of large-scale coherent structures, and thus do not fully address this currently recognized feature of turbulent mixing layers. This chapter shall briefly summarize the basic ideas of classical aero-optics and then discuss more recent work which emphasizes the contributions of coherent structures to turbulence-induced optical aberrations. It also briefly reviews some aspects of turbulent mixing layers, namely their general features and the processes at work in them.

2.1 Aero-optics

Much of the origins of the field of aero-optics stem from atmospheric optics, which is concerned with atmospheric light or radio wave propagation (Chernov, 1960; Tatarskii, 1971). Because of the long propagation distances in the presence of atmospheric turbulence, the theory assumes random, homogenous refractive index fluctuations and uses the statistically based ideas of isotropic turbulence as a starting point for analysis. As such, a homogeneous random field is defined as one which has a constant mean and in which the correlation function between two points is unaffected by the simultaneous translation. Therefore, the function depends only on the points' relative positions, not on their positions in a fixed reference frame (Tatarskii, 1971). Isotropic fields are more restrictive in that the correlation function is direction independent, as well, i.e., it has no preferred direction or orientation. In other words, two light beams can travel through any part of a turbulent mixing layer, in any direction, and be affected in the same way as long as their separation is unchanged. These definitions are generally applied to time-averaged quantities as

being descriptive of the flow-field. As we shall see, at any instant in time, the turbulent mixing layer, because of the presence of large-scale, systematic, and relatively predictable nonuniformities, is neither truly homogeneous nor isotropic.

Aero-optics is different from atmospheric optics in that it includes the study of laser and image transmission through aerodynamic flows. The difference between these newer applications and atmospheric optics is in the relative magnitudes of the refractive index fluctuation scale size and the aperture size. Atmospheric optics typically involves fluctuation scales much larger than the aperture and path lengths much larger than the fluctuation scales. The aero-optical situation, on the other hand, involves fluctuation scales much smaller than the aperture (Sutton, 1985). In the aero-optical case, this assumption is important because it determines scaling relationships when combined with the use of time-averaged, isotropic statistics (Sutton, 1985).

The installation of optical apparatus on aircraft such as NASA's Kuiper Airborne Observatory has resulted in degraded optical performance due to interactions between a cavity in which the apparatus is installed and the outside airflow (Sutton, 1985; Elliot et al., 1989). The thick, turbulent shear layer over the aperture causes stellar images to be distorted in short (1 ms) exposures (Sutton, 1985). Because the distortions are nearly identical at all wavelengths, they are believed to be caused by refractive effects rather than diffractive effects, which indicates the presence of large-scale inhomogeneities in the flow (Sutton, 1985). However, with few exceptions, there has been little research on how these large-scale flow structures can affect light transmission.

Truman et al. (1990) discuss the use of geometrical optics to conduct a numerical study of the effects of organized turbulence structure on optical beam transmission through turbulent shear flow. The study shows that thin shear layers cause refractive index variations which generate phase distortions in the beam, which can significantly reduce the beam's intensity. Using a direct numerical simulation as a data base and treating the refractive index as a passive scalar, the study has

also found that the most intense scalar fluctuations are closely correlated with the presence of hairpin eddies and that the beam quality is dependent on the angle of transmission.

Tsai and Christiansen (1990) discuss the direct solution for two-dimensional Euler equations, with no sub-grid turbulence model, to study shear layer development and optical transmission characteristics. To quantify shear layer optical characteristics, the study calculates the phase error (ϕ) and Strehl ratio (SR) of an initially uniform large diameter light beam which is aberrated by the shear layer. An unaberrated beam possesses zero phase error across its aperture; large phase errors imply poor optical characteristics. Strehl ratio is the ratio of a beam's centerline intensity under aberrative conditions to the centerline intensity under ideal conditions. Therefore, $SR = 1$ implies perfect optical transmission characteristics. The study finds that the increase in ϕ is closely correlated with shear layer growth, and leads to a reduction in time-averaged SR with downstream distance. The computed mixing layer consists of large-scale vortical structures connected by thin braids of vorticity. Instantaneous SR plots of large diameter beams show that these large-scale structures are associated with local maximums in the optical degradations while the braids correspond to local minimums (Tsai and Christiansen, 1990). These variations in SR increase with structure size. Beam degradation is explained by saying that for large beams the degradations are due more to "wide-angle scattering" by turbulence structures which are much smaller than the beam diameter. For small beams the degradations are more due to wavefront tilt, although the thin beams used in the study are still broad (1.28 and 2.56 cm in diameter versus structures approximately 2.4 cm in diameter) by the standards of the present study. Thus, there is still a considerable amount of spatial averaging being done in the study. Also, because the computations are two-dimensional, the effects of three-dimensionality on light transmission and the spanwise variations inherent in turbulent shear flows are not addressed.

A second aspect of the work by Tsai and Christiansen involves using periodic

forcing to improve shear layer optical quality. The numerical experiments show that free shear layer growth is retarded in a limited region of flow if the flow is forced since vortex pairing, a major cause of shear layer growth, is suppressed. Control of shear layer growth was shown experimentally by Oster and Wygnanski (1982). Comparison of time-averaged SR ($\overline{\mathrm{SR}}$) in unforced and forced shear layers shows an increase in $\overline{\mathrm{SR}}$ in the no-growth region (Tsai and Christiansen, 1990).

Chew and Christiansen (1990, 1991), in an experimental study preceeding and similar to Tsai and Christiansen's numerical investigations, study the transmission of a 6.5 cm diameter He-Ne laser beam through a He-Ar/air mixing layer, with and without forcing. The laser beam is focused onto a CCD camera for both short (100μs) and long (2s) exposures. In the short exposures, simultaneous side-view shadowgraphs show the positions of the coherent structures. Beam quality measurements result in $\overline{\mathrm{SR}}$ values of 0.66 for the linearly growing, unforced layer and 0.91 for the forced, arrested growth layer (Chew and Christiansen, 1990, 1991). The improvement is attributed to reduced mixing, although it is uncertain if the growth difference is actually responsible for the improved optical quality or if there is another mechanism. The short exposure images show a signature which has a double peak intensity profile that moves with the mixing layer structures; the double peak is due to the fact that focussing the laser is equivalent to obtaining a far-field diffraction pattern due to the flow structure. Plots of $\overline{\mathrm{SR}}$ versus downstream distance show that maximum SR occurs just downstream of the splitter plate. Within the mixing transition region, SR falls off rapidly while far downstream it levels off. The decrease in SR is attributed to an increase in small-scale turbulence combined with increased mixing layer layer thickness (Chew and Christiansen, 1991).

2.2 The Turbulent Mixing Layer

The literature on turbulent mixing layers and coherent structures has expanded dramatically since the mid-1970's when Brown and Roshko's paper was published (Brown and Roshko, 1974). Since then, research has shown that the turbulent mixing layer is characterized not by fine-scale, homogeneous, isotropic turbulence,

but instead by large organized structures of the order of the layer width. Because of these features, the flows cannot be described as random and purely stochastic (Cantwell, 1981; Hussain, 1983; Coles, 1985 give comprehensive review articles). The pre-1970's approach to investigating turbulent mixing layers, using laboratory-fixed spatial correlation functions, obscures the connection between the function and the actual flow which produces it. Any correlated portion of a signal due to the repeated passage of an organized structure can thus be masked by other components of the signal (Cantwell, 1981). Primary vortices, also called spanwise coherent structures, are the spanwise-oriented rollers visible in the Figure 2.1 side-view (top). Secondary vortices, also called streamwise coherent structures, are the streamwise-oriented streaks in the plan-view (bottom). The flow structures are especially important because they dominate entrainment and mixing of the freestream fluid.

The large, roller-like spanwise coherent structures span the entire width of the mixing layer region, surrounded on either side by irrotational free-stream fluid. They convect downstream at a velocity close to the mean velocity of the two streams. The unforced mixing layer grows linearly with downstream distance from the splitter plate, since the structures grow by pairing or amalgamation as they convect downstream (Brown and Roshko, 1974; Bernal, 1981; Winant and Browand, 1974).

As the structures convect, they continuously induct surrounding free-stream fluid into the turbulent region in the boundaries of the mixing layer (Dimotakis, 1986). Once a fluid element is inducted into the turbulent region, it is strained by turbulent action until its scales become small enough for viscous diffusion processes to begin mixing the fluid on a molecular level (Dimotakis, 1986). As shall be discussed in Chapter 3, an important requirement for light beam deflection is the presence of a refractive index gradient, which can only occur on an interface between two dissimilar fluids. Because of the induction–straining process, we have relatively large regions of unmixed fluid of each type, separated by relatively thin interfaces at which most of the light aberrations occur.

The spanwise structures exhibit an essentially generic form; they have identifiable regions, which we shall refer to as the braid, the core, and the trailing edge or cusp, as illustrated in Figure 2.1. To a stationary observer (or thin light beam) the three regions convect downstream in repetitive order. Any given flow variable, for example concentration or density, thus cycles with the passage of each structure. The flow variable's signal can thus be thought of as having a a canonical and periodic component due to the coherent structure as well as a random component (Hussain, 1983).

Except at very low Reynolds numbers, the motion in a turbulent mixing layer is three-dimensional. Superimposed on the primary spanwise structure is the secondary, streamwise structure which shows up as thin filaments on a plan-view shadowgraph of the turbulent mixing layer (Figure 2.1). In the initial stages of the mixing layer, the streamwise structures are fixed at their spanwise locations, however, in the later stages of the mixing layer, they become nonstationary. The streamwise vortices consist of fairly evenly spaced and persistent counter-rotating vortex pairs that fill the braid region between the primary structures and occasionally become obscured by extremely fine-scale structure (Roshko, 1990). Figure 2.2 shows photographs of a turbulent mixing layer in a plane which is parallel to the spanwise structures so that the flow is coming out of the photograph (Bernal, 1981). The picture, taken in the Breidenthal water mixing layer facility (Breidenthal, 1978), shows the mushroom-shaped vortex pairs, the axes of which extend in the streamwise direction and are responsible for a large degree of three-dimensionality. The structures have important implications for mixing (Breidenthal, 1978; Bernal, 1981; Roshko, 1990); note that the core is composed of a mix of high- and low-speed fluid while the braid is a thin interface separating high- and low-speed fluid. The three-dimensional structure which is evident in the two photographs indicates a large number of fluid interfaces any light beam must encounter as it passes through the mixing layer.

The large-scale structure in the mixing layer, as previously indicated, plays

a major role in how and in what proportions the two fluids are mixed locally. Concentration measurements in both gas and liquid mixing layers show that there is more high-speed fluid than low-speed fluid inside the mixing layer (Konrad, 1976; Koochesfahani and Dimotakis, 1986). The asymmetry occurs because the large-scale spanwise coherent structures entrain high- and low-speed fluid at different rates. By treating each coherent structure as a unit which pulls the surrounding fluid into the core, simple theoretical estimates can be made of the entrainment ratios which closely agree with the experimental measurements (Dimotakis, 1989).

The mixedness of the turbulent mixing layer, i.e., the extent to which the entrained fluids mix, depends on whether the mixing layer has undergone mixing transition. When the fluid is in a "pre-transition" state, concentration measurements register primarily one fluid or the other, implying that little mixing is actually taking place, and the interfaces between the fluids are extremely thin (Roshko, 1990). Flow visualization pictures of the flow's side- and plan-views imply that the flow is highly two-dimensional, although the streamwise structures have already begun to form. Depending on the specifics of the flow (e.g., the Reynolds number), the pre-transition flow occurs in the upstream region of the mixing layer, closer to the splitter plate where the two fluids first come together. These features have been observed in both gases (Konrad, 1976) and liquids (Dimotakis and Koochesfahani, 1986).

Downstream of mixing transition, in the "post-transition" region, the flow is much different in several ways. The most visible change is that, while the large-scale spanwise structures are still evident, there is an increase in the small scale structure in both the side- and plan-views (Cantwell, 1981), although the increasing pressure in the gas experiments also enhances the appearance of any small-scale structures present (Roshko, 1990). The flow is highly three-dimensional and the streamwise structures are extremely well-developed. As a result, the mixing transition defines the point where the mixedness of the two fluid streams increases greatly. At mixing transition, the mixed fluid fraction, i.e., the proportion of fluid which is neither

pure high-speed fluid nor pure low-speed fluid, increases about 25 percent in gas and 1000 percent in water (Roshko, 1990). On high-speed shadowgraphs, the mixing transition occurs abruptly as shown by an almost instantaneous increase in small-scale structure. However, when time-averaged concentration measurements are used to determine mixing transition, the transition region is finite in extent, because the streamwise location of mixing transition varies in time. Light transmission through pre-transition fluid can thus be expected to behave differently from light encountering post-transition fluid, even though both regimes are considered to be turbulent flow.

Because of the radical change in the flow at mixing transition, it is useful to know when transition occurs. Traditionally, a local, large-scale Reynolds number Re_δ based on the velocity difference across the mixing layer, the mixing layer thickness, and dynamic viscosity, has been used. For both gas and liquid flows transition occurs at $Re_\delta \doteq 10^4$; as characterized by a plot of mixed fluid fraction versus $log(Re_\delta)$, transition takes place quickly (Roshko, 1990; Dimotakis, 1986, 1989 and others). Alternatively, because momentum transition is dependent on initial conditions, it can be said that mixing transition is also dependent on initial conditions, and its location can be correlated with the initial momentum thickness θ_1 of the high-speed fluid, and occurs between x/θ_1 values of 150 to 500 (Roshko, 1990). The high-speed fluid momentum thickness is used because the high-speed stream is the source of most of the vorticity which controls the sign of the Kelvin-Helmholtz disturbances which become the spanwise coherent structures (Breidenthal, 1978). Because of this x/θ_1 is preferred in the present study, although the effects of changing Re_δ shall also be examined.

3. THEORY

In this study, the light which passes through the turbulent mixing layer shall be treated using geometrical optics. The light will be assumed to consist of initially parallel wavefronts, whose direction of travel is indicated by a series of parallel rays. The transmission of the rays is governed by whether or not the medium through which they travel contains refractive index gradients. The wavefronts represent a surface, the position of which relative to a reference axis x is represented by W (Figure 3.1) For light moving through an electromagnetically isotropic medium, such as a nonionized, nonmagnetic gas, the wavefronts are always perpendicular to the rays. In a homogeneous medium where no refractive index gradients exist, the wavefronts are spherical in the case of a point source or planar in the case of a plane wave and the rays will be straight lines. If the medium is optically inhomogeneous, the rays bend and the wavefronts will curve and become distorted (i.e., W will vary in a nonspherical or nonplanar way).

3.1 Refractive Index Effects in a Two Species Mixture

The optical inhomogeneities and refractive index gradients are caused by combinations of species, pressure or temperature variations. In the present study, we have an incompressible mixing layer, to virtually eliminate pressure and temperature variations; thus the inhomogeneities are restricted to variations in species concentration across the mixing layer (e.g., He versus N_2, which have different refractive indices). Upon traversing the mixing layer, they are once again in a homogeneous medium, usually refracted by some angle θ relative to their undeviated path. For small θ (Figure 3.1), the wave front slope dW/dy is given by the following relation.

$$dW/dy = tan\theta \doteq \theta \tag{3.1}$$

Using geometrical optics, θ can be related via an integral relation to the refractive index field through which the ray passed. The first step in the development of the necessary relations is to understand how refractive index varies in a two species medium.

The index of refraction n is defined by the following relation.

$$n = \frac{c_o}{c} = 1 + \beta \left(\frac{\rho}{\rho_s} \right) \tag{3.2}$$

For a two species mixture, the refractive index of each species is defined as follows.

$$n_1 = 1 + \beta_1 \left(\frac{\rho_1}{\rho_{s1}} \right) \tag{3.3}$$

$$n_2 = 1 + \beta_2 \left(\frac{\rho_2}{\rho_{s2}} \right) \tag{3.4}$$

Considering a situation such as a mixing layer, where the two species are allowed to mix, the concentration of species 2 will be such that $0 \leq c_2 \leq 1$. From Appendix A, the refractive index will vary according to the following relation.

$$n = 1 + \frac{p}{p_s} \frac{T_s}{T} [\beta_1 + c_2(\beta_2 - \beta_1)] \tag{3.5}$$

Note that because we have assumed incompressible flow, the variations in c_2 are the only source of variations in n.

From Appendix B and Figure 3.2, the ray equation is given by the following equation.

$$\frac{d\phi}{d\xi} = \frac{-1}{n} \frac{dn}{d\eta} \tag{3.6}$$

From Equation (3.5), we can write $dn/d\eta$ as shown in Equation (3.7).

$$\frac{dn}{d\eta} = \frac{p}{p_s} \frac{T_s}{T} (\beta_2 - \beta_1) \frac{\partial c_2}{\partial \eta} \tag{3.7}$$

where in this particular case, $d\eta$ is the wavefront variation, not number density. For small deflections, transforming the equations to a mixing layer based coordinate system, and integrating across the mixing layer, we arrive at the following relationship (see Appendix C and Figure 3.1).

$$\frac{dW}{dx} = \theta_x \tag{3.8}$$

In Equation (3.8) θ_x, the deflection angle in the streamwise direction and indicated by the following Equation (3.9), is now a function of physical variables related directly to the flow.

$$\theta_x = \frac{p}{p_s}\frac{T_s}{T}(\beta_2 - \beta_1)\int_{L_1(x,y,t)}^{L_2(x,y,t)} \frac{\partial c_2/\partial x}{1 + \frac{p}{p_s}\frac{T_s}{T}(\beta_1 + c_2(\beta_2 - \beta_1))}dz \tag{3.9}$$

The equation for θ_y is the same except that it depends on the transverse gradient $\partial c_2/\partial y$.

This result can be simplified by using the following definitions.

$$K_1 \equiv \frac{p}{p_s}\frac{T_s}{T}(\beta_2 - \beta_1) \tag{3.10}$$

$$K_2 \equiv 1 + \frac{p}{p_s}\frac{T_s}{T}\beta_1 \tag{3.11}$$

From Equations (3.10) and (3.11), we can simplify Equation (3.9) as shown below.

$$\frac{\partial W}{\partial x_i} \doteq \theta_i = K_1 \int_{L_1(x,y,t)}^{L_2(x,y,t)} \frac{\partial c_2/\partial x_i}{K_2 + K_1 c_2}dz \tag{3.12}$$

In Equation (3.12), i=1 or 2 and x_1 corresponds to x and x_2 corresponds to y. Since the wavefronts can curve in two orthogonal directions, we have the gradient of W shown in the following equations.

$$\nabla_{2D} W = \frac{\partial W}{\partial x}\hat{\imath} + \frac{\partial W}{\partial y}\hat{\jmath} \tag{3.13}$$

From Equations (3.12) and (3.13), we have the following expression relating wavefront slope to the concentration.

$$\nabla_{2D} W = K_1 \int_{L_1(x,y,t)}^{L_2(x,y,t)} \frac{\nabla c_2}{K_2 + K_1 c_2}dz \tag{3.14}$$

Since K_1 and K_2 are independent of the flow-field details, Equation (3.14) can be rewritten in the following form.

$$\frac{K_2}{K_1}\nabla W = \int_{L_1}^{L_2} \frac{\nabla c_2}{1 + \frac{K_1}{K_2}c_2}dz \tag{3.15}$$

We now have an expression for the wavefront variation, i.e., deflection angle, through the mixing layer. By considering Equation (3.15) in light of the mixing layer structure (Chapter 2) we can make some scaling arguments which will give us some physical insights.

To simplify Equation (3.15) further, we note $K_1 << 1$, $K_2 \doteq 1$, and $0 \leq c_2 \leq 1$ with the following results.

$$\frac{K_1}{K_2} c_2 << 1 \tag{3.16}$$

$$\nabla_{2D} W \doteq K_1 \int_{L_1}^{L_2} \nabla_{2D} c_2 dz \tag{3.17}$$

Considering the two-dimensional case, then, and recalling that $\nabla W = \vec{\theta}$ where $\vec{\theta}$ can be thought of as the ordered pair (θ_x, θ_y), we have the following expression for θ_x, where both sides of Equation (3.17) have been divided by K_1.

$$\frac{1}{K_1} \theta_x \doteq \int_{L_1}^{L_2} \frac{\partial c_2}{\partial x} dz \tag{3.18}$$

Equation (3.18) shows the three ingredients necessary for causing the light beam to deflect as it passes through the turbulent mixing layer. The first requirement is a nonzero refractive index difference, which, because we are mixing two dissimilar fluids, is really a requirement for a nonzero concentration difference. In the mixing layer, this is only achieved at the interfaces between the two fluids. Thus, the second requirement is an interface thickness, neglecting a Snell's Law type of transmission through a sharp interface like that between air and glass. The maximum achievable refractive index gradient is determined by the two gases used in the experiment, which sets $\Delta\beta$, and the pressure at which the experiment is run. Therefore, all else being equal, θ is proportional to pressure and $\Delta\beta$, hence the presence of K_1 as the denominator in the left-hand side of (3.18). The interface over which refractive index changes (i.e., $K_1 \nabla_{2D} c_2$) occur must have gradients in a direction orthogonal to the beam's transmission path. Large interface thicknesses between dissimilar fluids imply small gradients, and vice versa for small interface thicknesses. The effect of interface thickness is countered by the final ingredient,

which is the integral nature of the light transmission problem, represented by the $L_2 - L_1$ transmission path length. Long transmission distances through small gradients can still result in large deflections.

In regions between interfaces, where the medium is pure high-speed fluid, pure low-speed fluid, or a uniform mix of the two fluids, the gradients are zero and the light rays travel in a straight line as determined by the interfaces previously encountered. Light transmission through low Schmidt number fluids like gases is probably characterized by intermittent encounters with thin interfaces, interspersed with travel through electromagnetically homogeneous fluid. Furthermore, because of the generic structure of the coherent structures, the successive interfaces encountered by the light are highly dependent on the light's position within the structure.

A possible means of scaling the bending angle in light of the above is provided by considering the quantity θ/K_1 and examining how its rms fluctuations change with x/θ_1 and Re_δ, as shown in the following equations.

$$\sigma_\theta = f(x/\theta_1) \tag{3.19}$$

$$\sigma_\theta = f(Re_\delta) \tag{3.20}$$

Fluctuations in both the streamwise (θ_x) and spanwise (θ_y) directions will be separately addressed. Because of the importance of the mixing transition to the flow's development, most likely two different relationships will exist, one for pre-transition flow and the other for post-transition flow.

3.2 A Simple Ray Trace Exercise

To generate some insight into how a turbulent mixing layer aberrates thin light beams, a ray trace exercise is performed. Rays are computed and transmitted through an inhomogeneous refractive index field which is a rough approximation of a coherent structure at a pressure of 2 bar (Figure 3.3). The model spanwise coherent structure is meant to simulate a post mixing transition vortex which has three types of fluid in it: pure high-speed, pure low-speed, and in the core 57

percent high-speed fluid as measured in concentration experiments (Konrad, 1977; Koochesfahani and Dimotakis, 1986, 1989). The model is two-dimensional, so it cannot be used to study the effects of streamwise coherent structures. All length scales in the computation are scaled to the core radius and the scaled interface thickness is 0.1.

For each ray, the deflection angle θ is computed. The computation of the deflection angle is done by numerically integrating

$$\frac{d}{ds}(n\vec{\tau}) = \nabla n \tag{3.21}$$

where s is the distance along the ray, $\vec{\tau}$ is a unit vector tangent to the ray, and n is the index of refraction. The numerical procedure, outlined in Klein (1970), is a two-step integration along the ray path, using the $\vec{\tau}$ at a known position to step to a new position, at which point the refractive index gradients are computed and used to calculate a new $\vec{\tau}$. The technique is similar to that used by Hesselink to investigate shock wave propagation through an inhomogeneous mediums (Hesselink and Sturtevant, 1988). Each "light beam," is composed of nine separate and tightly grouped rays which propagate through the structure from a selected point. The angles to which the rays are deflected are averaged to obtain the beam's deflection angle.

The results of three computations are shown in Figure 3.4, for which θ is computed for 32 separate positions in the structure. The three curves, which show the effects of varying interface thickness and structure size, all have a large upstream deflection associated with the trailing edge region of the structure. This would seem to indicate that much of the aberrative qualities of a two-dimensional turbulent mixing layer are associated with the relatively small region about the structure trailing edge. The downstream half of the core, i.e., for position/$r > 0$ (r is the radius of the structure; see Figure 3.3), is relatively aberration free with the exception of a smaller amplitude peak deflection right at the leading edge which lends some credibility to the general features of this simple topological model. We

would expect some deflection at the leading edge because the core is dominated by high speed fluid and thus the interface between the high-speed fluid outside the core and the fluid inside the core contains a weaker refractive index gradient. The strong deflection at the trailing edge occurs because the trailing edge is where the high- and low-speed fluids are entrained into the core and consequently contains the strongest gradients. Because the predominate portion of the structure is uniform fluid, the only source of beam deflections is at the interfaces.

The ray trace exercise allows the effect of changing interface thickness (dr) and structure size (r) to be examined (Figure 3.4). From Equation (3.18), we would expect that doubling the structure size and interface thickness while holding the refractive index shift constant would result in no change in θ since the transmission path length is doubled while the gradient is halved. This expectation is proved correct in Figure 3.4; comparing the $r = 1$, $dr = 0.1$ and the $r = 2$, $dr = 0.2$ plots, we see that they fall on top of one another. Similarly, if we double the structure size to $r = 2$ while holding the refractive index shift and the interface thickness constant, we get a plot which displays θ values roughly twice those of the $r = 1$, $dr = 0.1$ plot. The three plots point to the importance of the scaling relationships between the growth of the interface thickness and the growth of the spanwise coherent structures as the turbulent mixing layer develops.

4. APPARATUS AND PROCEDURE

4.1 Facility Description and Test Conditions

The heart of the apparatus is the Brown-Roshko Gas Mixing Layer Facility (Figure 4.1). Briefly the facility is a vertically flowing, two stream test section, which is fed by bottled gas and enclosed inside an 8 bar-rated pressure tank. The tank has two glass windows for use in optical experiments. It also has electrical feed-throughs for instrumentation. Two optical tables of equal height straddle the facility in the horizontal plane, making it possible to align the optics without having to change their height, which makes the set-up easier to accomplish. The tables have steel tops for use with magnetic bases and are joined by two aluminum I-beams for rigidity.

Flow diagnostic hardware includes two Datametrics Model 590D Barocel pressure transducers to measure the dynamic pressure of the two streams and the wall pressure gradient, and an Everex System 1800 microcomputer (IBM PC-AT clone) equipped with an RC Electronics, Inc. IS-16E Computerscope data acquisition system (1 MHz total sample rate) to record the Barocel output. The computerscope is also used for the second set of experiments involving the use of a lateral effect detector to dynamically track a laser beam (see Section 4.3).

Because the mixing transition is important to flow properties and hence to light transmission through mixing layers, the experimental conditions are chosen to ensure that data are taken above and below transition (see Tables 1, 2, and 3). In tests with He and N_2, the dynamic pressure of the two streams is matched, so that $\rho_1 u_1^2 = \rho_2 u_2^2$. In tests with He-Ar and N_2, the densities are equal, but the velocity ratio used is the same as for the He/N_2 experiments ($u_2/u_1 = 0.38$). Table 4 lists the Gladstone-Dale constants of the gases used in the experiments, from which the refractive indices may be calculated using Equation (3.2). These conditions are essentially those used earlier in the facility (Brown and Roshko, 1974; Konrad, 1976; Bernal, 1981; Wang, 1984).

4.2 High Speed Thin Sheet Photography

Because short duration photographs are needed to discern how the overall flow structure affects a light beam passing through the mixing layer, a spark lamp of only a few microseconds duration is used. At the relatively low velocities ($< 10m/s$) , this means that the structures only convect approximately 10^{-5} m during the exposure, thus effectively freezing the motion with the field-of-view.

As a first means of characterizing light transmission through turbulent mixing layers, it is desirable to retain some sense of the continuum of effects across the mixing layer without being overwhelmed by the information present in a standard plan-view shadowgraph. To this end, a Cartesian-type grid of light sheets is used.

The optics (Figure 4.2) consists of the spark source (S_1), a light collection lens (L_1) a small flat mirror (FM_1), a 190.5 mm diameter, 1270 mm focal length spherical mirror (SM_1), a large flat mirror (FM_2), the grid (G), and two 45 degree flat mirrors (FM_3 and FM_4). All mirrors used in the experiments are first surface mirrors. Two "cameras," (C_1 and C_2), are used. C_1 is a 101.6 mm×127 mm (4×5 inch) sheet film holder mounted inside the tank in a bracket which places the film approximately 6mm away from the test section wall, thus providing for clear shadowgraph (sideview) mixing layer pictures. C_2 is also a 101.6 mm×127 mm (4×5 inch) sheet film holder, onto which the light beams or sheets are imaged. Immediately in front of C_2 is an aluminum frame with a Cartesian grid of thin platinum wires for use as a reference.

The light sheets are created by illuminating a grid (Figures 4.2 and 5.1) which is opaque except for thin, evenly-spaced lines with collimated light directed perpendicular to the shear layer. The individual lines are spaced 5.08 mm apart and are 1.016 mm wide. The lines are canted approximately 8 degrees from the streamwise and spanwise flow axis' so it is possible for orthogonal light sheets to traverse both the span-wise structure and stream-wise structure. A system of mirrors directs the light sheets through the mixing layer, at which point they are distorted. The now

aberrated sheets then directly expose the negative which is placed at either 559 mm or 1118 mm from the test section. The two distances are used as a means of cancelling the direct effects of pressure on the deflection of the sheets between the 4 and 2 bar tests. A three to four stop push during developing is necessary to fully expose the grid picture because of the small amount of light in the sheets. The experiments are carried out in absolute darkness to avoid contaminating the film with unwanted stray light and one exposure is made with each run.

Along with each light sheet photograph, a simultaneous side-view shadowgraph is made from the same spark, thus providing information on the disposition of the spanwise coherent structures.

As can be seen in a light sheet picture such as Figure 5.2, the area around the grid image has been left open, to show a partial plan-view of the mixing layer. This aids the interpretation and the process of lining up the side-view shadowgraphs of the flow with the light sheet images. When the photographs are developed and prints made of each view, the two images are lined up next to one-another in their proper orientation. The exposures are then analyzed with two broad issues in mind: (1) where the initial light beams are relative to the overall streamwise and spanwise flow structure and (2) how the light beams change relative to their initial condition. This allows the behavior of the light sheets to be accounted for in terms of what part of a primary vortex they encounter. Streamwise vortex effects can be considered also by comparing the partial plan-view images showing the streamwise vortices to the sheet deflections.

4.3 Position Tracking Experiments

In order to gain both a quantitative understanding of how a light beam is affected by the coherent structure as well as study the beam's dynamic behavior, experiments are conducted in which a He-Ne laser beam is tracked in real time as it deflects under the influence of the passing large-scale structures.

The general set-up, diagrammed in Figure 4.3, consists of many of the same

components as the Spark Picture Experiments. The spark picture system is used to take a single side view shadowgraph of the turbulent mixing layer on C_1. A Spectraphysics Model 132 He-Ne laser is focused by two lenses (L_{l1} and L_{l2}) of 125 mm and 250 mm focal lengths, respectively, and reduced in intensity by a neutral density filter (N). The beam is directed by a succession of mirrors (FM_{l1}, FM_{l2}, and FM_2) to an adjustable beam director (BD). The BD shifts the laser beam in the streamwise direction to put it at the desired location. A flat mirror (FM_3) directs it laterally through the mixing layer, and another flat mirror (FM_4) redirects it back out of the tank. The detector (D) tracks the beam as it wanders. Spanwise placement of the laser beam in the mixing layer is done by shifting mirror FM_{l2}.

The deflected beam is tracked using an SC-10D lateral effect detector made by UDT Sensors, Inc. The sensor, which has an active area of 10.16 mm × 10.16 mm, is a silicon-based dual-axis position-sensing photodiode (Figure 4.4). It is an analog device, as opposed to a CCD array, and is sensitive to the position of the laser; the energy centroid of the beam is measured relative to two orthogonal axes which are centered on the detector (the sensor generates a current proportional to the position of the spot). Thus, if the beam is centered, the output of the photodiode is zero, as is also true if the beam is evenly split, for example, along the x-axis. For this reason, it is necessary to make the beam as small as possible to reduce the uncertainty due to beam dispersion. In the test section it is approximately 1 mm wide, and by the time it reaches the detector it is approximately 2 mm wide. Although deflection magnitudes are on the order of 0.5 mm, calibration of the detector using a micrometer equipped optical translation stage show a continuous sensitivity of 0.33 mm/V and a resolution of 0.01 mm, or about 2 percent based on the maximum deflections at 2 bar pressure. For higher pressure test runs, the deflections are greater so the resolution improves.

The outputs from the detector are amplified and converted by two UDT Instruments, Inc. Model 301DIV 30kHz amplifiers, one per axis, into -10 to +10 V signals. The voltage output from the amplifiers is sampled and recorded by the

data acquisition system.

In addition to recording the beam dynamics, it is important to correlate it with information on the mixing layer, which is monitored using a single hot-wire anemometer positioned next to the laser beam axis. The hot-wire voltage, which fluctuates in response to the passing coherent structures, is also digitized and recorded by the Computerscope system.

The spark lamp generates a synchronization signal, which is recorded by the data acquisition system so that the spark picture from C_1 can be placed at its proper position in the hot-wire data.

Because of limitations in the data acquisition system and differences in the acquisition parameters for free-stream velocities and beam deflections (one requires slow sample rates while the other requires high sample rates), the experiment is run in three stages. The first stage involves several runs in which the flow velocities are adjusted using needle valves located at the top of the facility. Only dynamic pressure data are collected in this stage; each data set consists of 16384 points taken at 305μs between samples for a run of 5s beginning from when the flow is turned-on. The last 6380 points and the first 100 points (as a zero) are averaged, then subtracted. The dynamic pressure is used with Bernoulli's equation to calculate the velocity of each stream. Generally 6 to 10 preliminary runs are required before the velocities are set; they are periodically checked and adjusted as needed as the supply bottle pressures drop .

Next, the hot-wire is positioned so as to provide a clean, regular marker signal of the flow and 8192 points are taken at approximately 50 to 154μs between samples for 0.4 to 1.2s of data. Data acquisition actually begins 3s after the flow is turned on, to allow the flow to achieve a steady-state condition.

Finally, the laser is centered on the detector, and a series of runs, with the same sample rates as the previous hot-wire data, are made using the detector and the hot-wire. These data are also delayed by 3s and result in x and y deflection

and hot-wire data traces. Because the detector is sensitive to ambient light levels, to reduce noise in the detector data the runs are made with the room lights off. When deflection and hot-wire data are collected simultaneously, 8192 data points are recorded per run. When only deflection data is collected, 16384 data points are recorded. Generally, three data runs are made, with no-flow reference runs in between. The mean and rms voltages for each are calculated, then averaged together.

Data analysis is relatively straight-forward. After each run, the mean and rms fluctuations of the various measured quantities are calculated. From calibration data on the sensor, the data and reference voltages are converted into deflections in the x and y directions, then divided by the distance from the test section and the pressure at which the experiment is run in order to arrive at mean and rms fluctuations for the pressure-scaled deflection angles in the streamwise and spanwise directions.

5. HIGH SPEED THIN SHEET PHOTOGRAPHY

As discussed previously Section 2.1, classical aero-optical theory is based on the assumption that a mixing layer is statistically homogeneous and isotropic. However, the effect of the shear layer on the light sheet indicates substantial effects which are due to the coherent structures in the flow. These effects can be divided up into those caused by the spanwise structures, those caused by the streamwise structures, and those associated with mixing transition.

Prior to the examination of the photographic data, an orientation and explanation of terms is in order. Various features are illustrated in Figure 5.1, which also shows the undistorted grid before the gas is turned on. The grid pattern made by the sheets are slightly tilted; spanwise sheets are those extending *mainly* across the span and streamwise sheets are those extending *mainly* downstream. For the most part, we are concerned with the streamwise deflections of the spanwise sheets and the spanwise deflections of the streamwise sheets. These deflections have two components: primary, large-scale deflections due to the large-scale coherent structures and higher-order, small-scale deflections or fluctuations (see Section 2.2).

Each Figure 5.2 through 5.11 is a composite of two orthogonal views. The side-view spark shadowgraph of the mixing layer is on the right side of the figure, and provides an overall view of the flow. The figures are the photographic data obtained from experiments conducted in which He is always the high-speed gas and N_2 is always the low-speed gas. Table 1 summarizes the conditions of the experiments represented in the Figures 5.2 through 5.11. The left side of each figure is a photograph made by the light sheets impinging directly on the film (as opposed to using scattered light such as those obtained by the laser-induced fluorescence technique). These light sheet images, in the absence of refractive index gradients, appear as a network of straight, evenly-spaced lines. Therefore the distortions in the light sheets serve as an indicator of the aberrative effects of the mixing layer, which is the focus of the present work. The area around the edges of the network is a partial plan-view of the flow (i.e., a plan-view shadowgraph) showing some of the

primary and secondary structure. The photographs are shown full-scale)and the thin black lines are the wire grid next to the negative which is used as a coordinate system (see also Section 4.2).

5.1 Effects of Spanwise Coherent Structures

The spark photographs reveal that light sheet deflection is highly dependent on the part of a spanwise coherent structure through which the light passes. This data reveals that the coherent structures in a turbulent mixing layer have an asymmetric effect on the light sheets.

One of the most striking features evident in the photographs is that the greatest distortions are caused by an area in the vicinity of the spanwise structure's trailing edge (i.e., the upstream side–see also Figure 2.1), near a feature which shall be referred to as the *cusp* in the side-view shadowgraphs. This cusp is not to be confused with the cusp-like formation at the trailing edges of the spanwise coherent structures in the images of Koochesfahani and Dimotakis (1986). In Figure 5.2, for which the mixing layer is at the lowest Reynolds number tested, the cusps are at $x \doteq 48$ and 66 mm (see Table 1 for a summary of experimental conditions). In this experiment, bending of the light sheets is discernable only near these locations; the distortions of the light sheet manifest themselves as the small up- and downstream deflections of the spanwise oriented light sheets. In Figure 5.3 the Reynolds number is the same, but the light sheet distortions have been magnified by placing the negatives further away from the flow. The figure shows the up- and downstream deflections at $x \doteq 53$ and 71 mm. Figure 5.4, at $x \doteq 46$, 64, and 91 mm shows very clearly the cusp's effects on the lateral light sheets.

The results suggest that a cusp typically acts as a refracting device, particularly to converge the light passing just to either side of it. Light sheets just downstream of the cusp are deflected in an upstream direction while those just upstream are deflected in a downstream direction. Furthermore, these deflections are not symmetric about the cusp; the upstream deflection tends to be of higher magnitude.

For example, Figure 5.3, at $x \doteq 71$ mm, Figure 5.5, at $x \doteq 45$ and 66 mm, and Figure 5.6, at $x \doteq 41$ and 79 mm, all taken at different flow conditions, show this general trend.

Turning our attention to the core and braid regions of the spanwise coherent structure, the deflection magnitudes are much less than those at the cusp. At the lowest Reynolds number studied, i.e., Figures 5.2 and 5.3, the streamwise deflections due to the cores and braids are negligible (e.g., Figure 5.2, $x \doteq 56$ to 64 mm and 71 to 81 mm). At higher Reynolds numbers, for example at $x \doteq 69$ to 85 mm in Figure 5.4, the distortions of the core and braid are noticeably weaker.

An alternative way of isolating the relative distortions caused by the cusp is to examine the dark squares defined by the network of light sheets. Under nonaberrative conditions (i.e., without the mixing layer), the squares are 5.08 mm×5.08 mm (0.2 × 0.2 inches). The focussing of two parallel light sheets reduces the size of the squares. This is exactly what happens to squares which are formed by light sheets which straddle a cusp, for example at $x \doteq 64$ and 89 mm in Figure 5.4. In the vortex cores, between the cusps, the effect is opposite; there the squares get larger as the two lateral sheets which bound them are pulled apart in the streamwise direction ($x \doteq 76$ mm in Figure 5.5 and , $x \doteq 64$ and 81 mm in Figure 5.7). Part of the pulling apart is due to differences between the cusp, which distorts the upstream sheet in the *core* in an upstream direction, and the downstream side of the core (not the leading edge), which causes little or no bending in the downstream sheet. Because an increase in pressure results in greater refractive index differences between the gases, these distortions are magnified in the higher pressure runs.

At higher Reynolds numbers the presence of bright spots at various portions of the grid becomes apparent. These spots are produced by the light sheet being focussed in its plane instead of being deflected orthoganally. Generally, but not always, the spots occur near a cusp (e.g., Figure 5.3, $x \doteq 89$ mm or Figure 5.4, $x \doteq 76$ mm). Note that the light sheets in the immediate vicinity of a spot are dimmer than the spot itself. This is because the light entering the mixing layer is

conserved; since it is not absorbed by the gases, as a region of fluid focuses the light there must be a reduction in intensity elsewhere.

5.2 Effects of Streamwise Coherent Structures

In addition to the aberrations caused by the spanwise coherent structures, there are significant aberrations due to the streamwise coherent structures or secondary vortices. For regions far upstream, close to the splitter plate, the effects are small compared to the effects due to the primary vortices. These effects become more pronounced as one moves farther downstream from the splitter plate. In the case of Figures 5.2 and 5.3, the spanwise deflections of the streamwise-oriented light sheets are negligible for the entire length of the grid. This may be due to mixing transition occurring beyond the field of view; from Table 1 and Figure 5.2, for example, $Re_\delta \doteq 6600$ at the bottom of the network (i.e., $x \doteq 100$ mm). In Figure 5.4, taken at a higher Reynolds number, for $x < 43$ mm, we see almost no deflections. For $x > 51$ mm, the lateral deflections in the light sheets increase greatly. As the Reynolds number is increased, the discernable distortions move further upstream (Figures 5.4, 5.5, 5.6, 5.9).

As in the streamwise deflections of the spanwise-oriented light sheets by spanwise structures, the spanwise deflections of the streamwise-oriented light sheets are dependent on the specific regions in the flow through which the sheet travels, particularly at a lower Reynolds Number. In Figure 5.4, this becomes apparent if we follow sheet c (the light sheets are lettered from left to right in alphabetical order and extend diagonally downstream through the grid from the top of the photograph) through various regions of the flow-field and observe how it deflects. In the case of light sheet c, starting from the downstream edge of the grid and moving upstream, it immediately crosses the axis of a streamwise-oriented streak and deflects first to the left, then back to the right, and is straight between $x \doteq 66$ and 76 mm. Sheet a at $x \doteq 64$ and 92 mm exhibits similar deflections. In Figure 5.6, if we follow sheet b from the downstream end of the grid we can see alternating deflected and straight sections of light sheet as we follow the light sheet diagonally upstream.

The photographic results indicate that there are two places where these spanwise deflections occur. Spanwise deflections are observed where the sheets cross the streamwise streaks (Section 2.2) which are visible downstream of the grid where uniform illumination produces a standard plan-view shadowgraph. The deflections due to the streamwise structure can result in the focussing effect which produces the streamwise streaks on a plan-view shadowgraph. Because the sheets are oriented at an 8 deg angle to the streamwise direction, any given sheet crosses the streamwise streaks (e.g., Figure 5.4, sheet c at $x \doteq 94$ mm). In response to the refractive index gradients present in the streamwise structures, the part of the sheet on one side of the streak may be bent laterally to the other side (e.g., Figure 5.5, $x \doteq 64$ and 102 mm). The focussing of adjacent light sheets and the resulting crossing of formerly parallel beams of light generates a streamwise-oriented intense region of light which shows up on film as a streamwise–oriented streak on the shadowgraph. In some cases, i.e., Figure 5.7, $x \doteq 64$ mm, sheets a and b undergo enough bending so they actually cross prior to exposing the film. Because the light travels in straight lines upon leaving the mixing layer, any bend in any light sheet eventually leads to numerous ray crossings, especially when the film is placed far from the flow as in Figure 5.7.

The second place where spanwise deflections have been observed is in the region immediately downstream of the cusps; the deflections can be much larger in magnitude relative to deflections generated by other regions in the flow (e.g., Figure 5.5, $x \doteq 64$ to 69 mm; Figure 5.6, $x \doteq 58$ and 81 mm ; and Figure 5.8, $x \doteq 51$ and 76 mm). Immediately upstream of the cusps, particularly in Figure 5.8, where the light sheets are in a braid region, the spanwise deflections of the longitudinal light sheets are relatively mild. These results would seem to indicate that even at the trailing edges of the spanwise vortices there exist strong spanwise refractive index gradients in addition to the two-dimensional streamwise gradients.

5.3 Mixing Transition Effects

As mentioned in Section 2.2, the mixing transition is accompanied by greatly in-

creased three-dimensionality, greater growth of the streamwise coherent structures, and enhanced mixing, which result in a change from predominantly high-speed fluid in the core to more equal but decidedly asymmetric proportions. The process takes place quickly and, because the refractive index field is dependent on mixing, can have dramatic effects on the optical properties of the mixing layer.

The major effect of mixing transition is to divide the flow into two different optical regimes. Upstream of transition, where the flow is in a "pre-transition" state, the mixing layer exhibits the optical qualities discussed in Sections 5.1 and 5.2. In Figure 5.9, for example, it appears that transition occurs at $x \doteq 51$ mm. Upstream of that point, the cusps generate large optical distortions in both the spanwise- and streamwise-oriented light sheets. The distortions due to the streamwise structure are small, as are the distortions due to the core and the braid.

Downstream of the mixing transition, in the "post-transition" regime, the optical character has changed; distortions due to the streamwise coherent structures, in the form of lateral deflections in the streamwise-oriented light sheets, appear to represent the major source of optical aberrations. In Figure 5.9, these lateral deflections have increased from essentially zero for $x < 51$ mm to approximately 1.5 mm for $x > 1$ mm, as measured visually using a straight edge. In Figure 5.8, mixing transition appears to occur at $x \doteq 71$ mm, and for $x > 71$ mm, the deflections in the longitudinal sheets, e.g., sheet d, exceed the deflections in the lateral light sheets.

A second important characteristic of the post-transition regime is that the level of small-scale fluctuations (Figure 5.1) is much greater than in the pre-transition part of the flow. In the side-view shadowgraph pictures transition results in the appearance of smaller-scale structure (Figures 5.8, 5.10, and 5.11), although the higher test pressures are responsible for some of the changes. These higher-order fluctuations are localized; if one compares the fluctuation levels for light sheets near the cusps to those in the braid and core regions, the cusps seem to generate a higher level of fluctuations. In Figure 5.8, the cusp at $x \doteq 66$ mm generates much higher fluctuations than the core-braid region immediately downstream ($x \doteq 81$ to

89 mm). In Figure 5.10, the light sheets are so distorted, in part because the film is relatively far away from the test section, that it is difficult, if not impossible, to track a streamwise-oriented light sheet, while the identification of spanwise-oriented sheets is somewhat easier. Comparing $x \doteq 69$ mm to $x \doteq 76$ mm, we again see that the cusps generate stronger distortions.

A third result of the mixing transition and the increase in the level of small-scale structure is the increase in the number of spots visible in the photographs. This is particularly true of the highest Reynolds number condition of Figure 5.11, where the entire flow field seems to generate the intense white spots visible less frequently in Figure 5.4. The spots increase in number and intensity near the cusps, such as at $x \doteq 56$ and 79 mm in Figure 5.11. It is unclear, however, whether they are due to the increased pressure alone, or also to some changes in the flow strictly due to Reynolds number effects. Increasing Reynolds numbers tend to generate more small-scale fluid structure, which would be consistent with the larger number of spots.

With regard to how the flow structure focuses the light sheets, because of the strong smaller-scale component of the sheet deflections, focussing cannot be judged using only a single spanwise or streamwise sheet as a guide. A somewhat larger view, using adjacent light sheets to provide the needed clues, indicates that generally, as with the pre-transition cases, the cusps and streamwise vortices tend to focus adjacent sheets. In Figure 5.8, at $x \doteq 91$ mm, sheets b and c are pulled together, away from sheet a on their immediate left and sheet d on their immediate right. The plan-view shadowgraph directly downstream (not diagonally) from this point shows that this is occurring along a streamwise streak; the streak is also visible at the top of the network. In Figure 5.10, even though the distortions of individual light sheets have a very strong small-scale component, the pulling together of the spanwise sheets is visible at $x \doteq 56$ and 79 mm, next to the cusps. In Figure 5.11, at $x \doteq 76$ mm, the same thing can be observed, as well as two streamwise sheets b and c drawing closer together at $x \doteq 89$ mm.

These results show that the mixing transition generates higher-order, small-scale structure of a seemingly haphazard nature in the light sheet deflections. However, the general structure of pre-transition flows in terms of the optical effects of the spanwise and streamwise structures appears to carry through the mixing transition into the post-transition flow regime. Even in the post-transition regime, the cusps generally cause greater distortions than nearby braids and cores and continue to act as focussing elements of the flow. The streamwise-oriented secondary structures also focus light into what we see as the streamwise streaks in the plan-view shadowgraphs. Thus, even after mixing transition, the mixing layer continues to exhibit a significant degree of anisotropy and inhomogeneity as opposed to isotropy and homogeneity as is assumed in classical aero-optics.

6. POSITION TRACKING EXPERIMENTS FOR A He/N_2 TURBULENT MIXING LAYER

The use of the lateral effect detector (Section 4.3) to track the deflections of a laser beam in response to the flow in a He/N_2 turbulent mixing layer provides a dynamic means of understanding the origins of the mixing layer's optical properties. Although the spanwise coherent structures convect by the laser beam and produce deflections which are a continuous temporal record of the effects of the primary vortices, comparisons of data taken at various experimental conditions and spanwise positions allow conclusions to be made as to the effects of the streamwise coherent structures as well. Finally, mean and rms fluctuation values of the deflections provide insight as to the effects of mixing transition.

It should be noted that the refractive index shift across the mixing layer, which is ultimately determined by $\Delta\beta$ ($\equiv \beta_2 - \beta_1$) for this experiment, controls the polarity of the trace. Since the laser beam traverses the flow by passing from the He to the N_2, $\Delta\beta > 0$ ($\beta_{N_2} > \beta_{He}$), and the cusp-related maximum deflection is upstream (i.e. in the negative direction). If $\Delta\beta < 0$, then the deflection is downstream (i.e. in the positive direction) and the other deflections associated with the spanwise coherent structure are reversed in sign.

6.1 Effects of Spanwise Coherent Structures

In this study, we try to understand how instantaneous flow structure affects light transmission by studying beam deflection versus time and identifying different features of the data with convective structures which might be seen in typical side-view spark shadowgraphs. Initially, multiple sets of hot-wire data, each accompanied by a single side-view shadowgraph, were used to associate the instantaneous flow structure with portions of the hot-wire signal. However, since it is a point measurement, the hot-wire phase is extremely sensitive to its placement within the mixing layer, to the size of each successive spanwise coherent structure, and to its

spanwise position. Therefore, correlations between the signal at a point in space and time and a shadowgraph image of the flow are suitable only in a qualitative sense. Instead, a combination of the hot-wire signal, the photographs, the beam deflection signal, and the information obtained from the thin sheet photographs is used to study the effects of flow structure on light beam behavior. The hot-wire, positioned just inside the layer on the high-speed side, produces a characteristic signal, a sample of which is shown in Figure 6.1. Accompanying the signal is a simultaneous plot of beam deflection versus time. As can be seen in Figure 6.1, there exists a close correlation between the beam deflection and the hot-wire signal, in particular between the negative extremums in each trace. Although the trace's precise nature depends on its exact placement in the mixing layer, the general relationship between the E_{HW} trace and the passing coherent structures is shown in Figure 6.2.

Three features are generally present on the trace, and are labelled A through C in Figure 6.2. Feature A corresponds to the flow of high-speed He by the wire and thus occurs primarily between structures. Feature B generally occurs in the core where He and N_2 are mixing. Feature C is the most identifiable; this sharp negative voltage spike is associated with the passage of the cusp. Since the hot-wire is left in position and runs are next made with the laser beam traversing the mixing layer next to the hot-wire, the beam's behavior can be related directly to its relative position in or near a spanwise coherent structure or primary vortex.

Deflection angle versus time data are shown in Figures 6.3 through 6.7, which cover a range of Reynolds numbers. These figures show the pressure-scaled streamwise deflection angle (θ_x^*) and spanwise deflection angle (θ_y^*), which are computed by dividing the deflection angle (θ_x or θ_y) by the pressure ratio p/p_s where p_s is 1 bar to remove any direct pressure effects (Sections 3.1 and 4.3). In lower Reynolds number cases such as Figures 6.1, 6.3 and 6.4, the traces are free of higher-order signal components, and there is clearly a characteristic, recurring deflection signal.

From the data, including the high speed light sheet photographs of Chapter 5,

it is reasonable to conclude that the large-amplitude, negative-to-positive θ_x^* swings are caused by the cusps. These swings are large compared to the rest of the signal; the initially occurring negative extremums represent large upstream deflections of the laser beam. The upstream deflection is followed by a rapid swing in deflection to a positive value. Additional confirmation comes from recalling the results of the ray trace exercise in Section 3.2 and the light sheet photographs of Chapter 5; both indicate that the cusp is a primary source of high-amplitude upstream beam deflections.

The rapid positive swing is essentially representative of the cusp's focus effect (see Section 5.1). An increase in time on the trace is equivalent to a decrease in x in the reference frame of the test section. The negative peak followed by a positive peak can be interpreted as an upstream deflection on the downstream side of the cusp followed by a downstream deflection on the upstream side of the cusp (recall that since the beam is fixed, the cusp convects by it). Similar behavior has been observed in the thin sheet photographs of Chapter 5.

The laser beam is fixed at $x = 44.5$ mm from the splitter plate in Figures 6.3 and 6.4. As spanwise coherent structures convect by the beam, it repeatedly passes through a cusp, a braid, a core, and the next cusp in successive order (Section 2.2); the progression is labeled A to B, B to C, and C to D respectively in Figures 6.3 and 6.4. At the braid, the deflection angle is at the positive maximum and is beginning to decrease at successively increasing rate. At a certain point, the beam encounters the leading edge of the next spanwise coherent structure, which produces a momentary hesitation or shoulder (e.g., note C Figure 6.3, $t \doteq 0.17$s or Figure 6.4, $t \doteq 0.08$s) in the trend. Once inside the core, the beam continues on to its negative extremum; this is followed by a rapid reverse and swing to a positive deflection, during which time the cusp convects through the beam.

Figure 6.3 also shows that, even at relatively low Reynolds numbers, the mixing layer's structure occasionally breaks down, so the generic deflection signature may briefly disappear. After several periods, the instabilities reestablish themselves and

the regular signal reappears. Alternative mechanisms are either that the mixing transition momentarily moves upstream of the beam and adds a small-scale, three-dimensional component to the deflection signal or that vortex pairing occurs as the structures convect by the beam. Without a continuous series of pictures, however, it is hard to determine the true source of such a deterioration in the signal.

In addition to the close correlation between the spanwise coherent structures and the streamwise deflections (θ_x), there is also a correlation between the spanwise coherent structures and the spanwise deflections (θ_y). In Figure 6.3, the spanwise fluctuations are extremely small, except for small peaks which coincide with the θ_x^* negative peaks. Hence, the laser beam undergoes regular excursions in the spanwise direction as the cusps convect by it. In Figure 6.4, taken at a higher Reynolds number, the increase in the θ_y^* magnitude is noticeable, yet still closely associated with the cusps.

However, turbulent mixing layers are highly three-dimensional, and exhibit great variation across their spans; these variations are extremely important for the temporal variations in θ_y^* (cf., Section 2.2). Figure 6.9 is a collection of low Reynolds number θ_y^* traces at six spanwise positions 2 mm apart. The characteristic θ_x^* waveform is visible in all six traces. The θ_y^* trace shows some variations across the span and a consistent signature cannot be defined. A common feature in the data is the occurrence of a positive or negative peak in deflection angle as each cusp convects by the laser beam (e.g., $t \doteq 0.18$s in Figure 6.9a or $t \doteq 0.17$s in Figure 6.9b). This agrees with the spark picture data of Section 5.2. The variation in the mean and rms fluctuations of θ_y^* across the span are fairly large; explanation for this is deferred until Section 6.2.

Reynolds number effects on laser beam deflection have been studied by changing the pressure in the test section, the velocities of the two gas streams, and/or the distance of the laser beam from the splitter plate. The Reynolds number, Re_x, is

defined by the following expressions.

$$Re_x \equiv \frac{x\Delta u}{\nu} = \frac{\rho x \Delta u}{\mu} = \frac{px\Delta u}{RT\mu} \tag{6.1}$$

The final form allows an accounting of all three controllable variables. The temperature, T, is fixed in this study because the run times are short and the laboratory temperature is constant. Figure 6.3 represents the lowest Reynolds number case, with succeeding Figures representing increasing Re_x. Reynolds number effects are first considered for θ_x^* and then θ_y^*.

The most noticeable effect of increasing Re_x is the increase in the random component of the θ_x^* traces (Figure 6.3 to 6.7). At first this is in the form of additional, small-scale, weak hesitations in the core-associated beam deflections (Figure 6.4). As Re_x is increased, those additional deflections increase in number and magnitude (Figures 6.5 and 6.6), until they can obscure the underlying beam signature that is so dominant in lower Reynolds number cases such as Figure 6.3. The strong random component makes it difficult to identify the negative peaks and positive-going deflections associated with the cusps.

The increased small-scale structure in the signal is associated with the increased three-dimensionality and mixing transition. As alluded to previously (this chapter and Section 2.2), although transition occurs quickly, its location undergoes rapid temporal variations. It could be that the reappearance of the canonical θ_x^* signature is due to a streamwise shift of the mixing transition to a point further downstream. In Figure 6.6, the signature reappears at 0.30s and 0.34s, after being obscured for $t < 0.29$s. In Figure 6.7, the signature is visible at $t = 0.15$s and 0.16s.

The most dramatic Reynolds number effects have been observed in the θ_y^*. Between Figures 6.3 and 6.7, there is a large increase in the overall magnitude of the θ_y^* fluctuations, particularly in the positive peaks occurring at the cusps. The θ_y^* deflections eventually equal and in some instances exceed θ_x^* (e.g., Figure 6.7, $t \doteq 0.15$ and 0.17s). However, at the highest Re_x examined, the positive spikes no longer dominate but exhibit a tendency to have either sign (Figures 6.7 and 6.8).

A comparison of the θ_x^* and θ_y^* data shows that, as the Reynolds number increases, the relative contributions of θ_x^* and θ_y^* to the optical distortions generated by the mixing layer change. At low Re_x, e.g., Figures 6.3 and 6.4, the major contributor to the distortions is θ_x^*, which is generated primarily by the spanwise coherent structures. At high Re_x, the contribution of the spanwise coherent structures has been supplemented by the θ_y^*, which is generated primarily by the streamwise coherent structures, e.g., Figure 6.8. Thus, at high Re_x, there are two major sources of optical distortions in caused by the mixing layer. As shall be seen in Section 6.3, at intermediate Re_x, the contribution due θ_y^* can greatly exceed that of θ_x^*.

6.2 Effects of Streamwise Coherent Structures

Previous studies of the streamwise structure of the turbulent mixing layer have shown the secondary vortices to be relatively stationary. Long time exposure plan-view shadowgraph pictures by Bernal (1981) reveal a series of regularly spaced vortices; these vortices clearly do not convect in the same manner as the spanwise structures (Section 2.2). The regular spacing of the structures implies that the behavior of the laser beam varies as a function of spanwise position.

Accordingly, the variation in the rms fluctuations of the streamwise and spanwise deflection angle ($\sigma_{\theta_x^*}$ and $\sigma_{\theta_y^*}$) and the mean value of the spanwise deflection angle ($\overline{\theta_y^*}$) as functions of the spanwise position of the laser beam in the flow are now considered. In the following discussion, the mean value of the streamwise deflection angle ($\overline{\theta_x^*}$) is not examined since it is relatively small and therefore is extremely sensitive to the relative displacement of the mixing layer between the He and N_2 freestreams. This sensitivity makes its comparison for different conditions unreliable; the effect is similar to what happens if one passes a laser beam through a prism while slowly rotating the prism slightly. The laser beam wanders back and forth purely due to the change in its incident angle.

The value of the rms fluctuations of the streamwise deflection ($\sigma_{\theta_x^*}$) varies slightly, depending on the downstream position, as the laser beam is moved across

the span. Figure 6.10 shows $\sigma_{\theta_x^*}$ and $\sigma_{\theta_y^*}$ plotted as functions of spanwise position for $x = 45$, 88, and 113 mm. The spanwise positions are 2 mm apart for 10 mm on either side of an arbitrary reference position near the centerline of the test-section. At $x = 45$mm, $\sigma_{\theta_x^*}$ displays negligible variation across the span, well with-in the uncertainty of approximately 7μrad for each point. The data indicate that, from the point of view of θ_x^*, the flow appears to be two-dimensional. At $x = 88$ mm, the $\sigma_{\theta_x^*}$ has peak-to-peak variations of about 25μrad, which is well outside the uncertainty level. The streamwise coherent structures are much more developed at this position, thus leading to the increased spanwise variability. Data for $x = 113$ mm shows less variation. The $\sigma_{\theta_x^*}$ is approximately 150μrad to 175μrad for all three cases.

The value of the rms fluctuations in the spanwise deflection angle ($\sigma_{\theta_y^*}$) exhibits more variability with spanwise position. At $x = 45$ mm, the peak-to-peak changes are about 150μrad (50μrad to approximately 200μrad). At $x = 88$ mm, the variation with y has increased greatly, most likely due to development of the streamwise vortices with x. At this position, the peak-to-peak variation has increased to 175μrad, as the rms magnitude now varies between 125μrad and 300μrad. At $x = 113$ mm, the peak-to-peak variation has fallen slightly, to 125μrad, as have the rms levels (150 to 275μrad). In all three cases, the maximum fluctuation levels at $y \doteq 1$ mm coincide very closely with a streamwise streak in a series of plan-view spark shadowgraphs, one of which is shown in Figure 6.11. In the $x = 88$ and 113 mm cases, the variations in $\sigma_{\theta_x^*}$ and $\sigma_{\theta_y^*}$ correspond very well with one another. Once the streamwise coherent structures develop, it is interesting that they cause similar behavior in the rms fluctuation for two orthogonal deflection angles. The implication is that each type of structure has associated with it refractive index gradients in two directions, which is a further indication of the three-dimensionality present in the flow.

Plots of $\overline{\theta_y^*}$ versus y show a cyclic variation at $x = 45$, 88, and 113 mm (Figures 6.12 a,b,c respectively). Figure 6.11, the plan-view spark shadowgraph picture, shows streamwise streaks at $y \doteq -8$ and 1 mm ($y = 0$ is shown with a larger

mark on it; the individual marks are 2 mm apart and are slightly upstream of where the laser beam actually traverses the mixing layer). On the $\overline{\theta_x^*}$ plots, these locations correspond to negatively sloped changes in deflection angle. Thus, light on the positive side of a zero crossing, for example $y \doteq 1$ mm (marked by arrows in Figures 6.12), is bent in a negative direction, while light on the negative side are bent in a positive direction. The streamwise streaks are formed where the light rays cross. The separation between successive zero-crossings of negatively sloped plots of deflection angle corresponds to the distance between streaks. The deflections decrease slightly at positions further downstream (see Figure 6.12c, for $x = 113$ mm), possibly reflecting reduced gradients of the refractive index.

6.3 Mixing Transition Effects

The importance of mixing transition to the character of a turbulent mixing layer has been discussed in Chapter 2 and a qualitative assessment of its effects on optical quality has been made in the high-speed light sheet photographs of Chapter 5. Using the quantitative deflection data acquired in the measurements of beam deflection, an assessment which confirms and enhances the findings of the last two sections can be made regarding the effects of mixing transition on the optical quality of turbulent mixing layers.

The downstream distance is scaled with the initial momentum thickness on the flow's high-speed speed (θ_1); θ_1 is calculated using estimates from shadowgraph pictures of the most amplified wavelength (λ_0) and the fact that $\theta_1 \doteq 30\lambda_0$ (Roshko, 1990). The values for θ_1 (Table 2) are thus estimates, but they scale properly between runs of different pressures and velocities. As such, θ_1 is proportional to $p^{-1/2}u^{-1/2}$. Appendix D discusses the estimate in greater detail.

The major effect of increasing Reynolds number, in a general sense, is to obscure the characteristic signature (Section 6.1) of the spanwise coherent structures because the small-scale structure of the deflection signals becomes stronger. The question of Reynolds number dependence is intertwined with mixing transition; even though

transition is more dependent on initial conditions and the downstream distance in the form of x/θ_1 (cf., Section 2.2), it is impossible to increase x/θ_1 without changing the Reynolds number.

As shown in Figure 6.13, $\sigma_{\theta_x^*}$ shows relatively small changes with increasing x/θ_1. After peaking at $x/\theta_1 \doteq 380$, the rms fluctuations decrease slightly before reaching an asymptote. For the smallest values of x/θ_1 , $\sigma_{\theta_x^*}$ is relatively small (approximately 100μrad), but non-zero, possibly because the Kelvin-Helmholtz instabilities have already caused the flow to roll up into the spanwise structures, thus setting up the essential aberrative structure of the flow. However, considering that x/θ_1 increases by approximately a factor of 10 across the figure, $\sigma_{\theta_x^*}$ does not change very much. Even from the peak at $x/\theta_1 \doteq 380$ to large x/θ_1 , $\sigma_{\theta_x^*}$ does not deviate far from 150μrad.

As indicated in Section 6.2, the variation in rms fluctuation across the span is relatively small at low x/θ_1, growing as the streamwise vortices develop with increasing downstream distance until reaching the maximum near $x/\theta_1 \doteq 380$, after which it gets smaller. In general, the $\sigma_{\theta_x^*}$ variation with x/θ_1 is consistent relative to each spanwise position (y). For example, the fluctuation levels at $y = 2$ mm are consistently greater than those at $y = 0$ mm, and the levels at $y = -4$ mm are consistently less. While this consistency in the spanwise variation can be taken as an indication of how stable the streamwise vortices are in their respective positions, it does not mean that on a short time scale the vortices are not moving from side-to-side.

The changes that $\sigma_{\theta_y^*}$ undergoes with increasing x/θ_1 are much more impressive than those for $\sigma_{\theta_x^*}$. The trend for $\sigma_{\theta_y^*}$ is the same as for $\sigma_{\theta_x^*}$, with most notable being the peak in magnitude and spanwise-related variation in values at $x/\theta_1 \doteq 380$. As shown in Figure 6.14, for $x/\theta_1 < 200$, $\sigma_{\theta_y^*}$ is essentially negligible compared to $\sigma_{\theta_x^*}$. However, as x/θ_1 increases, $\sigma_{\theta_y^*}$ increases rapidly, to a maximum of over 300μrad. For $x/\theta_1 > 380$, both the level and spanwise variation decrease rapidly to a level of the same magnitude as $\sigma_{\theta_x^*}$. At each spanwise position, the results across the

range of x/θ_1's examined are consistent both with the laser beam's position in the layer and with the results for $\sigma_{\theta_x^*}$. For example, the spanwise positions with high $\sigma_{\theta_y^*}$ are the same as those for $\sigma_{\theta_x^*}$ (e.g., $y = 2$ mm). The spread in $\sigma_{\theta_y^*}$ values across the span is much more distinctive than it is for $\sigma_{\theta_x^*}$, being of the same magnitude as the fluctuations themselves. This is apparently because the streamwise coherent structures are primary contributors to the rms fluctuation of the spanwise deflection angles.

For a range of x/θ_1 between approximately 200 and 500, the rms fluctuation $\sigma_{\theta_y^*}$ is greater than the streamwise fluctuations $\sigma_{\theta_x^*}$. Below $x/\theta_1 = 200$, the flow is still very two-dimensional and the streamwise coherent structures have not developed enough to generate the spanwise refractive index gradients necessary to produce significant fluctuations. The spanwise coherent structures, on the other hand, have already assumed the geometry, i.e., the roll-up into the vortical structures, which possesses the streamwise refractive index gradients needed to produce associated beam fluctuations. Above $x/\theta_1 = 500$, mixing transition and the increased three- dimensionality have homogenized the flow to the point where $\sigma_{\theta_x^*}$ and $\sigma_{\theta_y^*}$ are comparable, having a value of approximately 150 to 200μrad.

If $\sigma_{\theta_x^*}$ and $\sigma_{\theta_y^*}$ are plotted versus Re_δ instead of x/θ_1, we can see the same general trends observed in Figures 6.14 and 6.15. In the present plots, the mixing layer thickness δ is actually δ_{vis} since it is measured from side-view shadowgraph pictures. The generally accepted value of the large-scale Reynolds number at mixing transition is approximately 10^4 (Dimotakis, 1989 and Roshko, 1990), and, as expected, significant changes in the rms fluctuation level are observed at that Re_δ . It is important, however, to remember that these data represent time averages, and the mixing transition location is not stationary during the averaging period. The result is that the abruptness of mixing transition is not as apparent on a linear Re_δ plot as it is on a logarithmic Re_δ plot (Section 2.2).

In the $\sigma_{\theta_x^*}$ versus Re_δ plot (Figure 6.15), the rms fluctuation peak at $Re_\delta \doteq$ 16000 is approximately 100μrad, while for $Re_\delta > 16000$, the level is 150μrad. The

peak exceeds 200μrad, but because of the variations in flow structure across the span of the flow, there is a spread in rms fluctuation which decreases with increasing Re_δ.

The changes in $\sigma_{\theta_y^*}$ are more distinctive than those for $\sigma_{\theta_x^*}$. In Figure 6.16, at low Re_δ (less than 6300), the spanwise rms fluctuation is approximately 50μrad. By $Re_\delta \doteq 16000$, $\sigma_{\theta_y^*}$ has increased to a spanwise maximum of over 300μrad. The spread due to variations in spanwise structure is much larger (150 to 350 μrad). Then, very rapidly on a logarithmic scale, the fluctuation magnitudes and spread induced by the spanwise structure drops to 150 to 200 μrad by $Re_\delta \doteq 63000$.

7. POSITION TRACKING EXPERIMENTS FOR A UNIFORM DENSITY TURBULENT MIXING LAYER

The effects of a uniform density mixing layer on the transmission of a thin laser beam are investigated. The mixing layer consists of N_2, which is the high-speed gas, and a mixture of 32 percent mole fraction He and 68 percent Ar, which is the low-speed gas. As such, in contrast with the He/N_2 turbulent mixing layer discussed in the previous chapter, the Gladstone-Dale constant shift is negative since $\beta_{He-Ar} < \beta_{N_2}$ and approximately 1/3 that of a He/N_2 mixing layer (Table 4).

The uniform density turbulent mixing layer displays similar characteristics to the non-uniform density mixing layer. The general signature of the spanwise coherent structures is dominated by large, cusp-related excursions, and is discussed in Section 7.1. As is the case for the He/N_2 mixing layer, consideration of the effects of the instantaneous flow structure on light transmission shall be confined mainly to the spanwise coherent structures. The effects of the large-scale, streamwise vortices are examined only in a time-averaged sense in the form of spanwise traverses in Section 7.2. The effects of scaling with x/θ_1 are discussed in Section 7.3. Because the high-speed fluid is N_2, the θ_1 is much smaller than for the He/N_2 mixing layer, which allows x/θ_1 values to be investigated far downstream of mixing transition since the range of x is fixed by the physical dimensions of the test-section.

The momentum thickness is calculated using estimates of the most amplified wavelength as obtained from high-speed shadowgraphs (Roshko, 1990). Estimates are made across a range of conditions using the fact that θ_1 varies with $(pu/\nu)^{1/2}$, the details of the calculations are included in Appendix D.

7.1 Effects of Spanwise Coherent Structures

The uniform density mixing layer generates consistent and periodic deflections of the laser beam, which, in a broad sense, display structure-dependent features

observed previously (Section 6.1). However, the Gladstone-Dale constant shift ($\Delta\beta$) across the $N_2/He\text{-}Ar$ turbulent mixing layer is negative whereas $\Delta\beta$ is positive for the He/N_2 mixing layer. Because the Gladstone-Dale constant, and the refractive indices, of each gas are passive scalars (i.e., they are convected with the local flow without interaction), their distribution and mixing are controlled by whether the gas is high-speed or low-speed. Hence, an overall negative $\Delta\beta$ across the mixing layer implies that the polarity of the deflection signature across the layer is reversed compared to a case where $\Delta\beta$ is positive (as in the He/N_2 mixing layer).

This reversal in polarity is shown by Figure 7.1, in which typical segments of θ_x^* data point to the dependence of the beam signature on the spanwise coherent structure. From simultaneous hot-wire and side-view shadowgraphs, the hot-wire signal, which is relatively weak because of lack of contrast between the two gases, can be correlated to structure position in the same manner as it is in Chapter 6.

Carrying the correlation over to the beam deflection measurements, the cusps of the spanwise coherent structures, i.e., their trailing edges, are associated with rapid positive-to-negative swings in the streamwise deflection of the laser beam (θ_x^*). Starting from a positive peak in deflection angle, for example 'A' in Figure 7.1a, $t \doteq 0.235$s, as the cusp convects across the beam, we see a swing to a negative deflection angle ('B'). At this point the beam is passing through the braid region. As the braid convects past the laser beam, the deflection angle begins to swing back in the positive direction to 'C' at which point the laser beam encounters the leading edge of the core. As the core begins to cross the axis of the laser beam, the deflection angle hesitates momentarily. Then, once it is inside the core, the laser beam continues to progress in the direction of a positive deflection angle to a new positive peak at 'D', until the next cusp is encountered, at which time the signal repeats itself.

As the Reynolds number is increased, the small-scale structure of the θ_x^* signal gains strength and increasingly obscures the canonical signature. Using x/θ_1 as the parameter determining the onset of mixing transition, because θ_1 is small, at

any given flow condition and downstream position, transition and the associated appearance of the small-scale component are moved further upstream (see also Section 7.3). Thus, at the most benign condition at which data are acquired (Figure 7.1a), the large-scale signal only occasionally breaks through. From a side-view shadowgraph, the development of small-scale structure of the flow is striking and immediate (Figure 7.3, $x \doteq 25$ mm). As is the case for the He/N_2 mixing layer, the transition location moves up and downstream, and the streamwise location where the associated small-scale component of the deflection angle first appears also moves back and forth across the beam axis. When the mixing transition is downstream, the canonical signal is apparent; when the transition is upstream, the signal is supplemented and obscured by the small-scales.

7.2 Effects of Streamwise Coherent Structures

Unlike the He/N_2 turbulent mixing layer, the streamwise coherent structures are present almost from the splitter plate and their presence is reflected in the beam deflections in the spanwise direction. In the previous case (Chapter 6), the larger scales at the splitter plate in the form of a large θ_1 allow the flow to retain a large degree of two-dimensionality because more downstream distance is required before the streamwise vortices are formed (recall Figures 5.2 to 5.5 for low values of x). In the present case, the smaller scales at the splitter plate (i.e., a smaller θ_1) mean the early development, in physical space, of the streamwise structures; therefore, the flow is three-dimensional very soon after the mixing layer forms.

A plan-view shadowgraph of the flow (Figure 7.3) shows, for a region just downstream of the splitter plate, i.e., at small x/θ_1, smaller scales than are present in the He/N_2 mixing layer at similar flow conditions. This finer scale is a result of the momentum thickness on the high-speed side (θ_1) being smaller for the N_2 than for the He at equivalent flow settings (Tables 2 and 3), which allows the streamwise coherent structures to initially be more closely spaced. As the mixing layer develops, the counter-rotating vortex pairs which make up the streamwise structures (Section 2.2) merge and combine, with the result being that the spacing

between streamwise structures grows. For small x/θ_1, when the 1 mm diameter laser beam is traversed across the span at 1 mm increments, the relatively fine scale as compared to previous experiments (cf. Section 6.2) limits the resolution of the measurements, and in effect creates a localized spatial average which tends to smooth out the spanwise variations in the data. For large x/θ_1, the scales are larger, but the effect of the mixing transition is to make the flow more (not totally) homogeneous.

At each downstream position and flow condition tested, traverses are made for 1 mm increments for a total of 5 spanwise positions. From the traverse data, $\sigma_{\theta_x^*}$ and $\sigma_{\theta_y^*}$ are computed and shown in Figure 7.2 for five values of x/θ_1. The plots show that the rms fluctuation varies across the span of the flow and that this variation depends on the downstream position at which the measurement is made and on whether the measurement is of $\sigma_{\theta_x^*}$ or $\sigma_{\theta_y^*}$.

The variation in $\sigma_{\theta_x^*}$ follows a similar pattern as observed in the He/N_2 mixing layer (cf. Section 6.2). At low values of x/θ_1 (Figure 7.2a), $\sigma_{\theta_x^*}$ is between 40 and 50μrad, and increases with x/θ_1. At $x/\theta_1 = 357$ (Figure 7.2b), $\sigma_{\theta_x^*}$ has increased to between 50 and 60μrad, after which its range and magnitude decrease. By $x/\theta_1 = 1355$, the spanwise dependence is negligible, and the magnitude is approximately 55μrad.

The rms fluctuation $\sigma_{\theta_y^*}$ displays extremely rapid development with x/θ_1 (cf. Section 6.2), starting from being less than $\sigma_{\theta_x^*}$ at $x/\theta_1 = 250$ (Figure 7.2a) and surpassing it by $x/\theta_1 = 357$. The spanwise variation also changes with x/θ_1, from 20 to 35μrad at the $x/\theta_1 = 250$, to 55 to 80μrad at $x/\theta_1 = 357$, then back down to 70 to 80μrad by $x/\theta_1 = 1355$. In general, as is the case for the He/N_2 mixing layer, the spanwise variation in $\sigma_{\theta_y^*}$ closely tracks the spanwise variation in $\sigma_{\theta_x^*}$.

The correlations between different runs at a given spanwise position is not as consistent as is the case with the He/N_2 mixing layer. The most likely reason for this lack of consistency is that the spanwise scale size for low values of x/θ_1 is

much smaller because the momentum thickness in this flow is smaller. As discussed above, the plan-view shadowgraph (Figure 7.3), shows a much finer structure than is true for the He/N_2 mixing layer at equivalent pressures and velocities. The finer structure limits the resolution achievable with the 1 mm diameter laser beam traversing in 1 mm increments. Over the 4 mm and 5 positions examined, several streamwise structures are traversed with the laser beam completely covering the available area. At high values of x/θ_1, even though the streamwise structures have merged and the scales have become larger, the flow is in a post-transition state, and the resulting strong three-dimensionality and spanwise motion of the streamwise structures affects the time averaging process.

7.3 Mixing Transition Effects

The fact that θ_1 for the $N_2/He\text{-}Ar$ mixing layer is smaller than for the He/N_2 mixing layer implies that mixing transition physically takes place farther upstream, or, conversely, for a given downstream position, the x/θ_1 values are larger. While this makes examination of pre-transition flows in the uniform density mixing layer difficult because of the physical limitations of the facility, examination of post-transition flows beyond values available in the He/N_2 case is possible.

The effect of mixing transition on $\sigma_{\theta_x^*}$ and $\sigma_{\theta_y^*}$ is shown by the plots of Figure 7.4, which are actually the data of Figure 7.2 plotted against x/θ_1. Figure 7.4a, for $\sigma_{\theta_x^*}$, shows a relatively small change over the range of x/θ_1's tested (250 to 1355). From the smallest x/θ_1 tested ($x/\theta_1 = 250$), increasing x/θ_1 leads to a peak in rms fluctuations at $x/\theta_1 \doteq 350$. The peak is accompanied by an increase in the spanwise variation of the rms fluctuation (Section 7.2). For $x/\theta_1 > 350$, the plot suggests that $\sigma_{\theta_x^*}$ decreases slightly to a constant mean value of approximately 55μrad and the spanwise variations get smaller, most likely because the flow has become more homogeneous, in a time-average sense, as a result of having undergone mixing transition.

The effect of mixing transition on $\sigma_{\theta_y^*}$ is shown in Figure 7.4b. The changes

in $\sigma_{\theta_y^*}$ with increasing x/θ_1 are greater than for $\sigma_{\theta_x^*}$. At $x/\theta_1 \doteq 250$, the rms fluctuations of θ_y^* are much smaller then those for θ_x^*. Extrapolating upstream, it appears as if $\sigma_{\theta_y^*}$ approaches zero at approximately $x/\theta_1 = 150$ to 200, implying that upstream of that point the flow is largely two-dimensional. Progressing in the downstream direction, however, by $x/\theta_1 \doteq 350$, $\sigma_{\theta_y^*}$ has grown so rapidly that it now surpasses $\sigma_{\theta_x^*}$. The spanwise dependence of the rms fluctuations is also greater, as indicated by fact that the variation in the data with spanwise position is large, well outside the uncertainty of 5μrad. For values of x/θ_1 between 200 and 500, the streamwise vortices are experiencing rapid growth and development and the flow is in the process of undergoing mixing transition (Section 2.2). As with the He/N_2 mixing layer, the major contributors to spanwise beam deflections are the streamwise vortices. Past $x/\theta_1 \doteq 500$, the layer is in a post-transitional state, and as a result the spanwise variation of $\sigma_{\theta_y^*}$ decreases with increasing x/θ_1 . As with the $\sigma_{\theta_x^*}$ data, the $\sigma_{\theta_y^*}$ data seems to reach a constant level, in this case 70 to 80μrad. In both the $\sigma_{\theta_x^*}$ and $\sigma_{\theta_y^*}$ cases, the saturation and decreased spanwise dependency indicates and/or is a result of an increased homogenization of the flow.

8. DISCUSSION OF RESULTS

The results presented in Chapters 5, 6, and 7 cover two types of experiments, the high-speed light sheet photography and the beam tracking studies, and two types of turbulent mixing layers, unequal density and uniform density. Various results have been shown concerning the nature of the optical distortions and where they originate in the mixing layer structure, as well as the effects of mixing transition and Reynolds Number.

This chapter seeks to relate the various aspects of the study to each other and to offer some insights into how turbulent mixing layers, especially the large-scale structures, affect light transmission. The chapter begins with a discussion of the relationship between the flow structure, particularly the spanwise coherent structures, and the behavior of thin beams of light passing orthogonally through the plane of the mixing layer. The next section of the chapter discusses how the rms fluctuation of the beam deflection scales with the development of the mixing layer, and the final section examines the role of the interfaces between the two fluids in the layer in aberrating a light beam.

8.1 Relationship between Flow Structure and Beam Behavior

In building a conceptual model of the deflection signature of a spanwise coherent structure, the results of two different flows must be compared. The two flows bound a wide range of possible density ratios for a given velocity ratio: the uniform density flow of $N_2/He\text{-}Ar$ on one hand and the nonuniform ($\rho_1/\rho_2 = 1/7$) flow of He/N_2 on the other.

The streamwise deflection data from each flow look very much alike, implying that the structure causing the deflections is common to both mixing layers. However, since the signs of $\Delta\beta$ are different, the deflection signals are of opposite sign. The sign difference is removed by multiplying the data from the $N_2/He\text{-}Ar$ mixing layer by -1 and comparing the result directly with the data from the He/N_2 mixing layer (Figure 8.1). Although the data differ in magnitude because the $\Delta\beta$

magnitudes are different, the streamwise beam deflections from each flow generate a periodic asymmetric signal caused by the passage of large-scale coherent structures. The signal is characterized by the rapid, large-magnitude swing in θ_x associated with the passage of a cusp by the laser beam. The extremum (A in Figure 8.1) in deflection angle is upstream for the He/N_2 mixing layer and downstream in the case of the $N_2/He\text{-}Ar$ mixing layer and occurs just downstream of the cusp. As the cusp convects past the beam, the beam now encounters the braid, and the deflection angle swings to a new extremum of opposite sign (B in Figure 8.1), then starts to swing back, although generally at a more gradual rate. In both cases, as the beam encounters the leading edge of the core, it hesitates, then continues as the core convects past the beam (C to D in Figure 8.1). In addition to the basic signature, there is also a superimposed small-scale component, and with increasing Reynolds number and mixing transition, this component increases in strength.

The results suggest a model for beam deflection as shown in Figure 8.2, which associates each portion of the deflection signature with its corresponding region in the spanwise coherent structure. This model is two-dimensional and so cannot address the effect of the streamwise structures and three-dimensionalities associated with the mixing transition. Because the sketched trace is smooth, it is indicative of a pre-transition mixing layer. Also included in Figure 8.2 is a sketch of the effect of increasing Reynolds number; progress up to and through mixing transition results in the addition of a small-scale component to the basic signal. Depending on the length of the braid, the relative extent of the braid-induced part of the signal will change. If the structure spacing is small, the hesitation will occur more quickly after the positive peak (i.e., positive as drawn in Figure 8.2). In many of the data traces, it seems as if the braid region is extremely short, so the hesitation occurs very soon after the sharp rise.

The model suggests the origin of the spanwise-oriented bright streaks and spots present in the plan-view shadowgraphs (Sections 5.1 and 5.2). These streaks and spots are caused by *caustics*, which are the focussing of light beams into the same

point in space, thus raising the intensity of the light at that point, and overexposing the film (e.g., Figure 5.3). In a case where $\Delta\beta > 0$, such as for the He/N_2 turbulent mixing layer and Figure 8.2, positively sloped θ changes in time imply negatively sloped θ changes in space. As shown in Figure 8.2, the negative slope in space is indicative of caustics forming as the rays cross after passing through the mixing layer. While this is especially true of the large amplitude, negatively sloped θ_x curve at the cusp, it also holds true for any part of the curve which is negatively sloped. The additional regions of negative slope first appear at the leading edge of the core; in plan-view shadowgraphs, after the trailing-edge (cusp) caustics appear, one next sees the caustics associated with the leading edges of the vortex cores. Thus, each new negatively sloped region that occurs as a result of mixing transition represents the potential for another caustic to form. Therefore, the increasing strength of the small-scale component, which is associated with increased Reynolds number and mixing transition, is reflected in the growth in the number of caustics in the plan-view photographs.

In addition to its explanation of the relationship between a spanwise coherent structure and the deflection angle of a thin light beam, the model should encourage attempts at an alternative interpretation of the effects of the large-scale flow structure. From Equation (3.1), the deflection angle can be integrated with respect to x to calculate the wavefront shape W. Using the model signature, we can simulate a wavefront shape (Figure 8.4). Since the rays are orthogonal to the wavefront, negatively curved regions correspond to convergent wavefronts. As can be seen from Figure 8.4, these regions are the dominant features of the cusp.

8.2 Scaling Relationships for the $\sigma_{\theta_x^*}$ and $\sigma_{\theta_y^*}$

In presenting the rms fluctuation data in Chapters 6 and 7, no attempt is made to directly compare the results for the two gas combinations (He/N_2 and $N_2/He\text{-}Ar$) used in this study by using the full nondimensionalization provided for in Equation (3.18). Because the shift in the Gladstone-Dale constant across the mixing layer ($\Delta\beta$) in the He/N_2 experiments is several times that of the $N_2/He\text{-}Ar$

experiments, the magnitudes and rms fluctuations of the deflection angle are several times greater for the He/N_2 experiments. By scaling the results of each experiment by $\Delta\beta$, as suggested by Equations (3.18) and (3.10), the two experiments may be considered together. Accordingly, a new scaled rms fluctuation of the deflection angle ($\sigma_{\theta_{xSC}}$) is defined in the following relationship.

$$\sigma_{\theta_{xSC}} \equiv \frac{\sigma_{\theta_x^*}}{\Delta\beta} \tag{8.1}$$

The relation for $\sigma_{\theta_{ySC}}$ is the same.

The variation in $\sigma_{\theta_{xSC}}$ may be plotted against nondimensional downstream distance (x/θ_1) as shown in Figure 8.3. The data from both the unequal density (He/N_2) and equal density ($N_2/He\text{-}Ar$) experiments is plotted after appropriate scaling by Equation (8.1). The general agreement between the two experiments is good, and the results show that the relationships (3.18) and (8.1) provide a means of scaling out the differences due to the use of different gas combinations. The rms fluctuation appears to peak at a value of $x/\theta_1 \doteq 380$, after which it declines slightly and asymptotes to a value of approximately 0.6. The spanwise variation due to the presence of streamwise structures in the flow increases to a maximum at $x/\theta_1 \doteq 380$ and then decreases farther downstream.

The results for $\sigma_{\theta_{ySC}}$, shown in Figure 8.4, display similar agreement, except that the increase in rms fluctuation levels is much greater for $130 < x/\theta_1 < 380$. Beyond $x/\theta_1 \doteq 380$ the data show a decrease, then leveling off at $x/\theta_1 \doteq 800$, to a value of between 0.6 and 0.8. For low x/θ_1 (< 200), the spanwise vortices appear to be the principal cause of the optical aberrations induced by the flow. For $x/\theta_1 > 200$ and especially for $200 < x/\theta_1 < 800$, the streamwise structures make the major contribution to the aberrations.

A trend which is apparent upon close examination of Figures 8.3 and 8.4 is that the spanwise variation due to streamwise vortices is greater for the He/N_2 flow, even if the actual levels are generally similar. This difference may be attributed to the fact that the beam diameter (d), relative to the size of the streamwise structure,

is larger for the $N_2/He\text{-}Ar$ mixing layer than for the He/N_2 mixing layer. This is because θ_1 is smaller for the $N_2/He\text{-}Ar$ mixing layer; for a fixed x/θ_1, x is smaller, i.e., the laser beam is farther upstream in the $N_2/He\text{-}Ar$ layer than in the He/N_2 layer. Thus, the beam is in a region where the streamwise vortices are smaller and more closely spaced. Because d is unchanged relative to the scale sizes of the mixing layer, a higher degree of spatial averaging in the spanwise direction occurs in the case of the $N_2/He\text{-}Ar$ mixing layer, which reduces the measured spanwise variations in the data.

From the data, it appears that there is a close relationship between the onset of the mixing transition and the rapid increase in rms fluctuations in the deflection angle (as sketched in Figure 8.5). The mixing transition occurs at x/θ_1 values between 150 and 500, beyond which the flow has relaxed into full-scale turbulence (Bradshaw, 1966; Roshko, 1990). Thus, the peak in the rms fluctuation $\sigma_{\theta_{xSC}}$ and $\sigma_{\theta_{ySC}}$ occurs in the middle of the mixing transition. Previous studies in which a spanwise plane of the flow is visualized early in the mixing transition, a view similar to Figure 2.2, show a great deal of organization and tight, well-wrapped streamwise structures (Bernal, 1981 and Roshko, 1990). It is possible that the high degree of organization early in the mixing transition is the source of both strong refractive index gradients and, because the vortices are tightly wrapped, the many interfaces over which those gradients exist. The result is the high level of rms fluctuation which has been observed. Between $x/\theta_1 \doteq 380$, i.e., the peak in rms fluctuation, and $x/\theta_1 = 500$, the organization of the flow begins to break down and the flow starts to become more homogeneous; therefore, the rms fluctuation begins to decline. At x/θ_1 values greater than 500, the mixing transition is over and the combination of less organization and the presence of fluid mixtures of intermediate concentration (Section 2.2) serves to continue reducing the rms fluctuation. For very large x/θ_1's, the flow has become more homogeneous and, as pointed out in previous chapters, the rms fluctuation reaches an asymptote and the spanwise variations become smaller.

Chew (1991) discusses similar results for 1.0 cm and 6.5 cm diameter laser beams. Using Strehl Ratio (SR) as the diagnostic for beam aberrations, the study shows relatively constant, high SR levels prior to mixing transition, a sharp drop in SR starting at the beginning of mixing transition, and a leveling off after mixing transition. The results for the 6.5 cm beam show a lower SR than for the 1.0 cm beam. The bottom diagram in Figure 8.5 is a sketch showing how $1 - SR$, which is a measure of the aberrative quality of the flow, relates to mixing transition and the rms fluctuation of the beam bending angles. The aberrations $(1 - SR)$ induced by the flow on the 1 cm and 6.5 cm beams are low in the pre-transition regime, undergo a monotonic rise during transition, and level off in the post-mixing transition regime.

8.3 Comments on the Role of Interfaces

Past research on turbulent mixing layers shows that the mixing layer is inhabited by large-scale structures which, for a wide-range of Reynolds numbers, are composed of relatively uniform masses of fluid (Konrad, 1976; Koochesfahani and Dimotakis, 1986). These masses of fluid are large in size, on the order of the thickness (δ) of the mixing layer. Concentration measurements have shown them to be composed of pure high-speed fluid, pure low-speed fluid, or a relatively unique mixture of the two (Dimotakis, 1986, 1989). The light beam can only bend because of refractive index gradients; therefore, the presence of these large masses of uniform fluid implies that bending can only take place at the interfaces between the fluids. Thus, rather than being the result of a more or less continuous, random refractive index field of extremely small scale-size (i.e., Equation (1.1)), the deflection of a light beam can be thought of as being the result of a finite number of interactions with the thin interfaces separating the various large-scale bodies of fluid. Between these interfaces, the light travels in a straight line because the fluid is uniform.

A natural question is what constitutes the proper path length for light transmission. In the case of the continuously distributed refractive index field, the path length is δ. However, if the light beam deflection is mainly due to the interactions

with the fluid interfaces, then the appropriate path length is more of the order of the interface thickness.

Following Liepmann (1952), who discusses the deflection of a light ray passing through a boundary layer, and using Equation (3.18), we can estimate the path length requirement for the deflections measured in the experiments.

$$\frac{\theta_x}{K_1} = \int_{L_1}^{L_2} \frac{\partial c_2}{\partial x} dz \tag{8.2}$$

From Equation (8.2), if we were take the limit as the thickness of the gradient goes to zero, we would arrive at Snell's Law, which for extremely thin interfaces, could be a plausible means of estimating beam deflection.

Forming a mean square fluctuation using the assumption of large-scale disturbances, we get the following equation for two paths a and b which correlate together on the scale of the mixing layer.

$$\sigma_{\theta_x}{}^2 = K_1{}^2 \int \int_{L_1}^{L_2} (\frac{\partial c_2}{\partial x})^2 dz_a dz_b \tag{8.3}$$

Using the orders of magnitude for the various quantities in Equation (8.3), we can see that the following approximations may be made, where λ is the interface thickness and the σ_{θ_x} is typical for the experimental data.

$$K_1 \equiv \frac{p}{p_s}\frac{T_s}{T}\Delta\beta \sim (1)(1)(100 \times 10^{-6}) \tag{8.4}$$

$$\frac{\partial c_2}{\partial x} \sim \frac{1}{\lambda} \tag{8.5}$$

$$\sigma_{\theta_x} \sim 200 \times 10^{-6} \tag{8.6}$$

Substituting Equations (8.3) to (8.5) into Equation (8.3), we have the following.

$$(200 \times 10^{-6})^2 \sim (100 \times 10^{-6})^2 \frac{1}{\lambda^2}(\Delta L)^2 \tag{8.7}$$

From Equation (8.7), the path length $\Delta L \sim 2\lambda$. Thus, to an order-of-magnitude the path length required for the deflections observed in the experiments is the thickness

of the interface between the two fluids, not the thickness of the mixing layer. It is important to note that the the interfaces in question are mainly situated at the perimeter of the coherent structure, and are not distributed randomly inside the structure. As such, most of the aberrations will be a result of interactions taking place at the edges of the *structure* and not at the edges of the mixing layer as defined by δ.

The Taylor thickness can provide a suitable estimate of the interface thickness, and is given by the following relation (Broadwell and Mungal, 1991).

$$\lambda \sim \delta Re_\delta{}^{-1/2} \tag{8.8}$$

Taking the constant of proportionality to be of order 1, Re_δ of order 10^4, and δ of order 10 mm, the Taylor thickness (λ) is of order 0.1 mm, or about 100 times smaller than the mixing layer thickness.

Because of the presence of the large masses of uniform fluid in the mixing layer, the above argument shows that the deflections can occur only at the interfaces between the fluids. From the point-of view of the light, passage through the masses of fluid generates no aberrations; it is only upon encountering the gradients at the interfaces that the aberrations occur.

9. SUMMARY AND CONCLUSIONS

An investigation of how turbulent mixing layers affect light transmission has been conducted. To learn how coherent structures affect light transmission, beam deflections have been studied with high spatial and temporal resolution by using a network of thin, short duration light sheets as well as with a thin He-Ne laser beam tracked by a high speed lateral effect detector.

The turbulent mixing layer is dominated by the large-scale spanwise coherent (primary) structures. The large-scale structures cause the mixing layer to be highly anisotropic and inhomogeneous optically. The structures have a generic, asymmetric geometry; their general form is reflected in the streamwise deflection (θ_x^*) of a thin light beam. The thin light sheet photographs show largest deflections associated with the primary structures' trailing edge (cusp) where entrainment of the low speed fluid takes place. These deflections are dependent on the over-all refractive index shift (Δn) across the mixing layer. For positive Δn (e.g., the beam traverses from high-speed, low-n He to low-speed, high-n N_2), the beam deflections are in the upstream (negative) direction while for negative Δn (e.g., the beam traverses from high-speed, high-n N_2 to low-speed, low-n He-Ar) the deflection is in the downstream (positive) direction.

When the thin laser beam deflection data are studied in conjunction with hot-wire data and side-view shadowgraphs, it is possible to construct a general model of how the position of a primary vortex relative to the laser beam affects the beam's deflection angle (Figure 8.2). Progressing from upstream to downstream, the maximum deflection at the trailing edge is followed by decreasing magnitude through the core region to the braid, where the deflection is of opposite sign. The structure's leading edge is associated with momentary hesitation in the deflection angle. By extension, since the bending angle is the derivative of the wavefront shape, the model indicates how a coherent structure affects the shape of the wavefront of a broad, initially collimated, light beam. In particular, the trailing edges focus the light into caustics.

It has been shown that the initial momentum thickness of the high-speed side (θ_1) is an important governing parameter in judging optical quality when it is used to nondimensionalize downstream distance x as x/θ_1. As the mixing layer develops, it becomes three-dimensional because it develops streamwise or secondary coherent structures. This three-dimensionality introduces a spanwise (cross-stream) component of the bending angle of the light beam (θ_y). For low values of downstream distance (x/θ_1), the light sheet and thin beam results show that the θ_y deflections are small. As x/θ_1 grows, θ_y grows rapidly, and eventually reaches magnitudes equal to or greater than θ_x. Spanwise traverses show θ_x and θ_y dependence on spanwise position (both in mean and rms). The thin sheet photographs show this to be a spanwise focussing effect which can be associated with the streamwise flow structures. Mean θ_y measurements show focussing to be coincident with the streamwise streaks in plan-view shadowgraph pictures.

Mixing transition has important optical consequences. Measurements show that the the rms fluctuation of the beam deflection angle (both σ_{θ_x} and σ_{θ_y}) is maximized at $x/\theta_1 \doteq 380$. The relation is observed to hold for both equal density ($\rho_2/\rho_1 = 1$) and unequal density ($\rho_2/\rho_1 = 7$) turbulent mixing layers and appears to be true regardless of spanwise position. This location occurs within the region where the flow is undergoing mixing transition. In this experiment, pre-transition flow is associated with low values of total pressure, velocity, and/or downstream distance and under these conditions the thin sheet photographs exhibit little small-scale development and the thin beam data show regular θ_x temporal fluctuations and either regular or nonexistent θ_y fluctuations. Post-transition flow is associated with high values of pressure, velocity, and/or downstream distance. The contrast with pre-transition flow is striking in that the small scale, random fluctuations have greatly increased in magnitude, with the greatest change coming in θ_y. By comparison, the change in θ_x through transition is relatively small.

Furthermore, presumably as a consequence of the homogenization of post-transition flow, the spanwise dependency decreases. From $x/\theta_1 \doteq 380$, where the

rms variations across the span are greatest, the variations decrease steadily with increasing x/θ_1. By $x/\theta_1 \doteq 800$, there is very little difference in the rms fluctuation across the span.

Contrary to what has been generally assumed about light transmission through turbulent mixing layers, the light transmission and beam deflection appear to be the result of a finite number of interactions of the light beam with thin fluid-fluid interfaces (of the order of the Taylor thickness). These interfaces are the major source of the refractive index gradients needed for bending the light beam. The fluid between the interfaces is relatively uniform and thus generates little or no aberrations.

From the point-of-view of light transmission, these above results would indicate two strategies which may be appropriate for minimizing flow-induced optical aberrations. First, one wants to transmit light at low x/θ_1, prior to mixing transition, when the peak aberrations are relatively predictable and confined, and rms values are relatively low. Second, as an alternative, one can allow light transmission at high x/θ_1, where increased homogenization reduces spanwise variations in light transmission, albeit at higher overall fluctuation levels. In any case, it is best for optical transmission to be avoided for x/θ_1 values between 150 and 500.

The present study has shown that both the streamwise and spanwise large scale structures are as important to light transmission as they are to mixing. Previous statistical models assuming only homogeneity and isotropy may therefore be inadequate for reconciling theory and experiment because the anisotropy of the coherent structures is not taken into account.

REFERENCES

Bernal, L. P. (1981). The Coherent Structure of Turbulent Mixing Layers. I. Similarity of the Primary Vortex Structure., II. Secondary Streamwise Vortex Structure. *Ph.D Thesis*, California Institute of Technology.

Bradshaw, P. (1966). "The Effect of initial conditions in the development of a free shear layer," *J. Fluid Mech.*, **26**, 225–236.

Breidenthal, R. E. (1978). A Chemically Reacting, Turbulent Shear Layer. *Ph.D Thesis*, California Institute of Technology.

Broadwell, J. E. and Mungal, M. G. (1991). "Large scale structures and molecular mixing," *Phys. Fluids A*, **3**(5), 1193–1206.

Brown, G. L. and Roshko, A. (1974). "On Density Effects and Large Structure in Turbulent Mixing Layers," *J. Fluid Mech.*, **64**(4), 775–816.

Cantwell, B. J. (1981). "Organized Motion in Turbulent Flow," *Ann. Rev. of Fluid Mech.*, **13**, 457–515.

Chernov, L. A. (1960). *Wave Propagation in a Random Medium*, McGraw–Hill.

Chew, L. and Christiansen, W. H. (1990). "Coherent Structure Effects on the Optical Performance of Plane Shear Layers," *AIAA J.*, **29**(1) , 76–80.

Chew. L. and Christiansen, W. H. (1991). "Experimental Investigations of Free Shear Layer Optics," AIAA Paper 91-1722.

Coles, D. (1985). "The Uses of Coherent Structure," AIAA Paper 85–0506.

Dimotakis, P. E. (1986). "Two-Dimensional Shear Layer Entrainment," *AIAA J.*, **24** (11), 1789–1796.

Dimotakis, P. E. (1989). "Turbulent Free Shear Layer Mixing and Combustion," ISABE 89–7006, Ninth ISABE, Athens, Greece, 3–9 Sept 89.

Dimotakis, P. E. and Brown, G. L. (1976). "The Mixing Layer at High Reynolds Number: Large Structure Dynamics and Entrainment," *J. Fluid Mech.*, **78**(3), 535–560 + 2 plates.

Elliot, J. L. et al. (1989). "Image Quality on the Kuiper Airborne Observatory. I. Results of the first flight series." *Publ. of the Astronomical Soc. of the Pacific*, **101**, 737–764.

Gilbert, K. G. and Otten, L. J. (1982).*Aero–Optical Phenomena*, American Institute of Aeronautics and Astronautics.

Hesselink, L. and Sturtevant, B. (1988). "Propagation of Weak Shocks through a Random Medium," *J. Fluid Mech*, **196**, 513–553.

Hussain, A. K. M. F. (1983). "Coherent Structures–Reality and Myth," *Physics of Fluids*, **26**, 2816–2850.

Klein, M. V. (1970). *Optics*, John Wiley and Sons, Inc.

Kline, S. J., Reynolds, W. C., Schraub, F. A., and Runstadler, P. W. (1967). "The Structure of Turbulent Boundary Layers," *J. Fluid Mech.*, **30**, 741–773.

Konrad, J. E. (1976). An Experimental Investigation of Mixing in Two–Dimensional Turbulent Shear Flows with Applications to Diffusion–Limited Chemical Reaction. *Ph.D Thesis*, California Institute of Technology.

Koochesfahani, M. M. and Dimotakis, P. E. (1986). "Mixing and Chemical Reactions in a Turbulent Liquid Mixing Layer," *J. Fluid Mech.*, **170**, 83–112.

Liepmann, H. W. (1952). "Deflection and Diffusion of a Light Ray Passing Through a Boundary Layer," Report SM-14397, Douglas Aircraft.

Liepmann H. W. and Roshko, A. (1957). *Elements of Gasdynamics*, GALCIT Aeronautical Series, John Wiley and Sons, Inc.

Oster, D. and Wygnanski, I. (1982). "The Forced Mixing Layer Between Parallel Streams," *J. Fluid Mech.*, **123**, 91–130.

Roshko, A. (1990). "The Mixing Transition in Free Shear Flows," *Proceedings of NATO Advance Research Workshop on THE GLOBAL GEOMETRY OF TURBULENCE (Impact of nonlinear dynamics)*, Rota (Cadiz), Spain, 8–14 July, 1990.

Sutton, G. W. (1985). "Aero–Optical Foundations and Applications," *AIAA J.***23**(10), 1525–1537.

Tatarskii, V. I. (1971). *The Effects of the Turbulent Atmosphere on Wave Propagation*, Israel Program for Scientific Translation.

Truman, C. R. and Lee, M. J. (1990). "Effects of Organized Turbulence Structure on the Phase Distortion in a Coherent Optical Beam Propagating Through a Turbulent Shear Flow," *Physics of Fluids A*, **2**,(5), 851-857.

Tsai, Y. P. and Christiansen, W. H. (1990). "Two-Dimensional Numerical Simulation of Shear-Layer Optics," *AIAA J.*, **28**(12), 2092–2097.

Wang, C. (1984). The Effects of Curvature on Turbulent Mixing Layers. *Ph.D Thesis*, California Institute of Technology.

White, F. M. (1974). *Viscous Fluid Flow*, McGraw-Hill.

Winant, C. D. and Browand, F. K. (1974). "Vortex Pairing, the Mechanism of Turbulent Mixing Layer Growth at Moderate Reynolds Number," *J. Fluid Mech.*, **63**, 237–55.

APPENDIX A

Refractive Index for a Two Species Mixture

If we use the number density η, the following two equations are true.

$$n_1 = 1 + \beta_1 \left(\frac{\eta_1}{\eta_{s1}} \right) \tag{A.1}$$

$$n_2 = 1 + \beta_2 \left(\frac{\eta_2}{\eta_{s2}} \right) \tag{A.2}$$

For a mixture, the refractive index can be written as follows.

$$n = \frac{n_1 \rho_1 + n_2 \rho_2}{\rho_1 + \rho_2} \tag{A.3}$$

Equation (A.3) can be rewritten using the concentration c.

$$n = \frac{n_1 \eta_1 + n_2 \eta_2}{\eta_1 + \eta_2} \tag{A.4}$$

$$n = n_1 \left(\frac{\eta_1}{\eta_{tot}} \right) + n_2 \left(\frac{\eta_2}{\eta_{tot}} \right) \tag{A.5}$$

$$n = c_1 n_1 + c_2 n_2 = n_1 + c_2 \left(n_2 - n_1 \right) \tag{A.6}$$

Note that in Equation (A.6) $c_1 = 1 - c_2$.

Since $p_i = \eta_i R_i T_i$ for species i, Equations (A.1) and (A.2) are rewritten as follows.

$$n_i = 1 + \beta_i \frac{(p_i / R_i T_i)}{(p_{si} / R_i T_{si})} = 1 + \beta_i \frac{p_i}{p_{si}} \frac{T_{si}}{T_i} \tag{A.7}$$

In Equation (A.7) p_i is the partial pressure of species i. However, $p_i / p_{si} = p / p_s$ and $T_{si} = T$ for $i = 1$ and 2, which leads to Equation (A.8).

$$n_i = 1 + \beta_i \frac{p}{p_s} \frac{T_s}{T} \tag{A.8}$$

Thus, for a 2 species incompressible mixing layer we have Equation (A.9).

$$n = 1 + \frac{p}{p_s} \frac{T_s}{T} \left(\beta_1 + c_2 \left(\beta_2 - \beta_1 \right) \right) \tag{A.9}$$

APPENDIX B

Derivation of the Ray Equation

To relate refractive index fluctuations to the light transmission through the mixing layer, one must develop the ray equation. From Liepmann and Roshko (1957) we use Figure 3.2 to describe how the light rays bend in a field of fluctuating n. For light traveling at speed c, the transit time τ through a small distance ξ on the ray r_a is $\tau = d\xi/c$. For ray r_b, the time is expressed by Equation (B.1).

$$\tau = \frac{d\chi}{c - dc} \tag{B.1}$$

Since the rays are joined by common wavefronts the following holds.

$$\frac{d\xi}{c} = \frac{d\chi}{c - dc} \tag{B.2}$$

From Figure 3.2, $d\phi$ and $d\chi$ may be expressed as in Equations (B.3) and (B.4).

$$d\phi \doteq \frac{d\xi - d\chi}{d\eta} \tag{B.3}$$

$$d\chi = \frac{d\xi}{c}(c - dc) = d\xi\left(1 - \frac{dc}{c}\right) \tag{B.4}$$

Substituting Equations (B.3) and (B.4) into (B.2) results in the following.

$$\frac{d\phi}{d\xi} = \frac{1}{c}\frac{dc}{d\eta} \tag{B.5}$$

The definition of index of refraction gives us an expression for dc.

$$dc = c_o d\left(n^{-1}\right) = -c_o\frac{dn}{n^2} \tag{B.6}$$

From Equation (B.6), we can say $dc/d\eta = -c_o/n^2$. Therefore, the following relationship holds true (Liepmann and Roshko, 1957).

$$\frac{d\phi}{d\xi} = -\frac{1}{n}\frac{dn}{d\eta} \tag{B.7}$$

APPENDIX C

Ray Trace Integral

For small deflections, $d\eta \doteq \frac{1}{\sin\alpha} dy \doteq dy$. Therefore, $d\phi/d\xi$ may be expressed by Equation (C.1).

$$\frac{d\phi}{d\xi} \doteq \frac{-1}{1 + \frac{p}{p_s}\frac{T_s}{T}\left(\beta_1 + c_2\left(\beta_2 - \beta_1\right)\right)} \frac{p}{p_s}\frac{T_s}{T}\left(\beta_2 - \beta_1\right)\frac{\partial c_2}{\partial y} \qquad (C.1)$$

Since we are dealing with a coordinate system based on the mixing layer (Figures 3.1 and 3.2), we must transform Equation (C.1) according to the following relationships, where w=wavefront, m=mixing layer.

$$dy_w = -dx_m \qquad (C.2)$$

$$dx_w = dz_m \qquad (C.3)$$

$$d\xi \doteq dx_w = dz_m \qquad (C.4)$$

Therefore, Equation (C.1) becomes as follows.

$$\frac{d\phi}{dy_m} \doteq \frac{1}{1 + \frac{p}{p_s}\frac{T_s}{T}\left(\beta_1 + c_2\left(\beta_2 - \beta_1\right)\right)} \frac{p}{p_s}\frac{T_s}{T}\left(\beta_2 - \beta_1\right)\frac{\partial c_2}{\partial z} \qquad (C.5)$$

Integrating across the mixing layer, dropping the m subscript and recalling Equation (3.8), we get Equation (C.6).

$$\theta_x = \frac{p}{p_s}\frac{T_s}{T}\Delta\beta \int_{L_1(x,y,t)}^{L_2(x,y,t)} \frac{\partial c_2/\partial x}{1 + \frac{p}{p_s}\frac{T_s}{T}\left(\beta_1 + c_2\Delta\beta\right)} dz \qquad (C.6)$$

Note that $\Delta\beta \equiv \beta_2 - \beta_1$. The equation for θ_y is similar in that it depends on the transverse gradient $\partial c_2/\partial y$.

APPENDIX D

Momentum Thickness Calculation

The momentum thickness is calculated for each test condition for the purpose of nondimensionalizing downstream distance x. It is based on the following correlation between the most amplified initial wavelength λ_0 and the initial momentum thickness (θ_1) on the high-speed side (Roshko, 1990).

$$\lambda_0 \doteq 30\theta_1 \qquad (D.1)$$

From a shadowgraph taken in the Brown-Roshko facility, Roshko (1990) measured the most amplified initial wavelength (λ_0) and calculated values of Rx/λ_0 for the purpose of investigating the relationship between vortex pairing and mixing transition ($R = (u_1 - u_2)/(u_1 + u_2)$). Using the values of Rx/λ_0 for the condition $p = 4$ bar, $u_2 = 3.8$ m/s, and $u_1 = 10.0$ m/s, a value of $\lambda_0 = 5$ mm is calculated, from which Equation (D.1) yields $\theta_1 = 0.17$ mm. The location of mixing transition is 69 mm, which gives $x/\theta_1 = 419$.

The value of θ_1 is then checked by noting the transition location in another picture taken at the same conditions, for which $x/\theta_1 = 369$. Since transition occurs in a range of x/θ_1 values slightly below 500, the estimate $\theta_1 \doteq 0.17$ mm is valid for a condition of $p = 4$ bar, $u_2 = 3.8$ m/s, and $u_1 = 10.0$ m/s.

The known value for θ_1 at a particular condition can now be scaled to other conditions and gases by noting the following relationship (White, 1974).

$$\theta_1 \propto \left(\frac{\mu}{pu}\right)^{\frac{1}{2}} \qquad (D.2)$$

The scaling is valid because the constant of proportionality is an integral based mostly on the geometry of the contraction section, which is the same for all of the experiments conducted in the facility. As a check, θ_1 at $p = 6$ bar, $u_2 = 1.9$ m/s, and $u_1 = 5.0$ m/s is calculated using Equation (D.2) and found to be 0.19 mm. The transition location is measured on the photograph to be 76 mm. From this, $x/\theta_1 \doteq 400$, which again provides good agreement with the above estimates. Tables 2 and 3 show the calculated θ_1's for the conditions tested.

TABLES

Table 1

Experimental Conditions for

High Speed Light Sheet Photography

$1 \equiv He$, $2 \equiv N_2$

p(bar)	u_1(m/s)	u_2(m/s)	$\frac{Re_x}{x}(\times 10^{-6})(\mathrm{m}^{-1})$	$\Delta n(\times 10^4)$
2.0	5.0	1.9	0.44	5.24
2.0	10.0	3.8	0.86	5.24
4.0	5.0	1.9	0.86	10.48
4.0	10.0	3.8	1.78	10.48
6.0	5.0	1.9	1.33	15.72
6.0	10.0	3.8	2.68	15.72

Table 2

Experimental Conditions for

Position Tracking Experiments (He/N_2)

$1 \equiv He$, $2 \equiv N_2$

p(bar)	u_1(m/s)	u_2(m/s)	θ_1(mm)	$\frac{Re_x}{x}(\times 10^{-6})$ (m^{-1})
2.0	5.0	1.9	0.33	0.44
2.0	10.0	3.8	0.23	0.86
4.0	3.8	1.4	0.27	0.67
4.0	5.0	1.9	0.23	0.86
4.0	10.0	3.8	0.16	1.78
6.0	3.8	1.4	0.22	1.00
6.0	5.0	1.9	0.19	1.33
6.0	10.0	3.8	0.14	2.68

Note: $\frac{Re_x}{x} = \frac{Re_\delta}{\delta}$

Table 3

Experimental Conditions for

Position Tracking Experiments ($N_2/He\text{-}Ar$)

$1 \equiv N_2$, $2 \equiv He\text{-}Ar$

p(bar)	u_1(m/s)	u_2(m/s)	θ_1(mm)
4.0	2.5	0.95	0.120
4.0	5.0	1.90	0.083

Table 4

Gladstone-Dale Constants

Gas	$\beta \times 10^4$	$\Delta\beta \times 10^4$
N_2	2.97	–
He	0.36	–
$He\text{-}Ar$	2.00	–
He/N_2	–	2.61
$N_2/He\text{-}Ar$	–	0.97

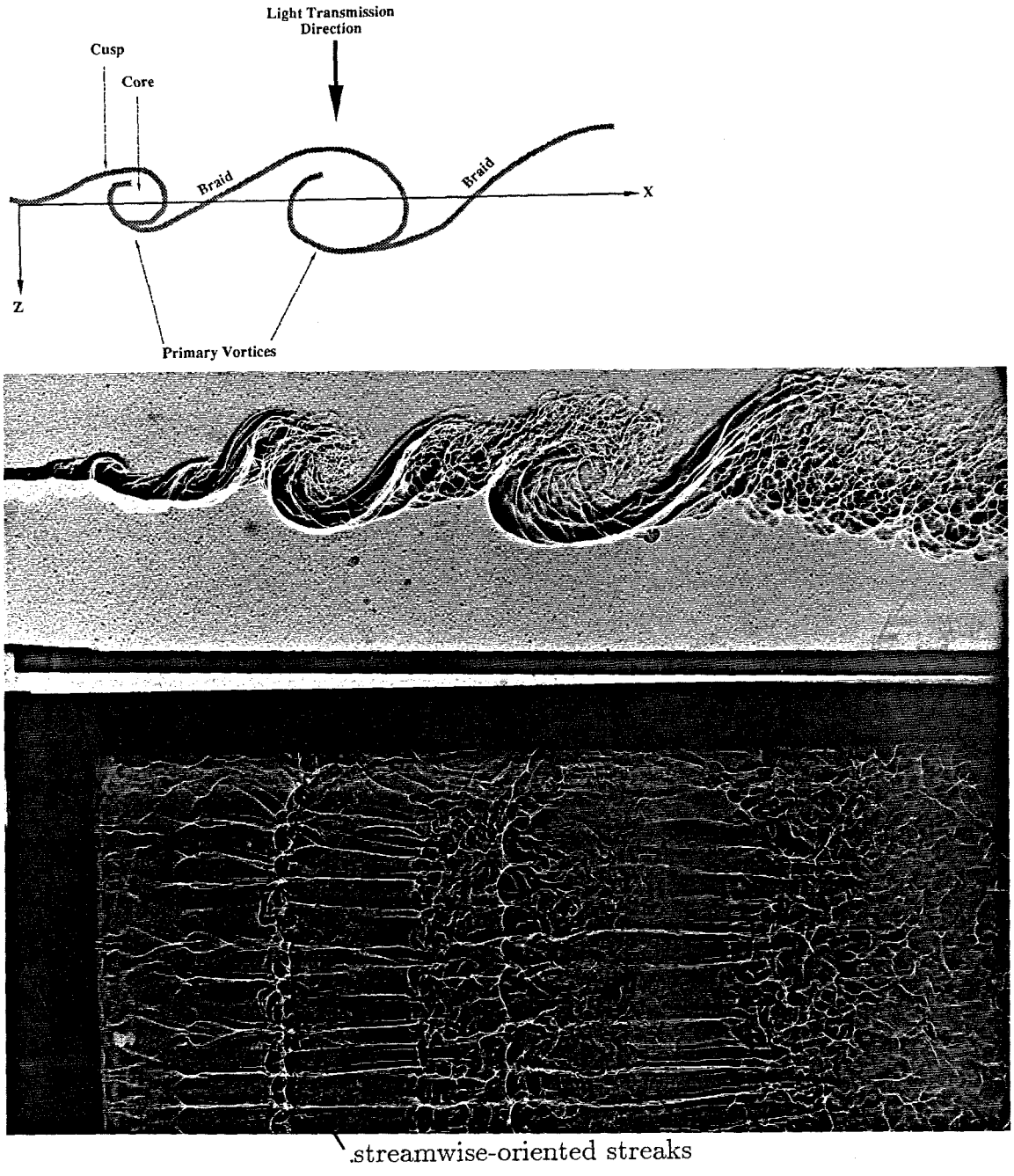

Figure 2.1–Turbulent Mixing Layer–diagram (top), side-view (middle), plan-view (bottom).

(a)

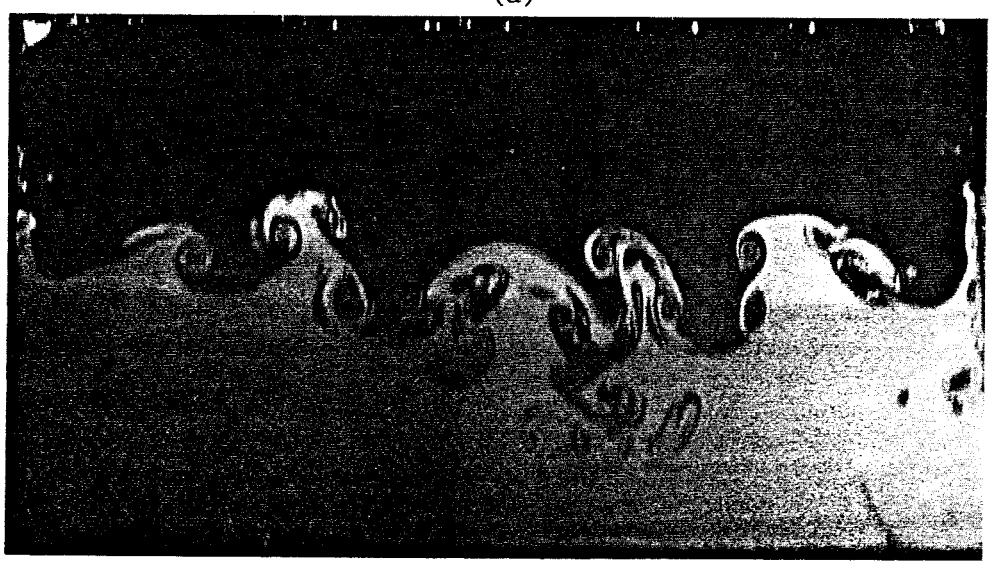

(b)

Figure 2.2–Streamwise Vortex Pairs (from Bernal, 1981).

(a) Cross-section through the core.
(b) Cross-section through the braid.

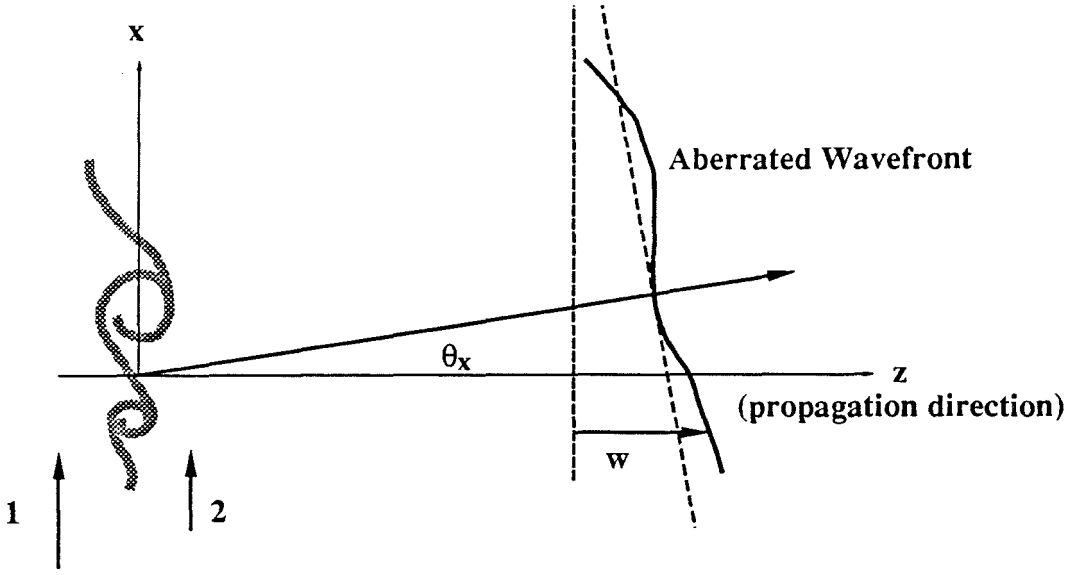

Figure 3.1–Coordinate System, Mixing Layer, and Wavefront.

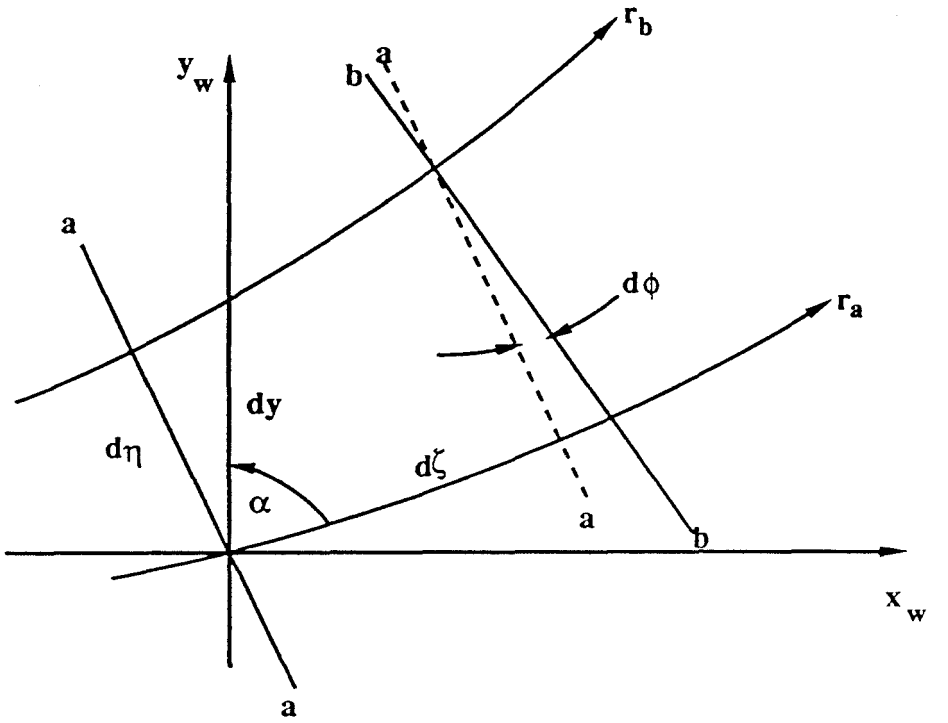

Figure 3.2–Rays and Wavefronts.

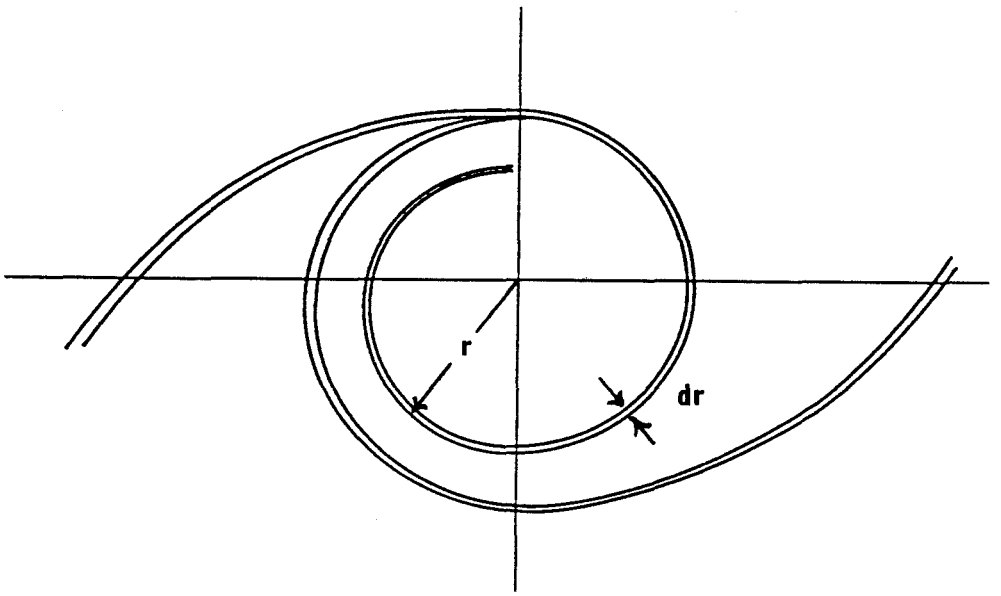

Figure 3.3–A Simple Model of a Coherent Structure.

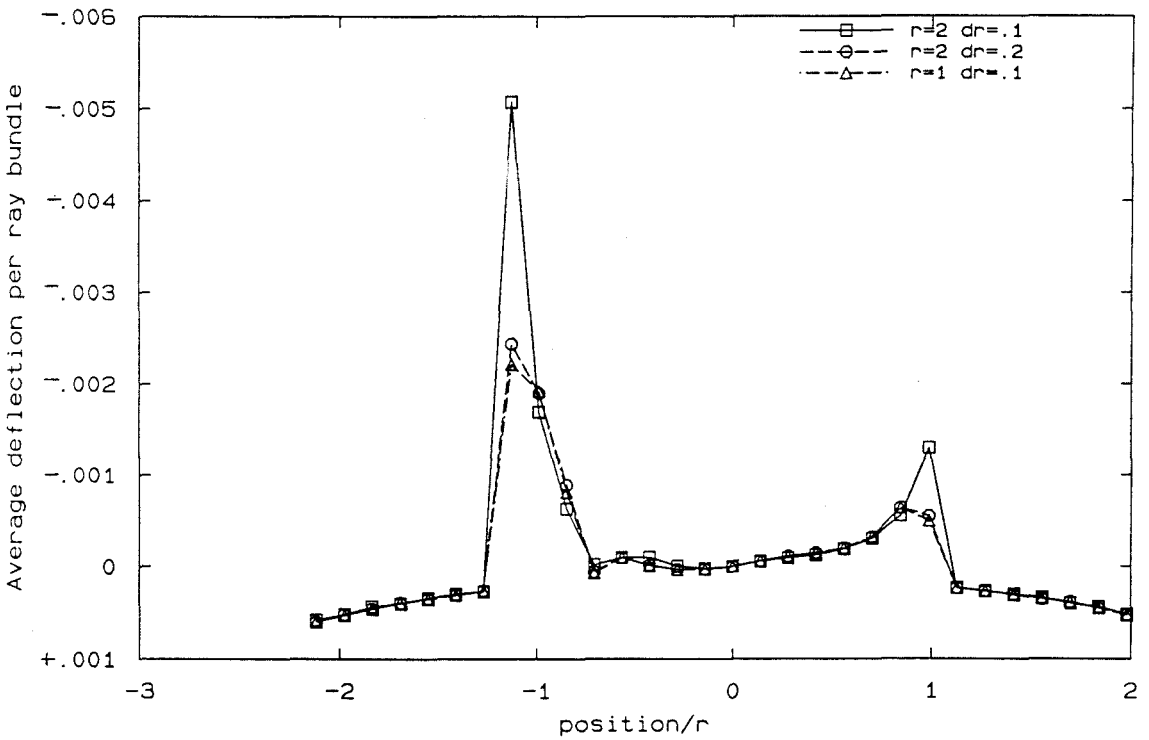

Figure 3.4–Results of Ray Trace.

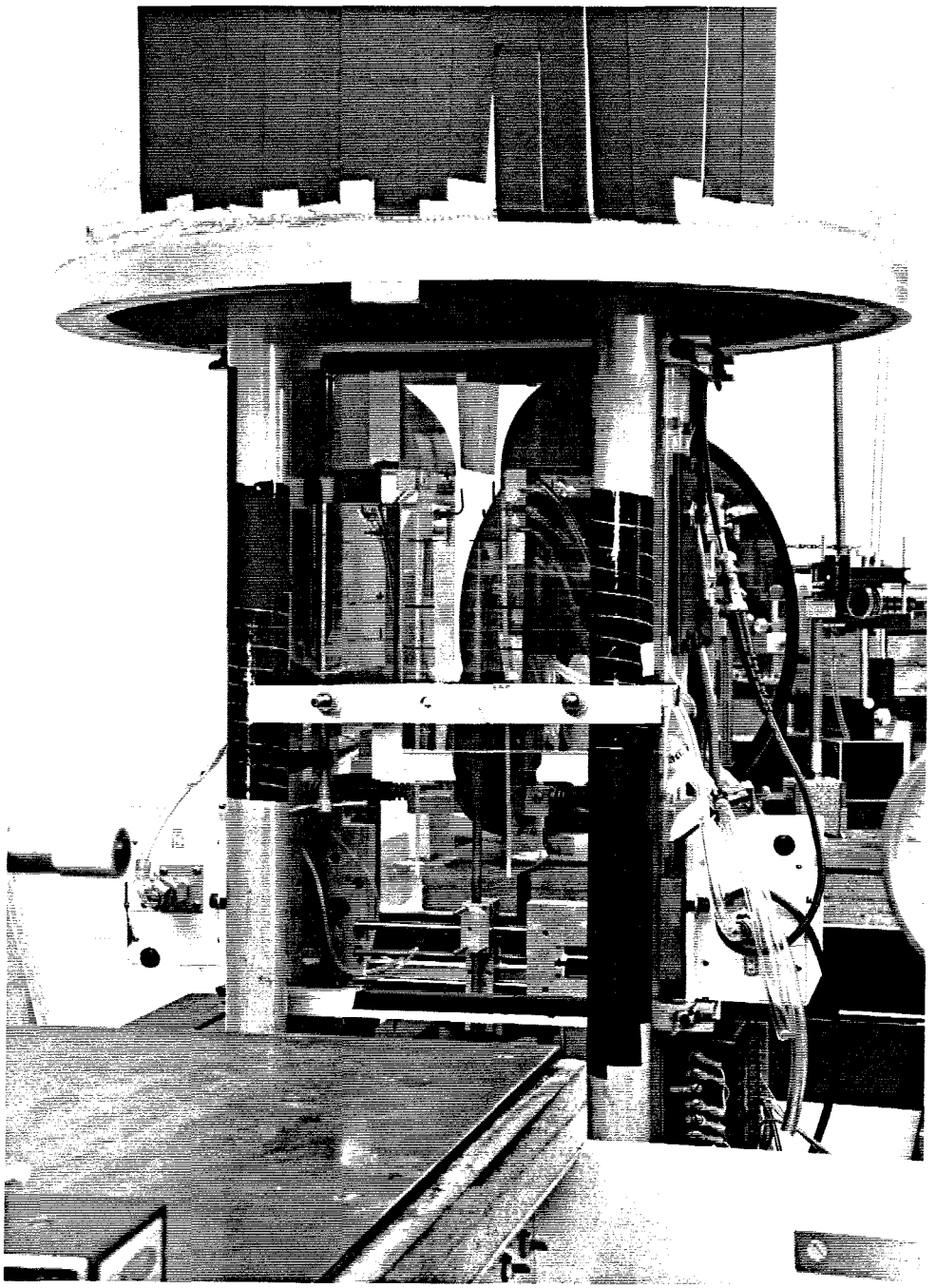

Figure 4.1–Brown-Roshko Gas Mixing Layer Facility.

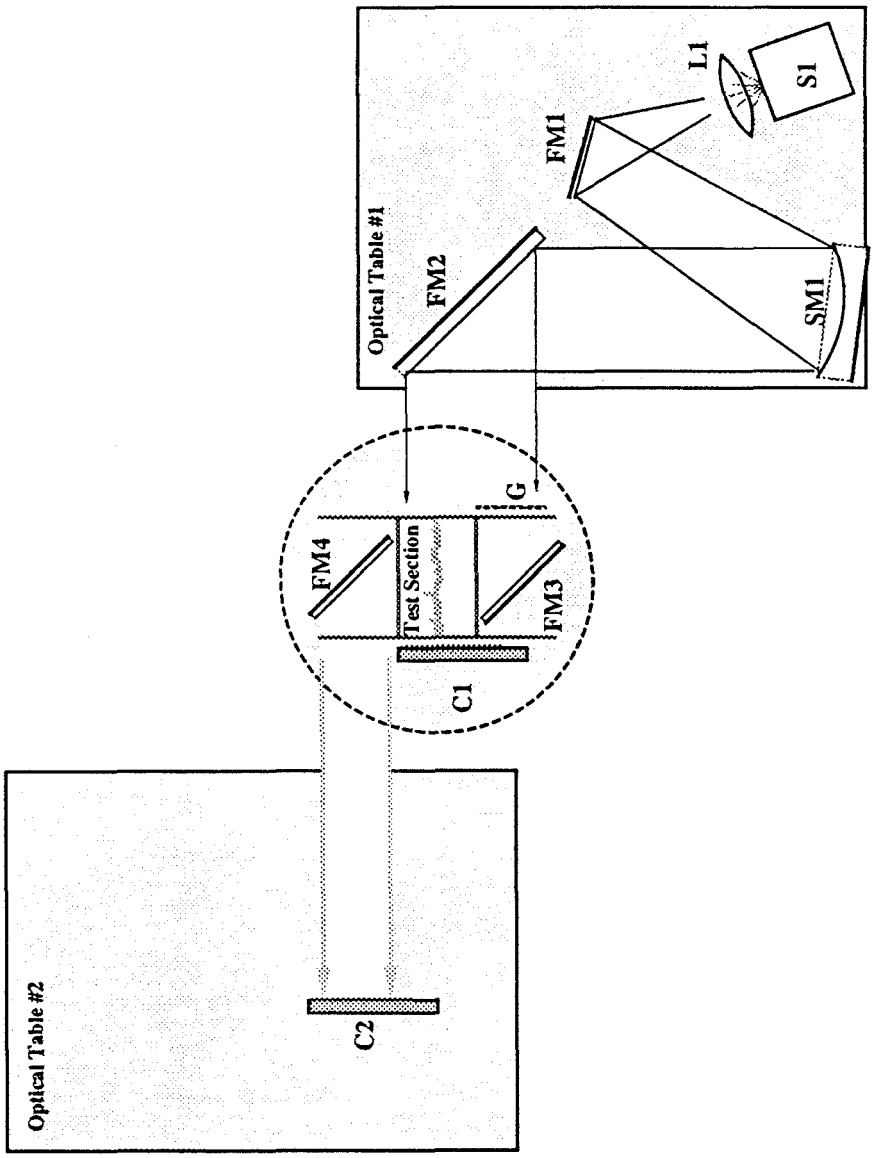

Figure 4.2–Set-up for High-Speed Thin Sheet Photography.

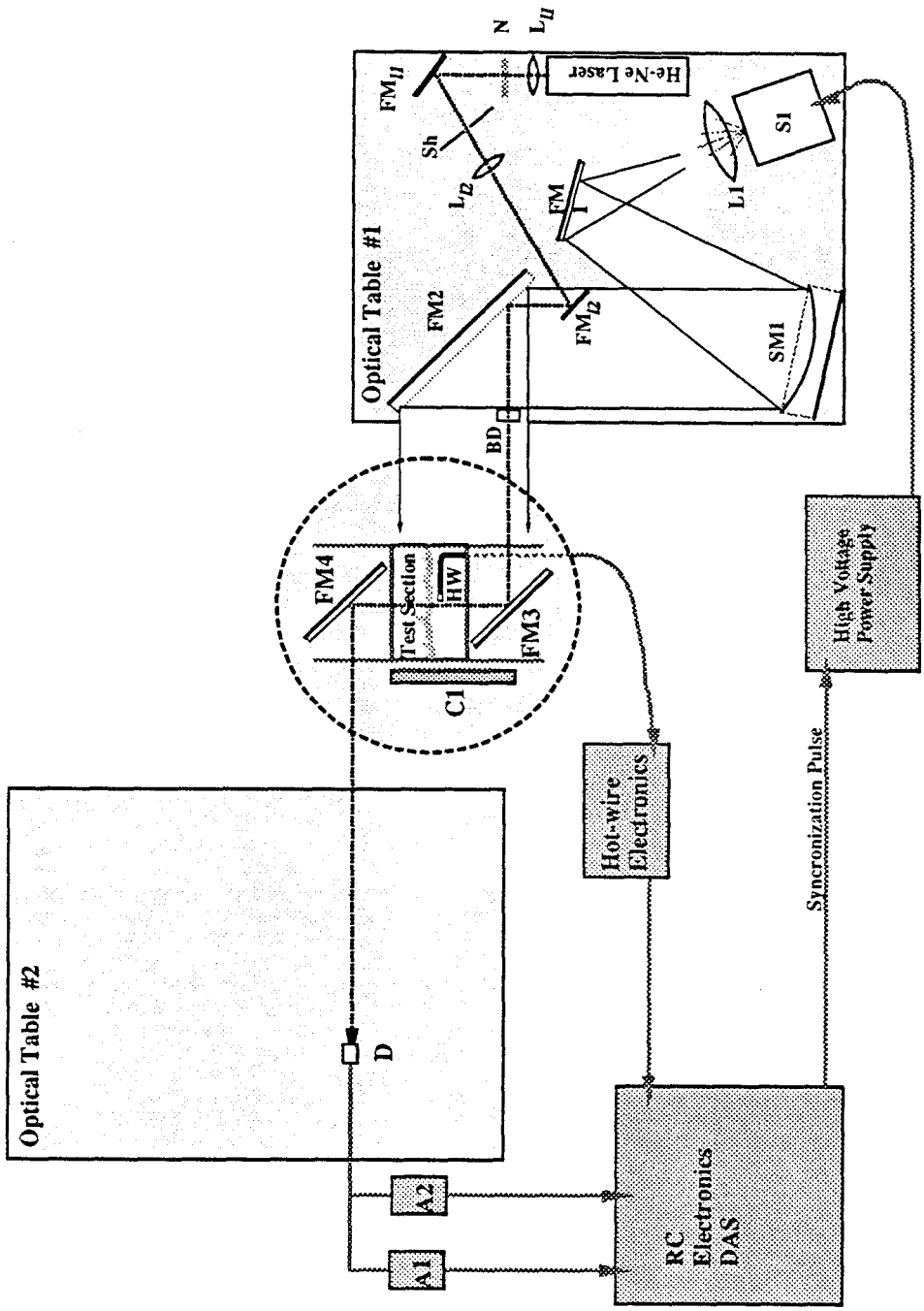

Figure 4.3–Set-up for Position Tracking Experiments.

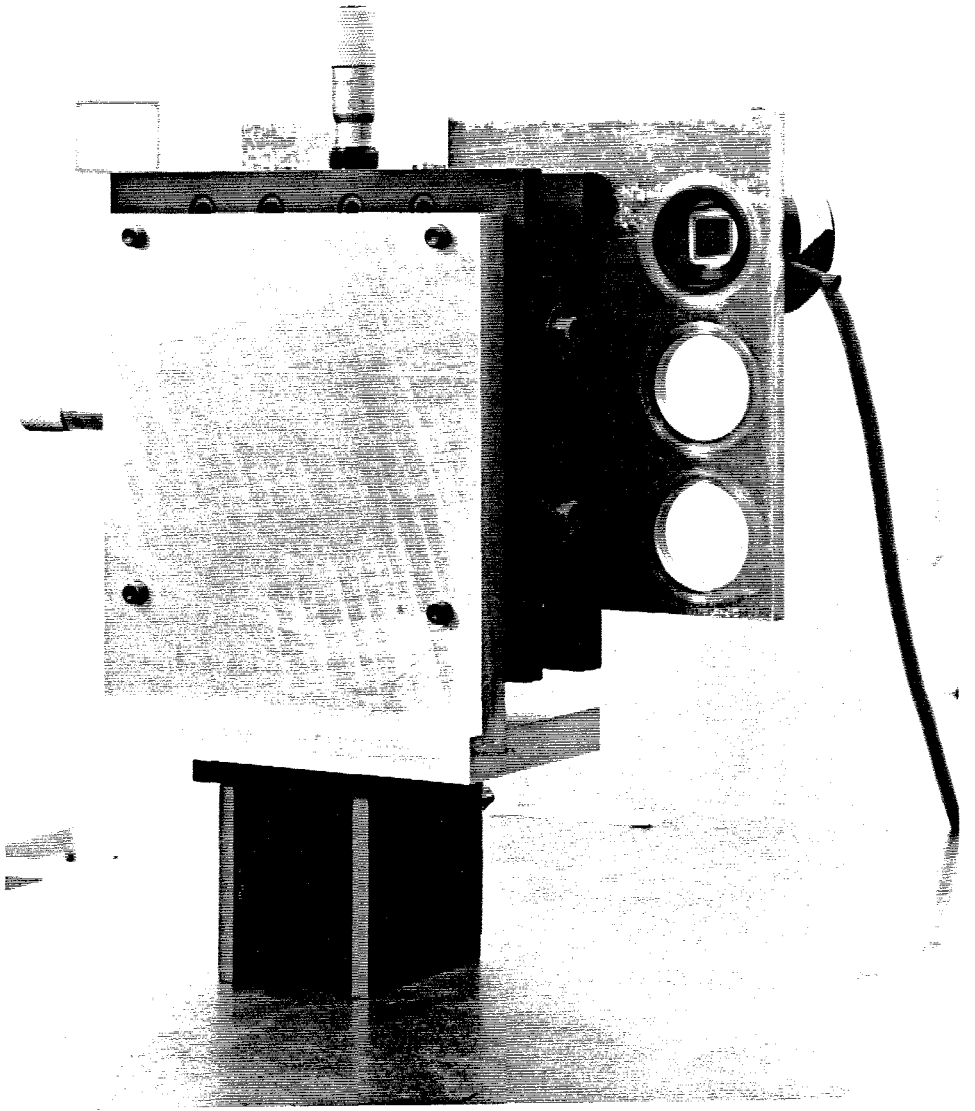

Figure 4.4–Lateral Effect Detector mounted on a Translation Stage.

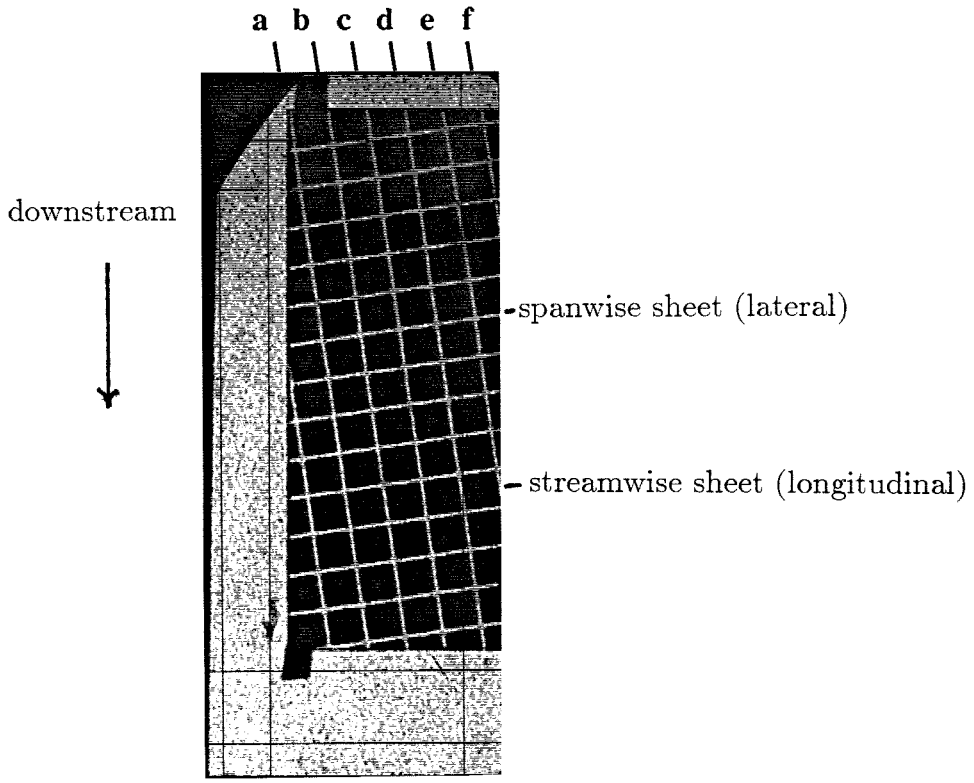

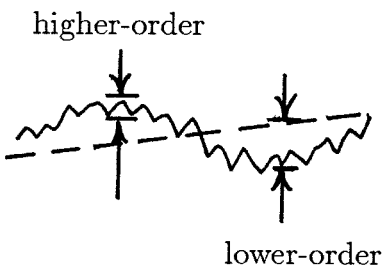

Figure 5.1–Orientation and Terminology for Thin Sheet Results.

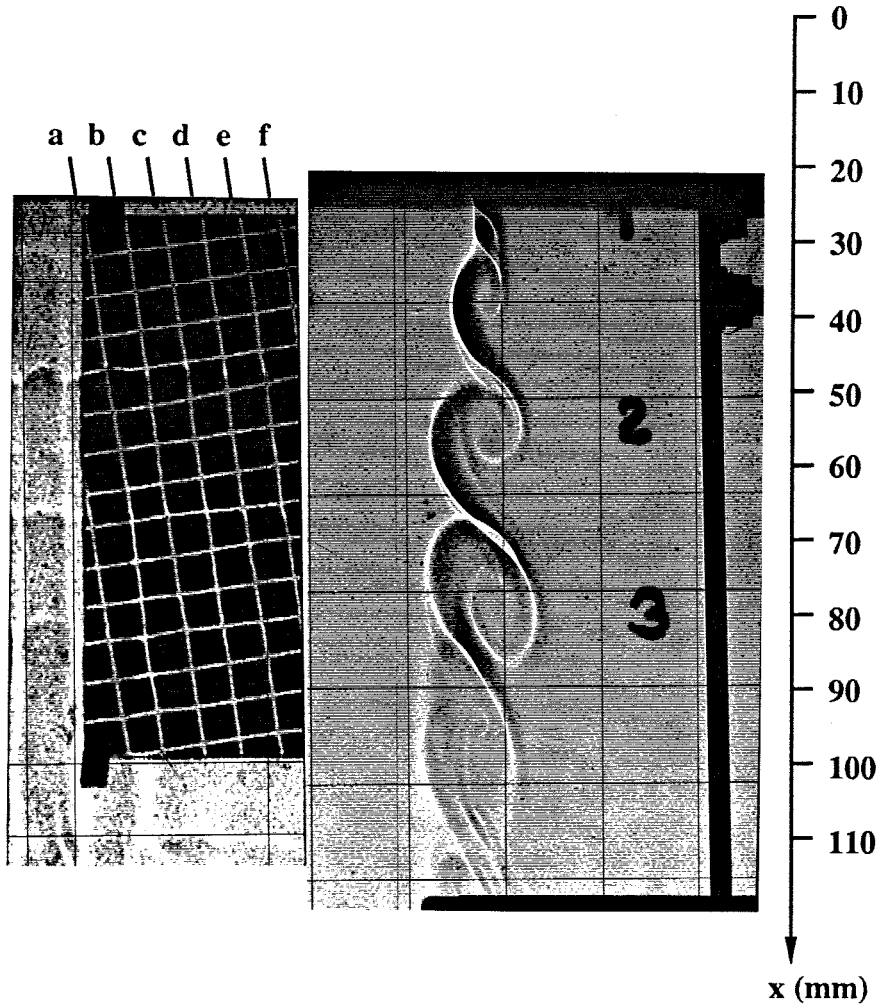

Figure 5.2–Light Sheets ($p = 2\text{bar}$, $u_2 = 1.9\text{m/s}$, $u_1 = 5.0\text{m/s}$, $L = 559\text{mm}$).

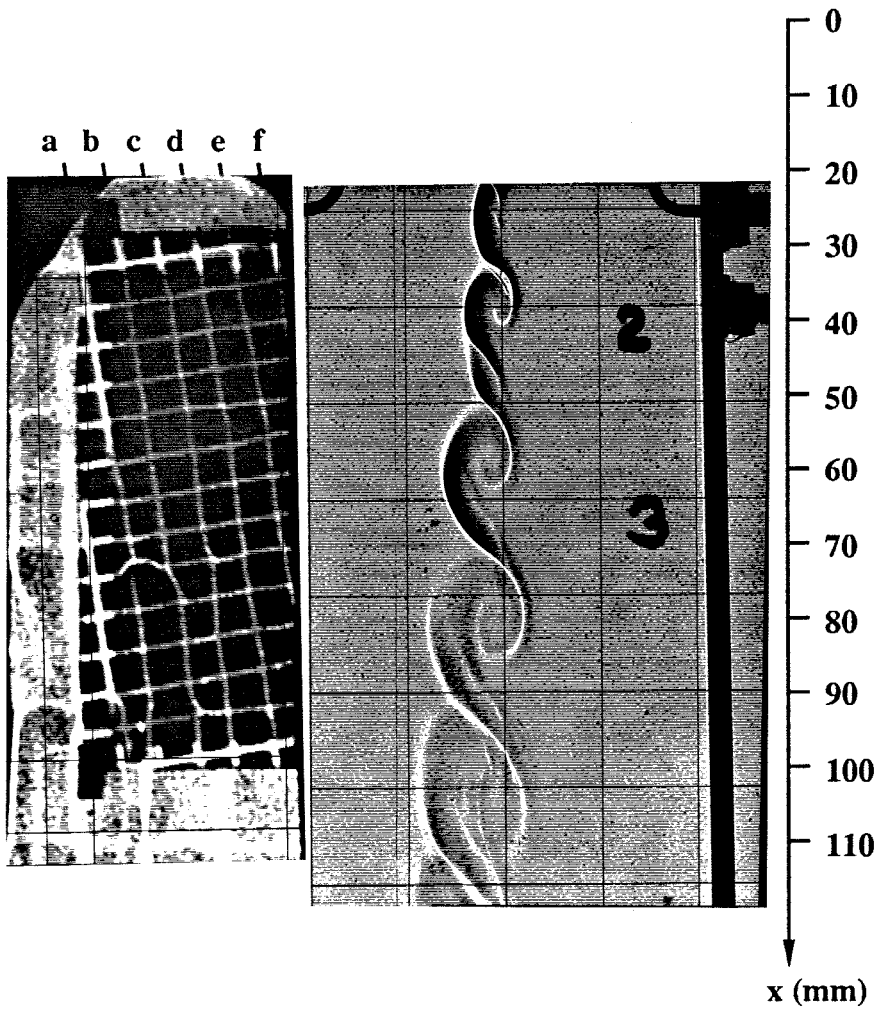

Figure 5.3–Light Sheets ($p = 2\text{bar}$, $u_2 = 1.9\text{m/s}$, $u_1 = 5.0\text{m/s}$, $L = 1118\text{mm}$).

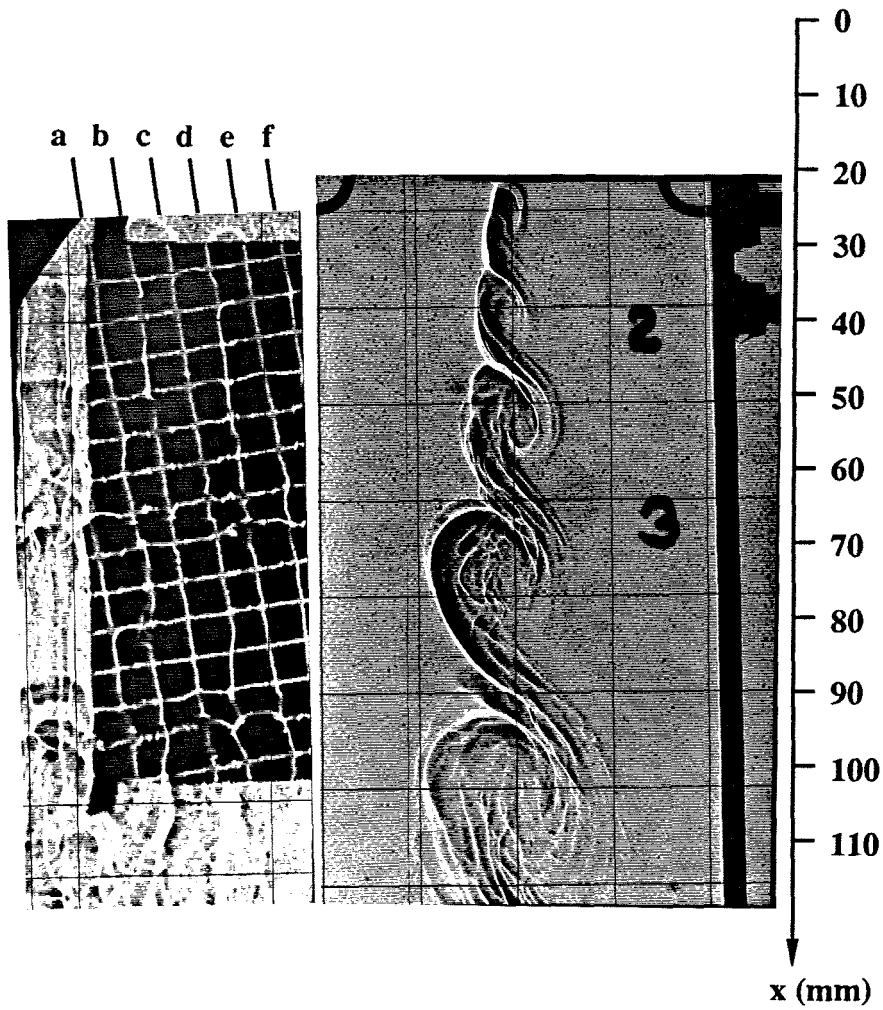

Figure 5.4–Light Sheets ($p = 2\text{bar}$, $u_2 = 3.8\text{m/s}$, $u_1 = 10.0\text{m/s}$, $L = 559\text{mm}$).

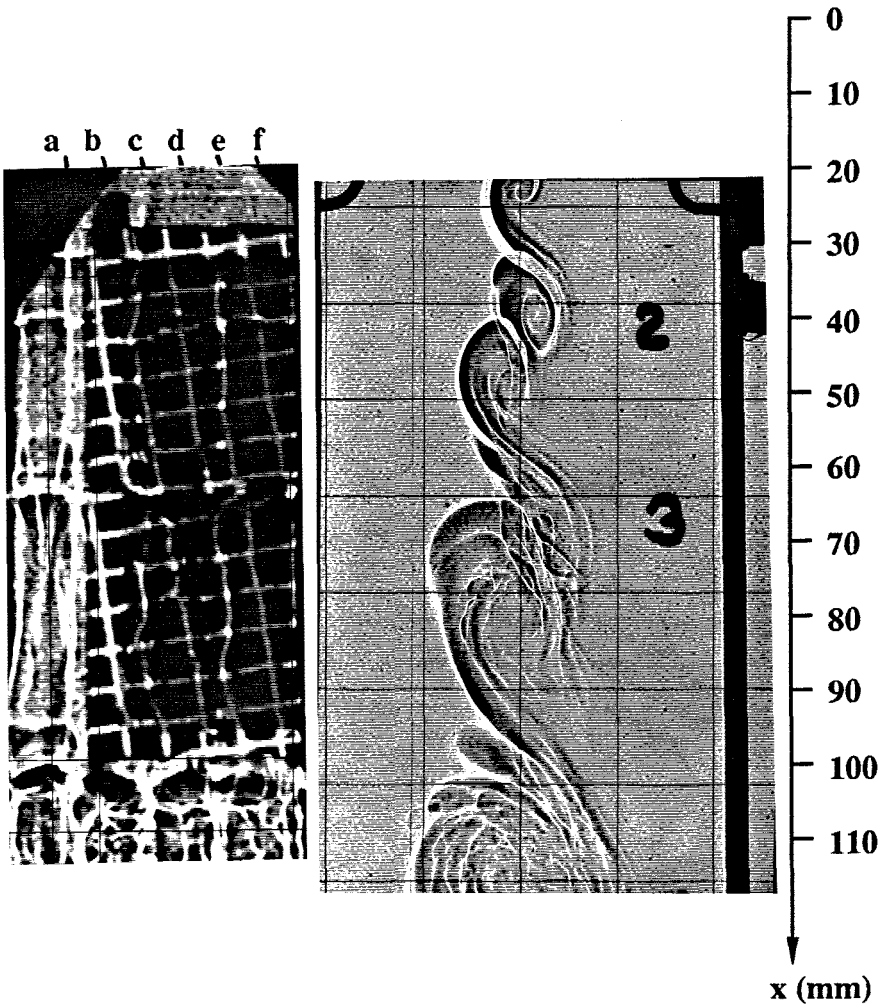

Figure 5.5–Light Sheets ($p = 2\text{bar}$, $u_2 = 3.8\text{m/s}$, $u_1 = 10.0\text{m/s}$, $L = 1118\text{mm}$).

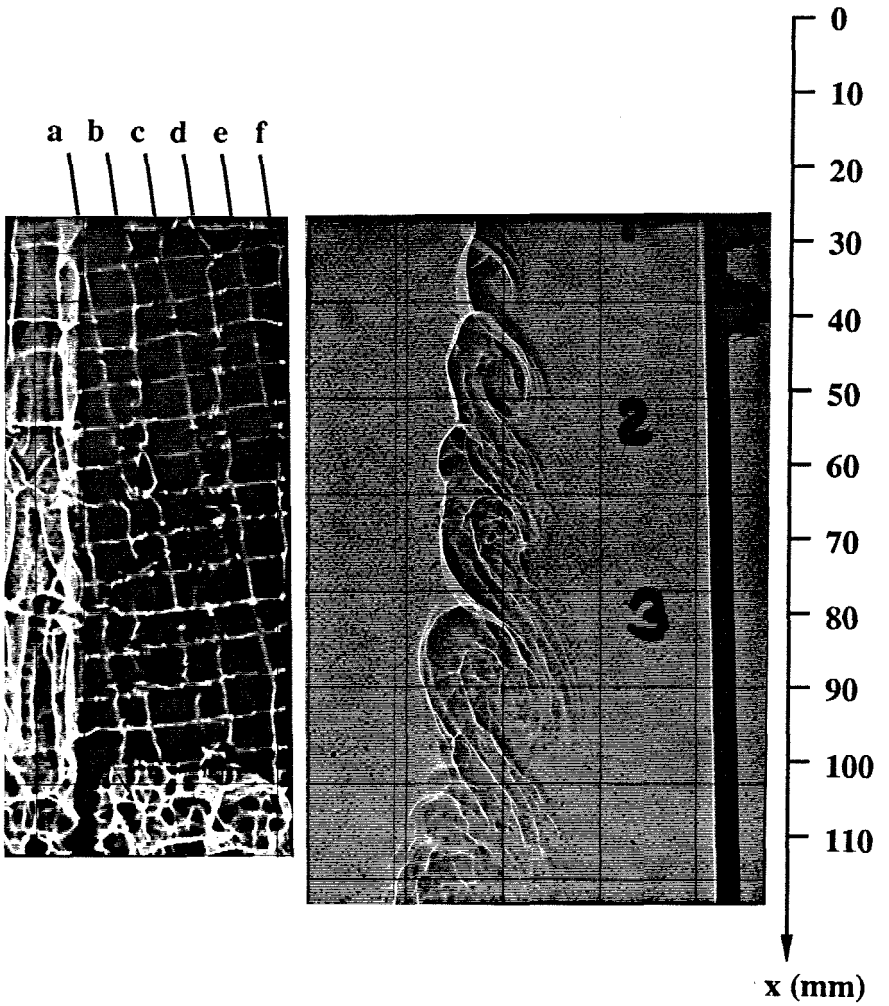

Figure 5.6–Light Sheets ($p = 4\text{bar}$, $u_2 = 1.9\text{m/s}$, $u_1 = 5.0\text{m/s}$, $L = 559\text{mm}$).

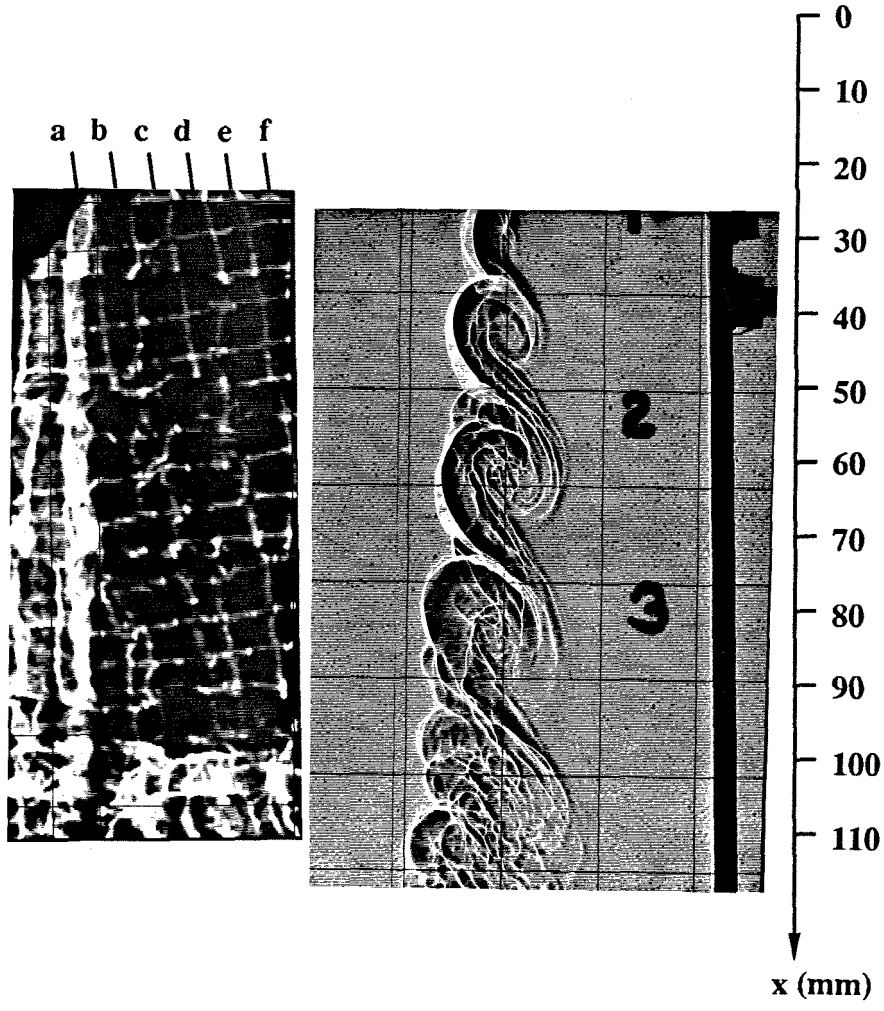

Figure 5.7–Light Sheets ($p = 4\text{bar}$, $u_2 = 1.9\text{m/s}$, $u_1 = 5.0\text{m/s}$, $L = 1118\text{mm}$).

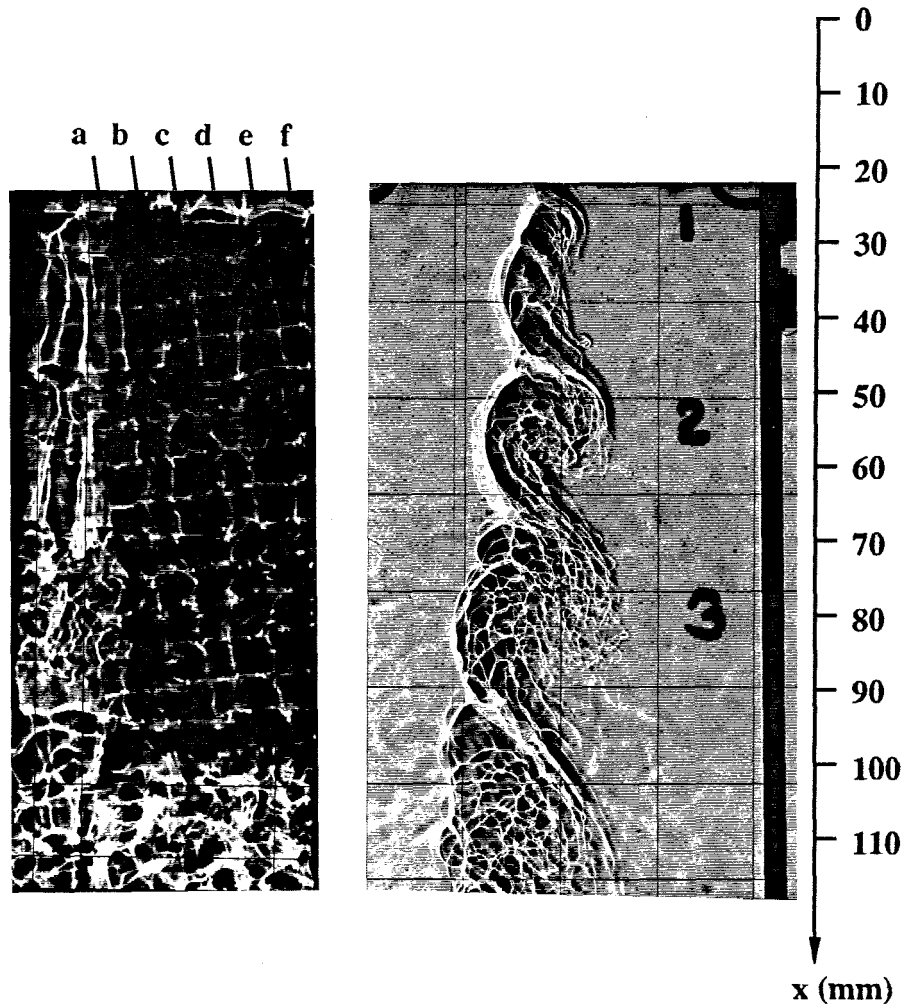

Figure 5.8–Light Sheets ($p = 6\text{bar}$, $u_2 = 1.9\text{m/s}$, $u_1 = 5.0\text{m/s}$, $L = 559\text{mm}$).

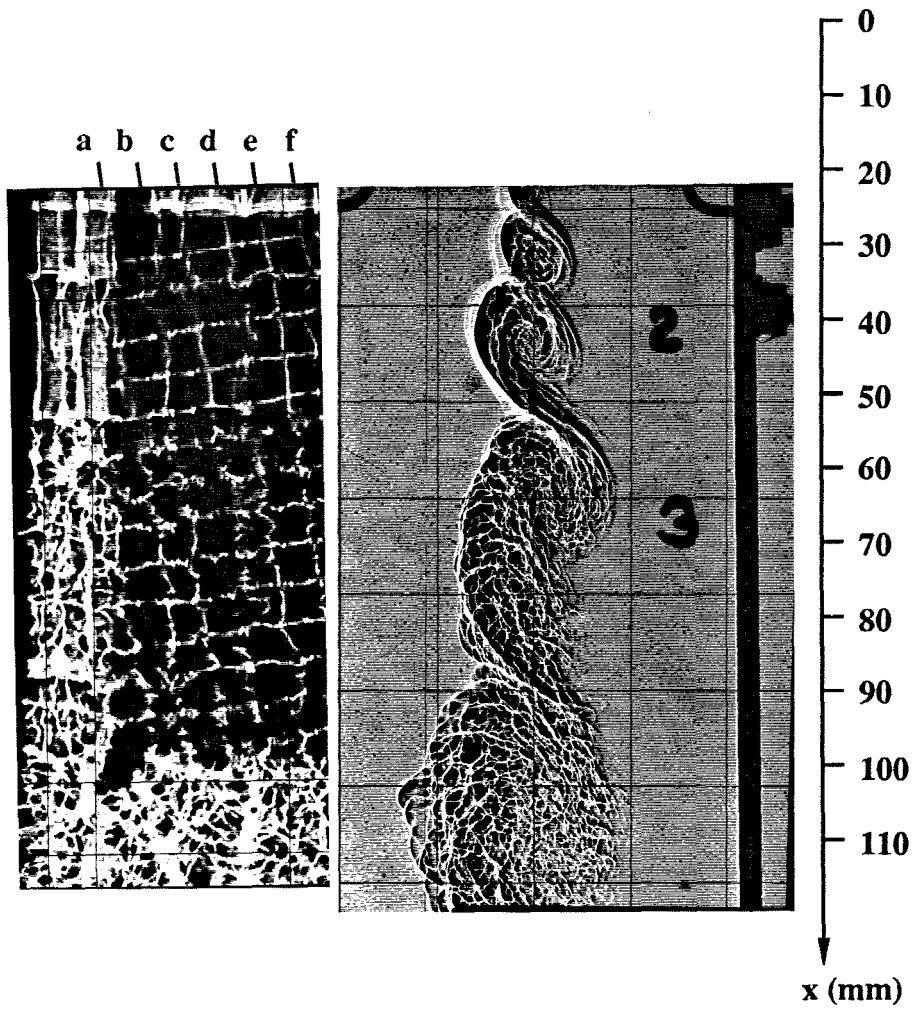

Figure 5.9–Light Sheets ($p = 4$bar, $u_2 = 3.8$m/s, $u_1 = 10.0$m/s, $L = 559$mm).

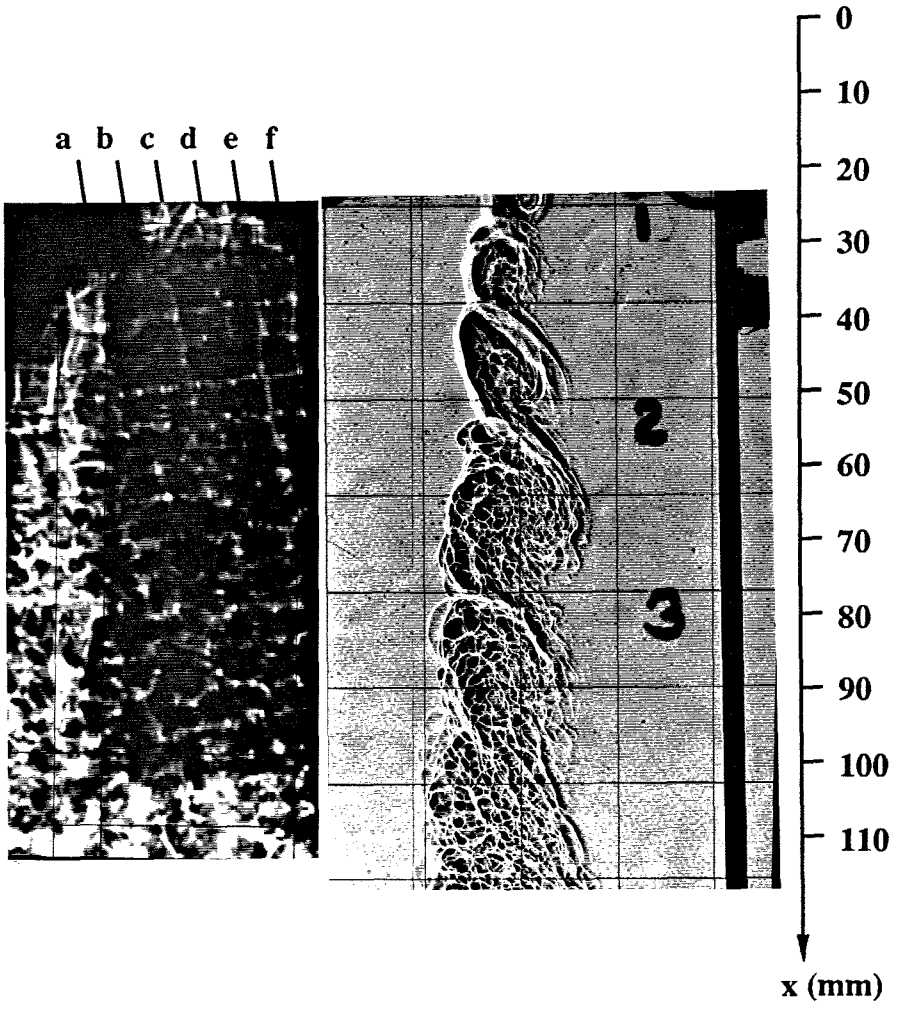

Figure 5.10–Light Sheets ($p = 4$bar, $u_2 = 3.8$m/s, $u_1 = 10.0$m/s, $L = 1118$mm).

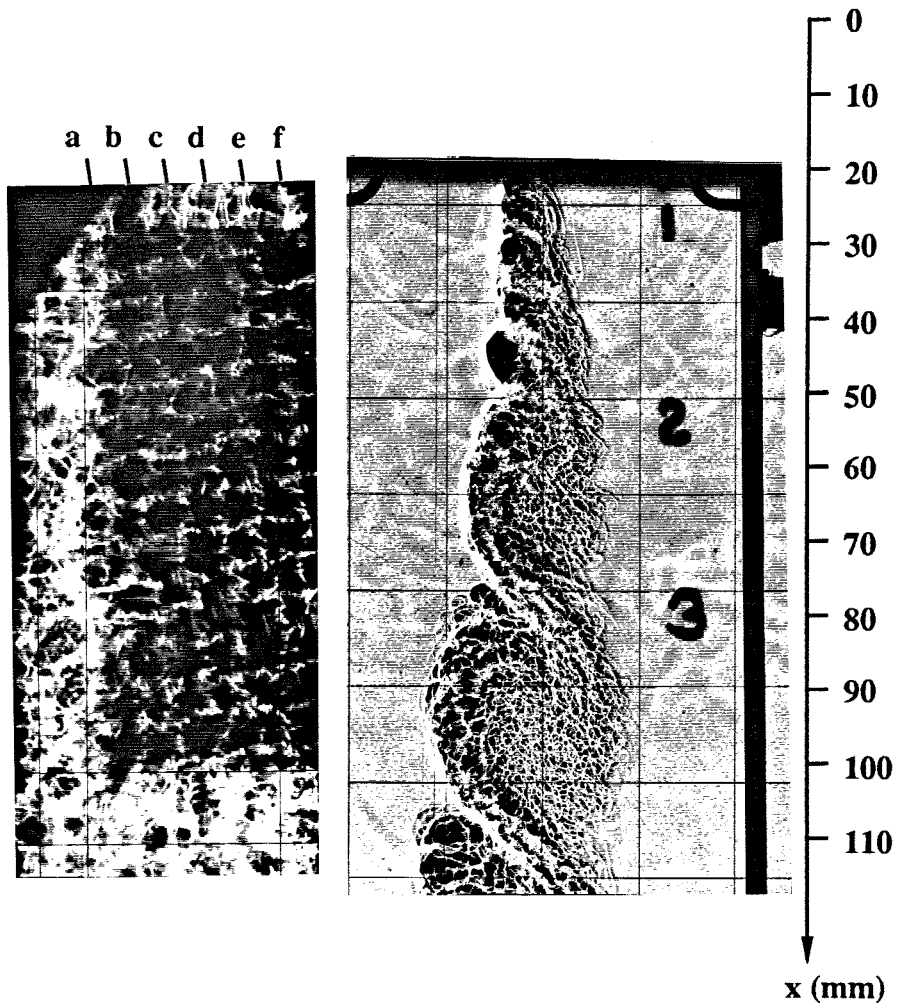

Figure 5.11–Light Sheets ($p = 6\text{bar}$, $u_2 = 3.8\text{m/s}$, $u_1 = 10.0\text{m/s}$, $L = 559\text{mm}$).

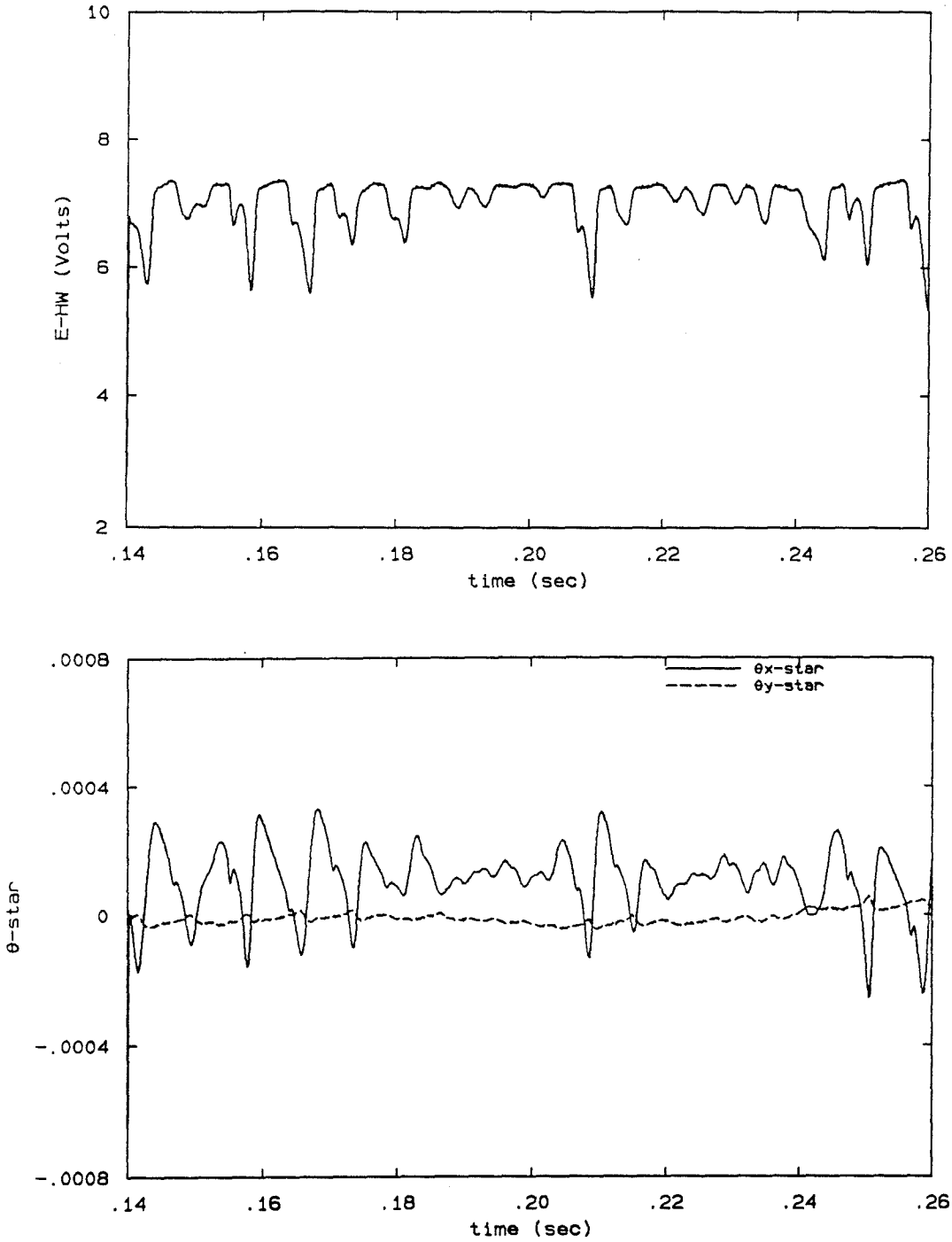

Figure 6.1–Hot-Wire and Beam Deflection Signals.

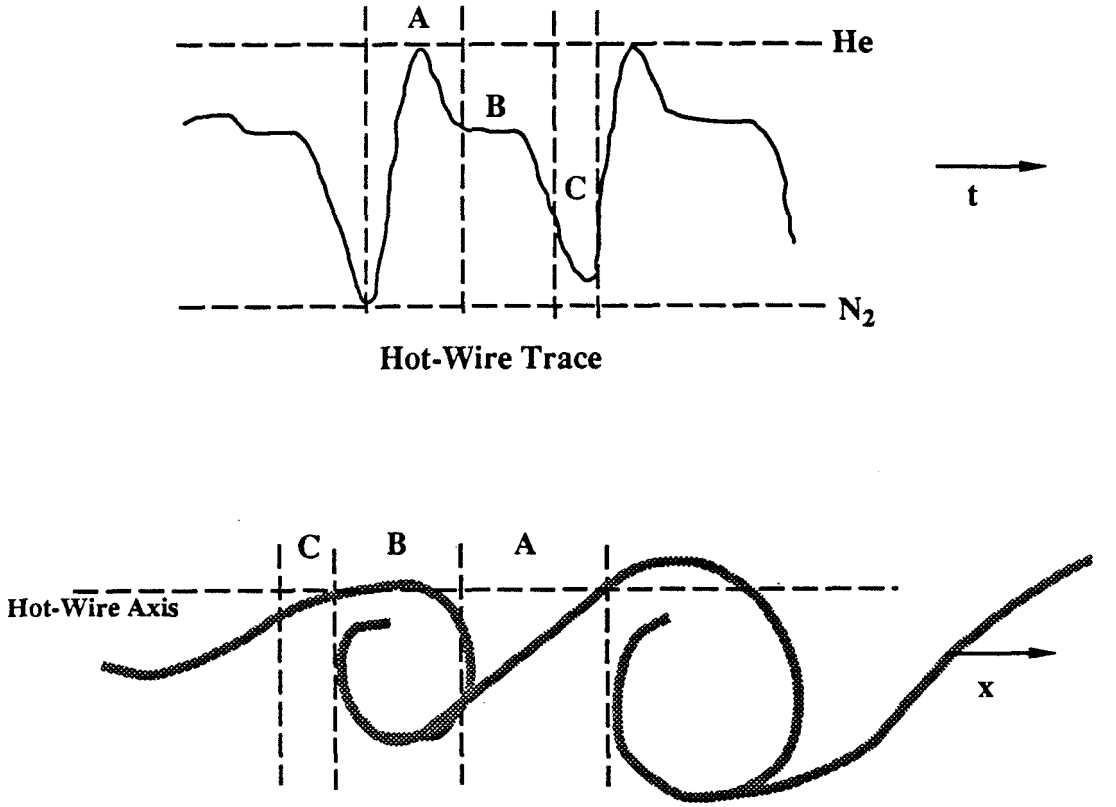

Figure 6.2–Relationship between E_{HW} and Spanwise Coherent Structures.

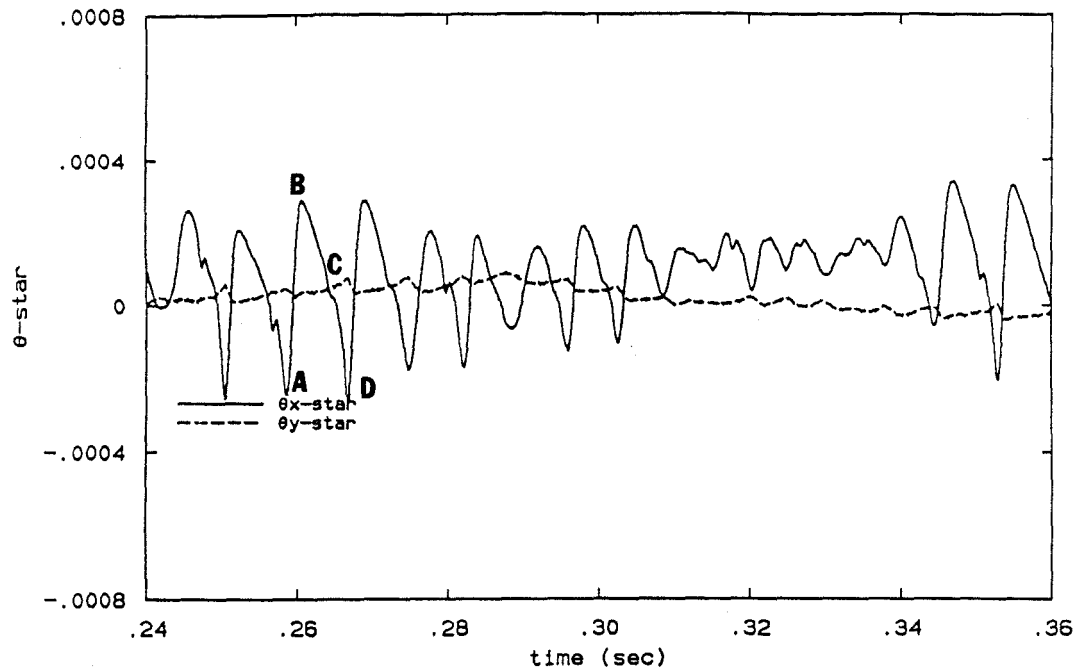

Figure 6.3–θ^* vs. $t(p = 2\text{bar}, u_2 = 1.9\text{m/s}, u_1 = 5.0\text{m/s}, x = 45\text{mm})$.

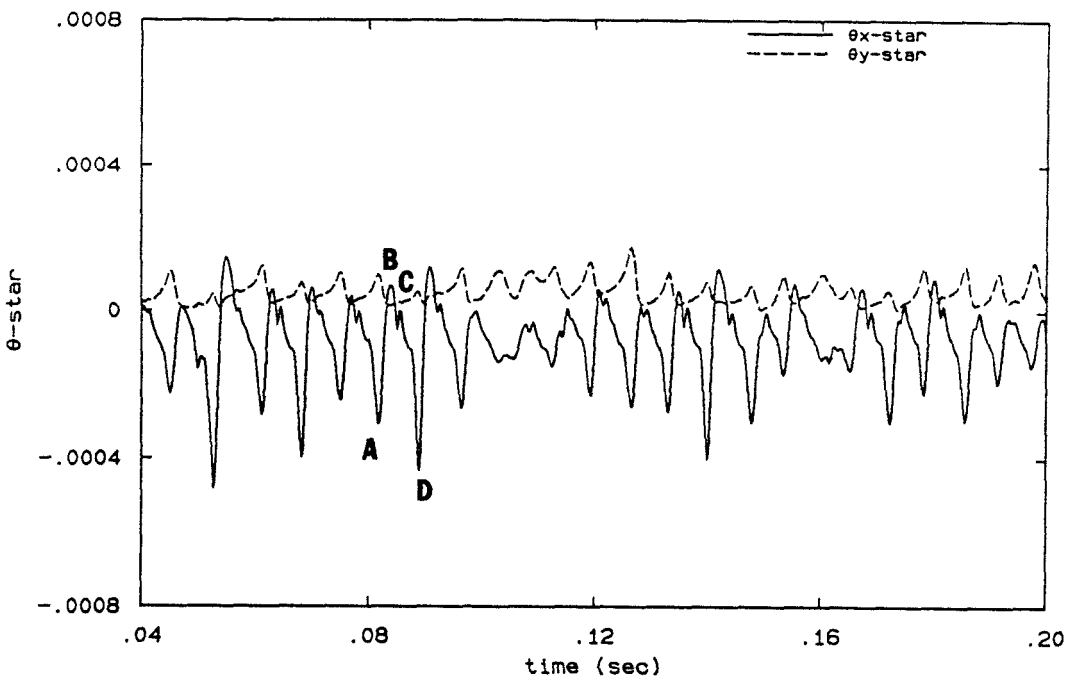

Figure 6.4–θ^* vs. $t(p = 4\text{bar}, u_2 = 0.95\text{m/s}, u_1 = 2.5\text{m/s}, x = 45\text{mm})$.

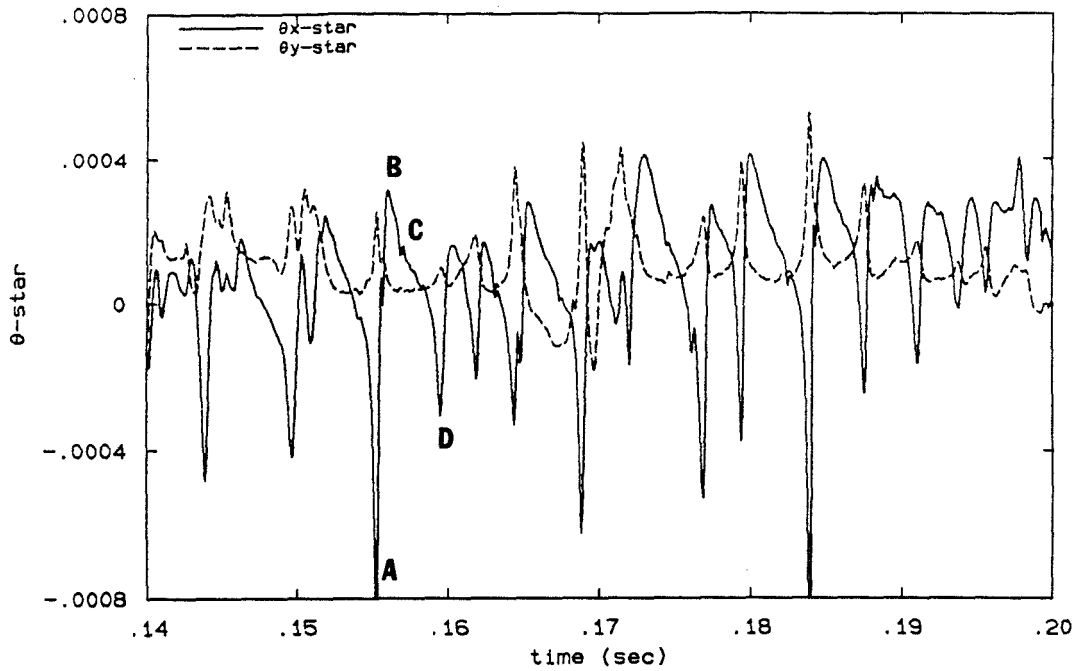

Figure 6.5–θ^* vs. $t(p = 2\text{bar}, u_2 = 3.8\text{m/s}, u_1 = 10.0\text{m/s}, x = 45\text{mm})$.

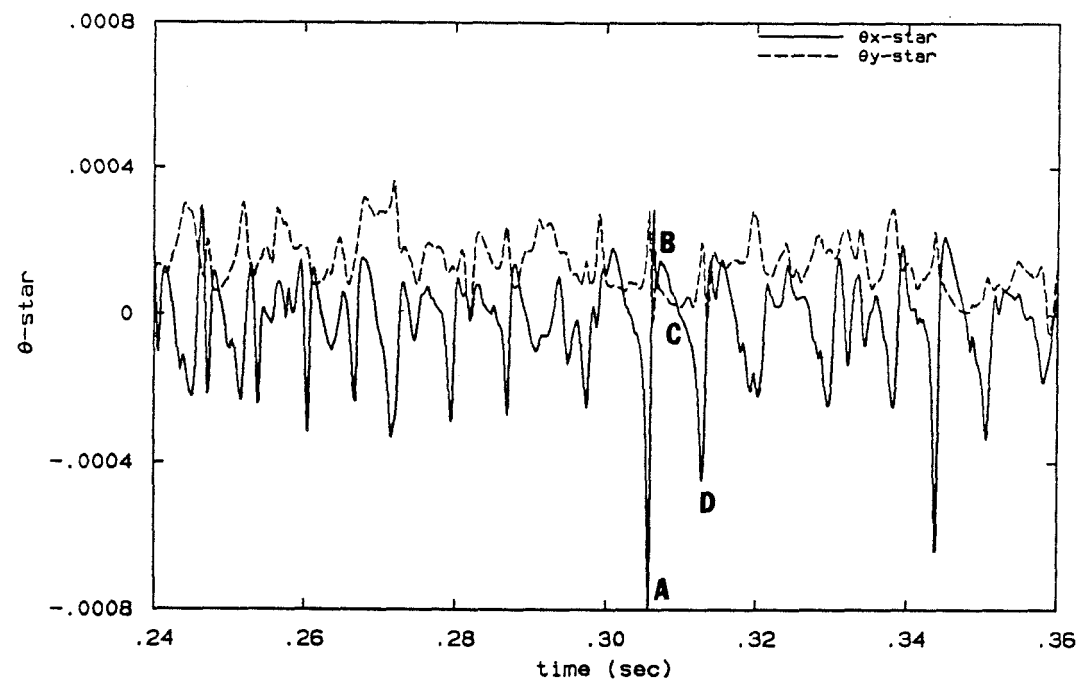

Figure 6.6–θ^* vs. $t(p = 4\text{bar}, u_2 = 1.9\text{m/s}, u_1 = 5.0\text{m/s}, x = 45\text{mm})$.

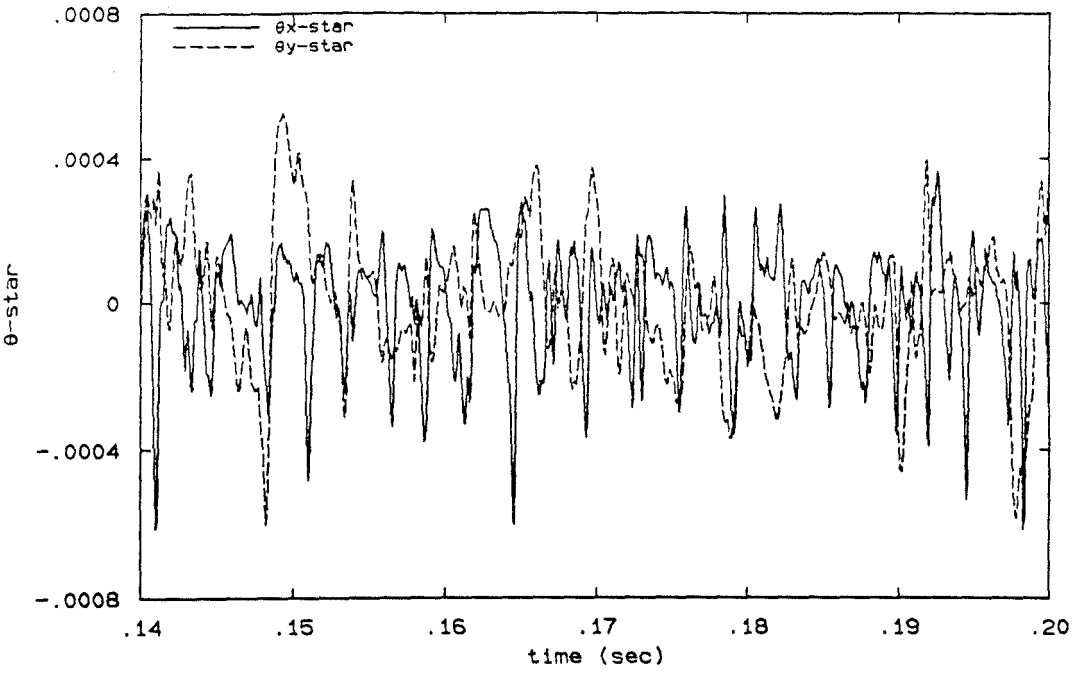

Figure 6.7–θ^* vs. $t(p = 4\text{bar}, u_2 = 3.8\text{m/s}, u_1 = 10.0\text{m/s}, x = 45\text{mm})$.

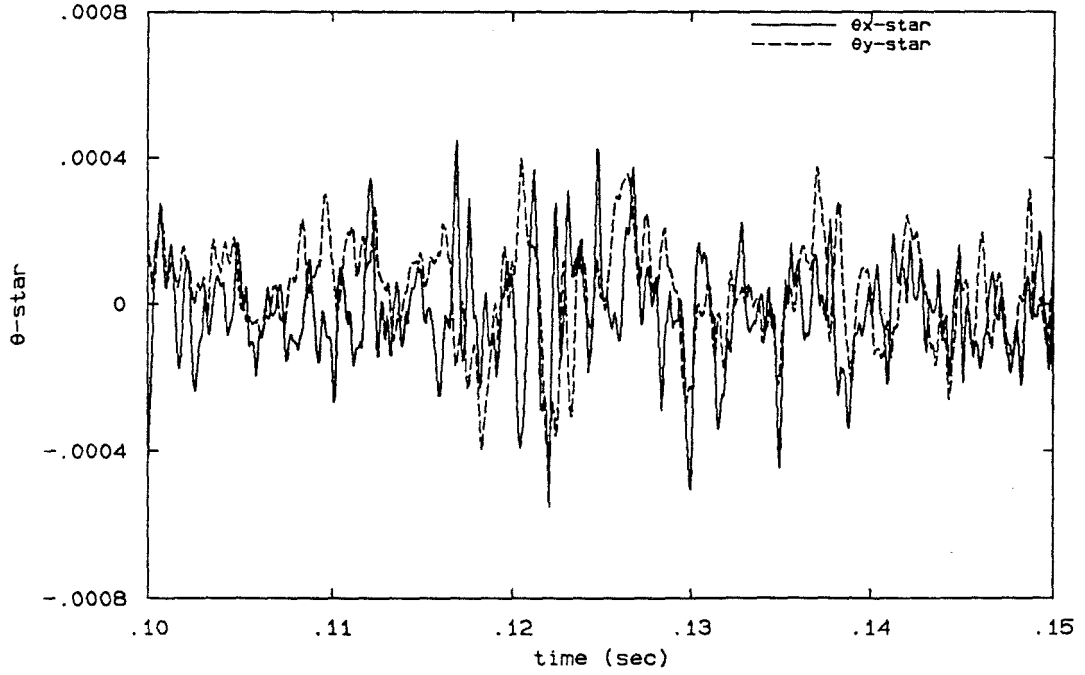

Figure 6.8–θ^* vs. $t(p = 6\text{bar}, u_2 = 3.8\text{m/s}, u_1 = 10.0\text{m/s}, x = 134\text{mm})$.

a)

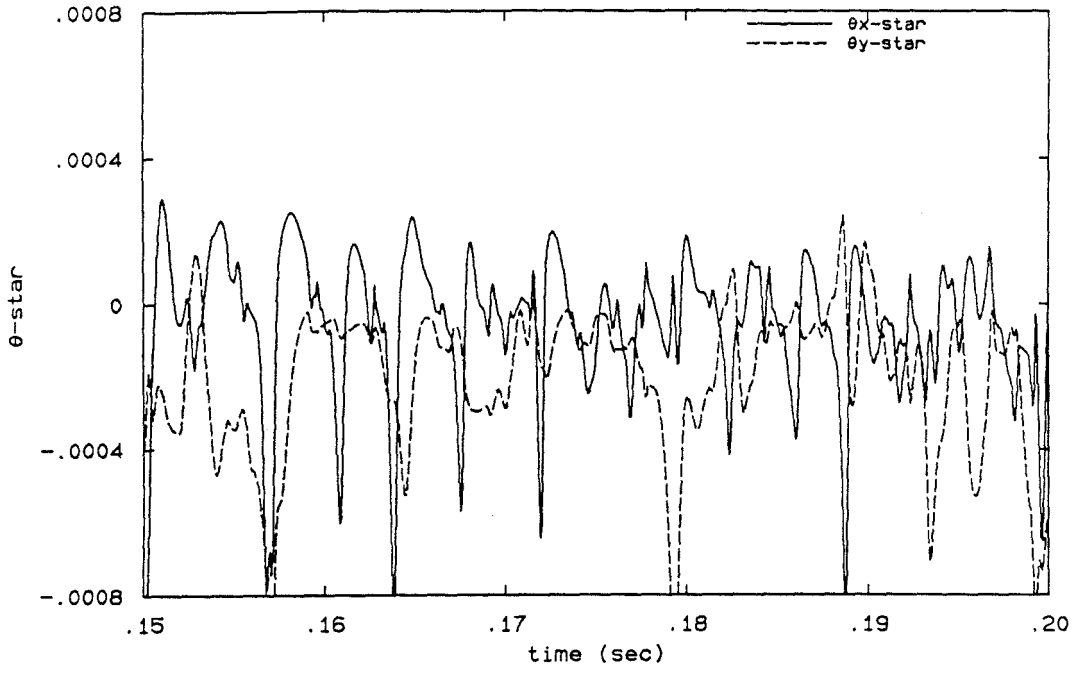

b)

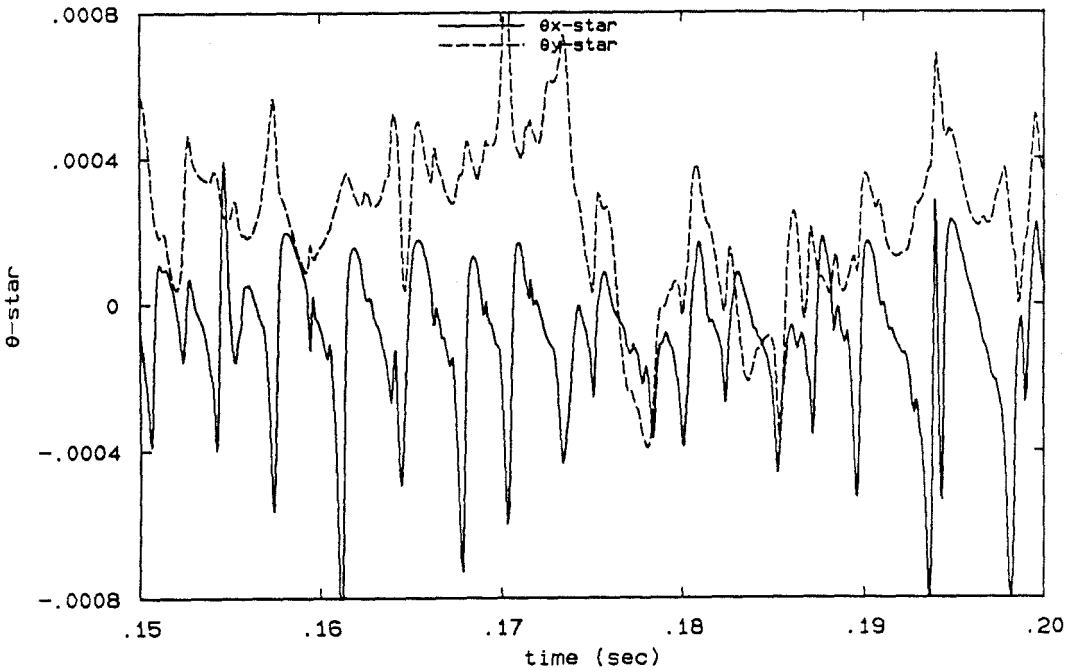

Caption on page 96.

c)

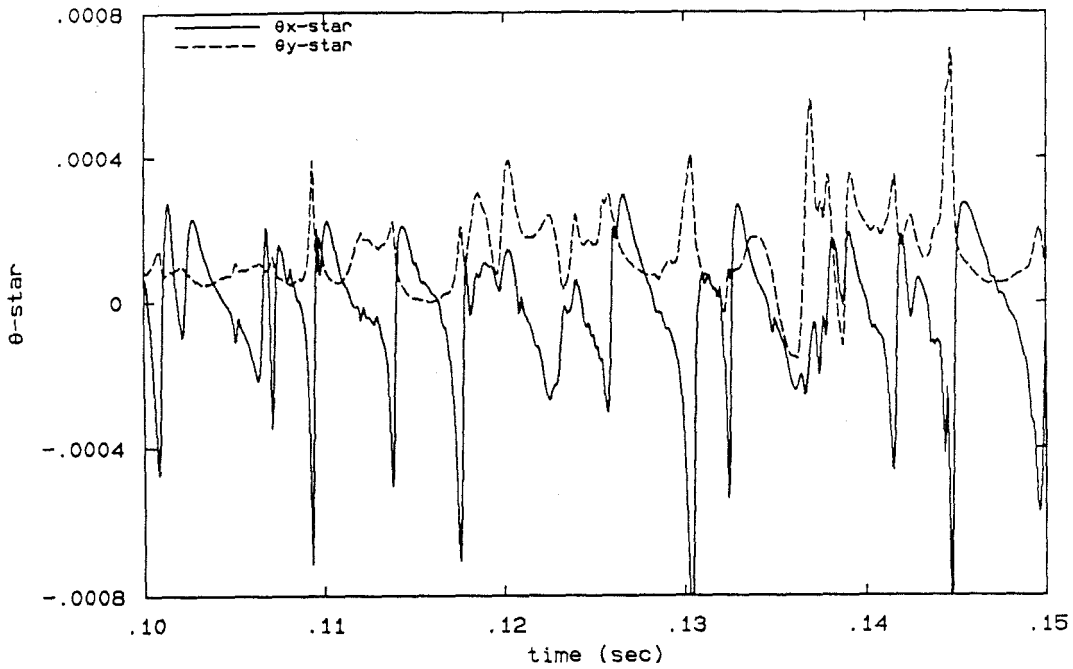

d)

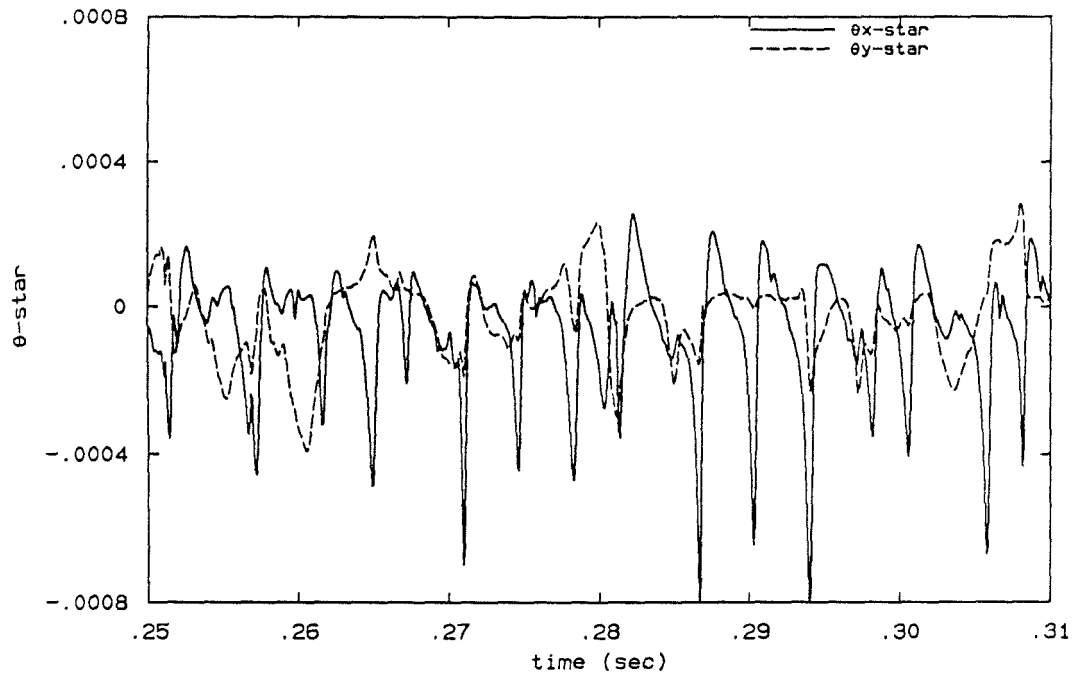

Caption on page 96.

e)

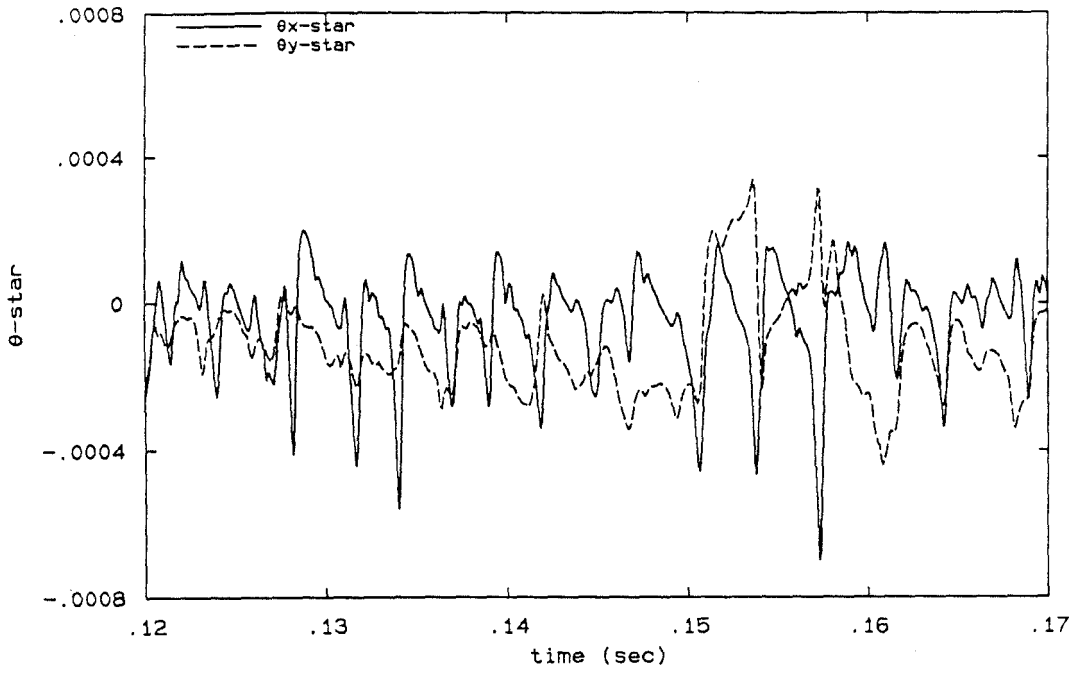

f)

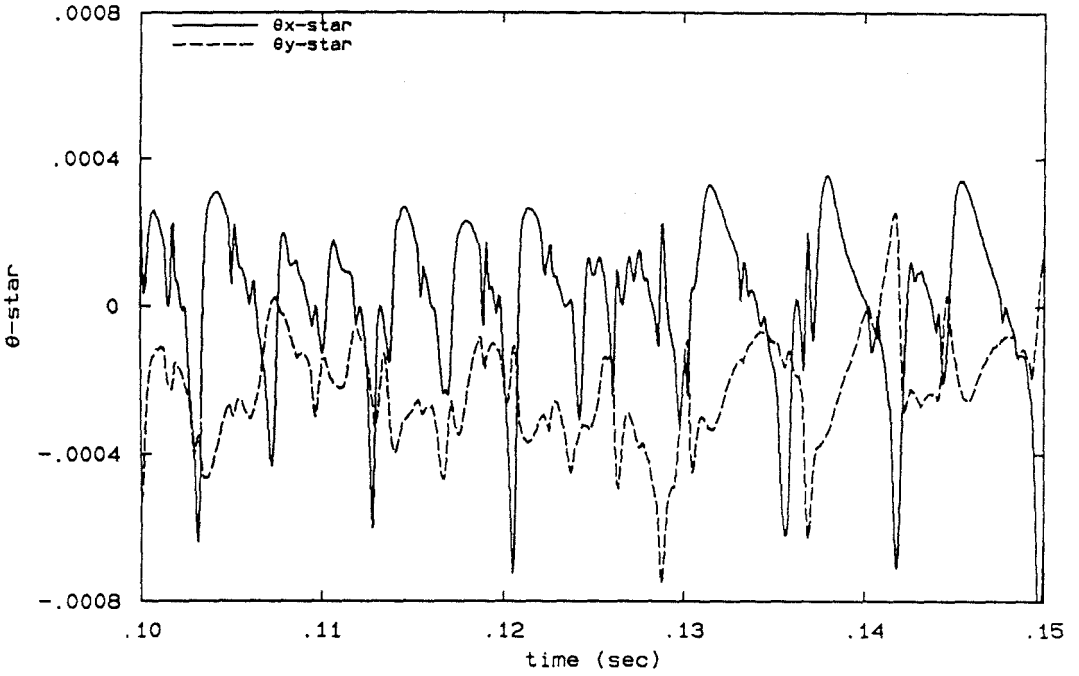

Figure 6.9–Deflection Angle Spanwise Dependence ($p = 2$ bar, $u_2 = 3.8$m/s,$u_1 = 10.0$m/s, $x = 45$mm) a) $y = 0$mm b) $y = 2$mm c) $y = 4$mm d) $y = 6$mm e) $y = 8$mm f) $y = 10$mm.

a)

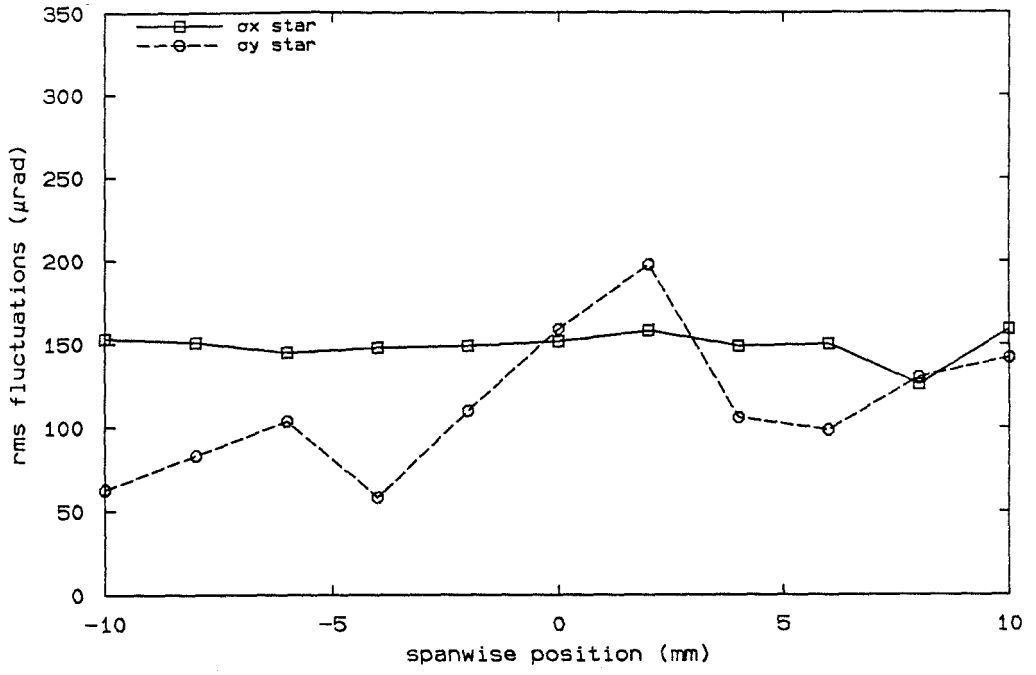

b)

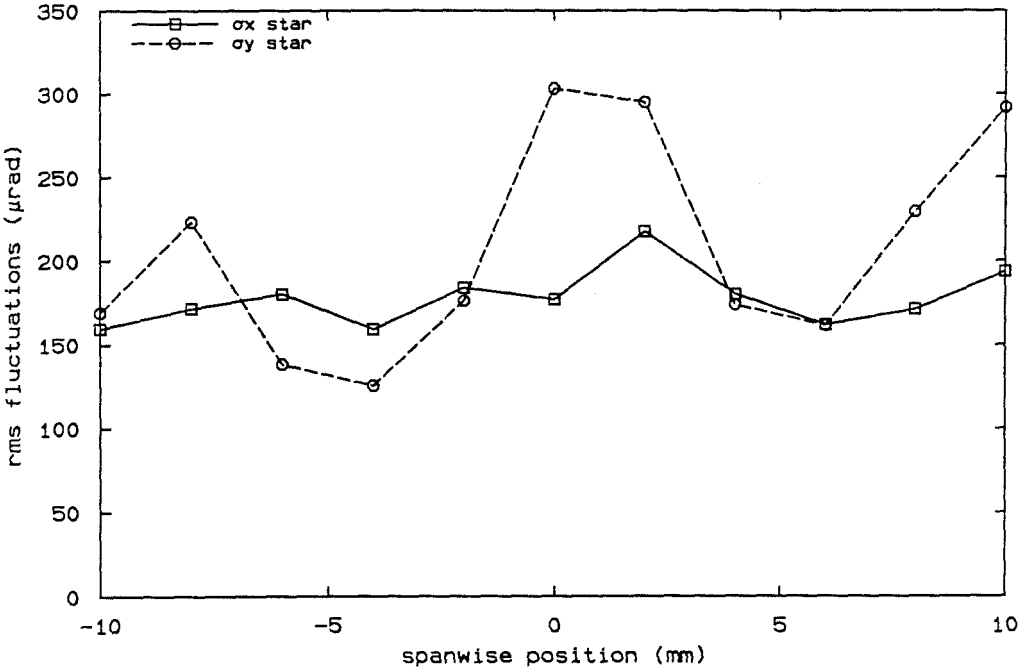

Caption on page 98.

c)

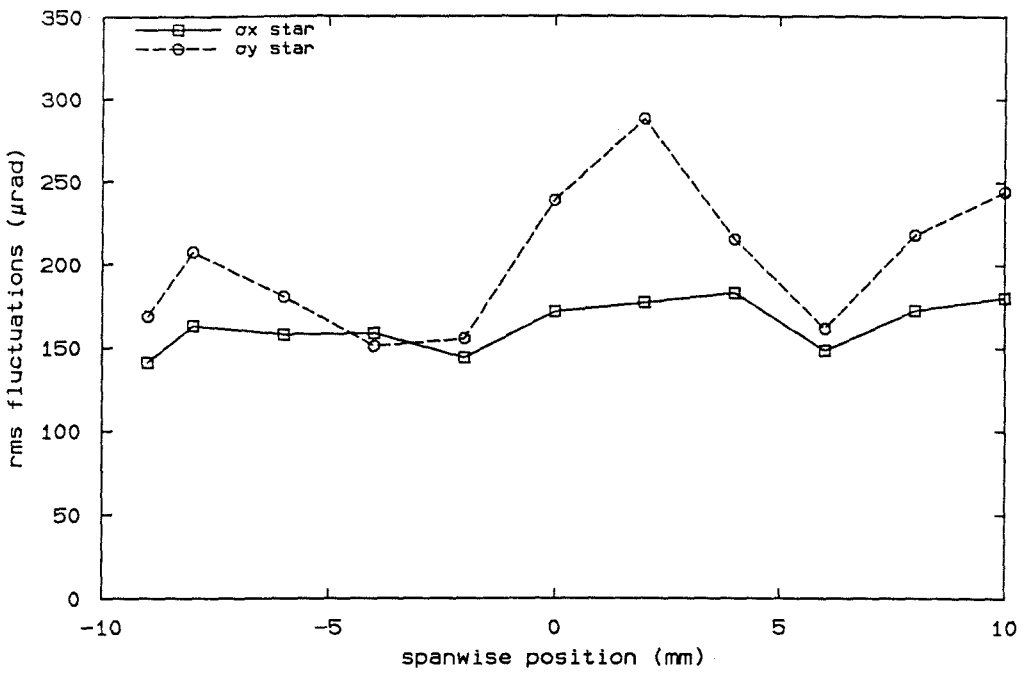

Figure 6.10–RMS Fluctuations vs. Spanwise Position (p = 2 bar, u_2 = 3.8m/s,u_1 = 10.0m/s) a) x = 45mm b) x = 88mm c) x = 113mm.

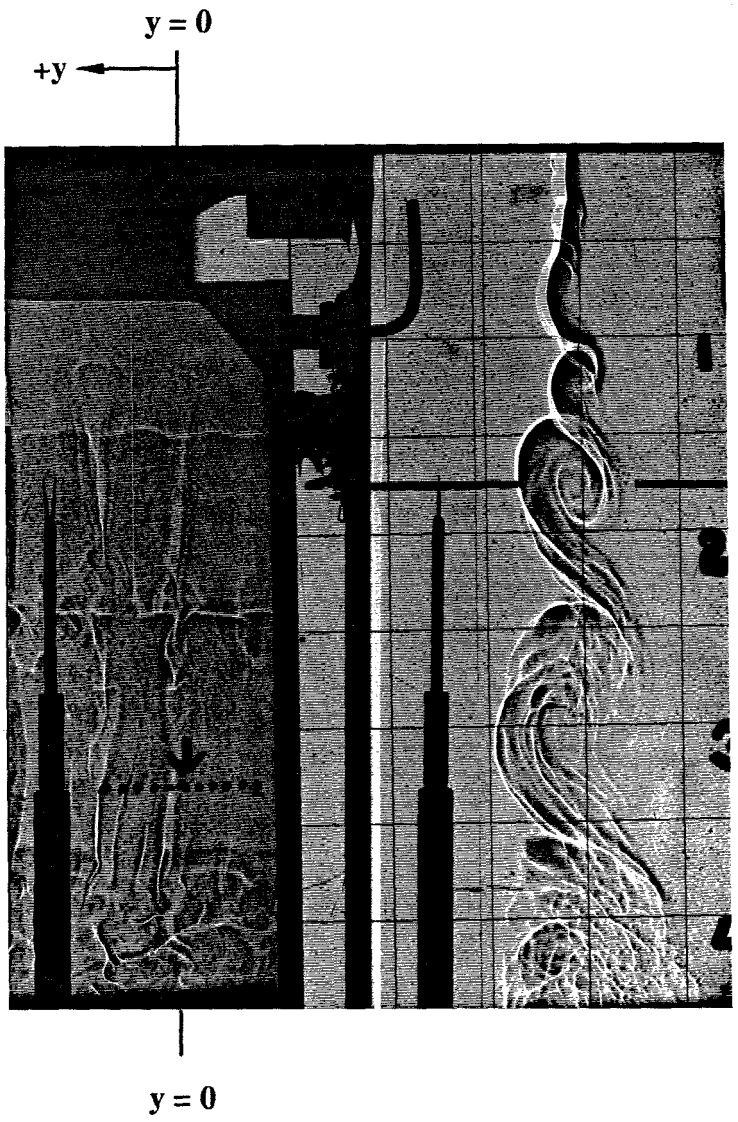

Figure 6.11–Shadowgraph ($p = 2\text{bar}$, $u_2 = 3.8\text{m/s}$, $u_1 = 10.0\text{m/s}$).

a)

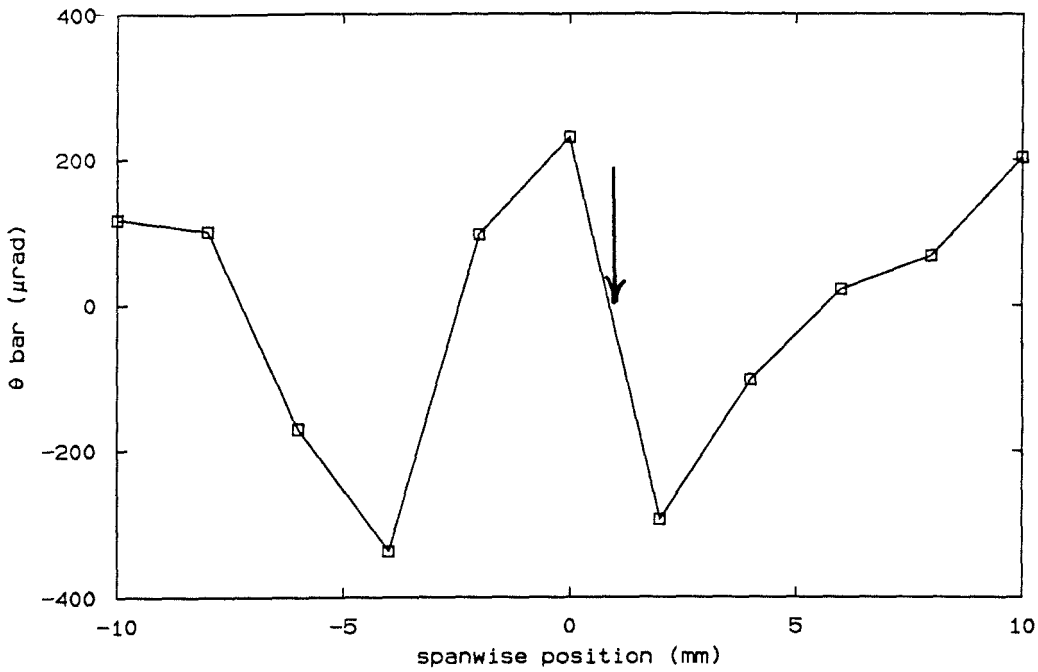

b)

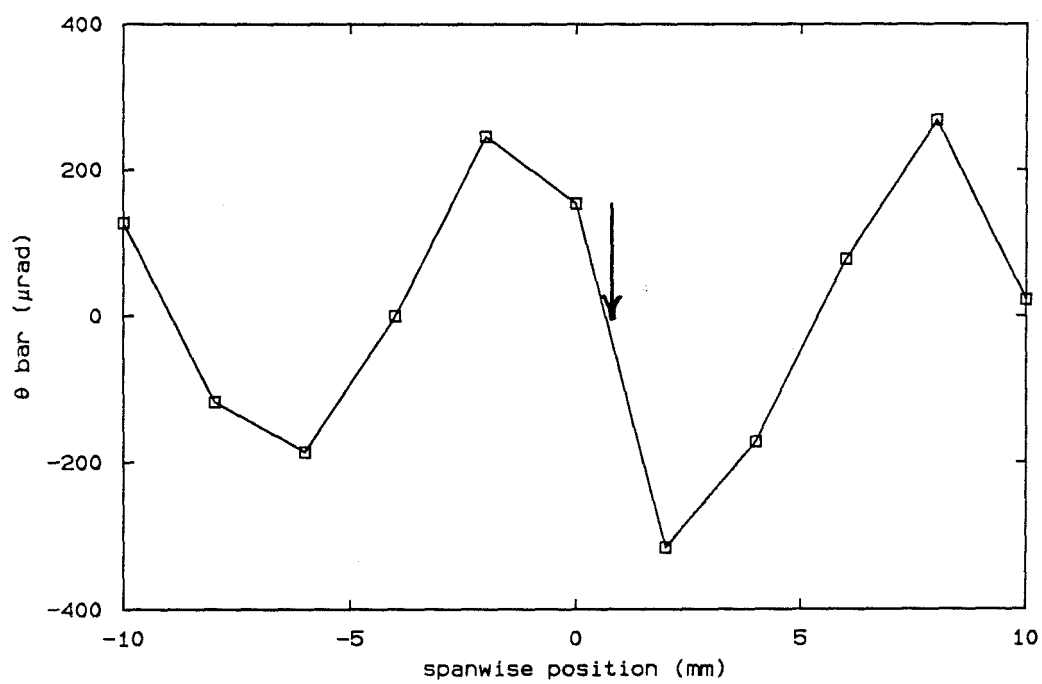

Caption on page 101.

c)

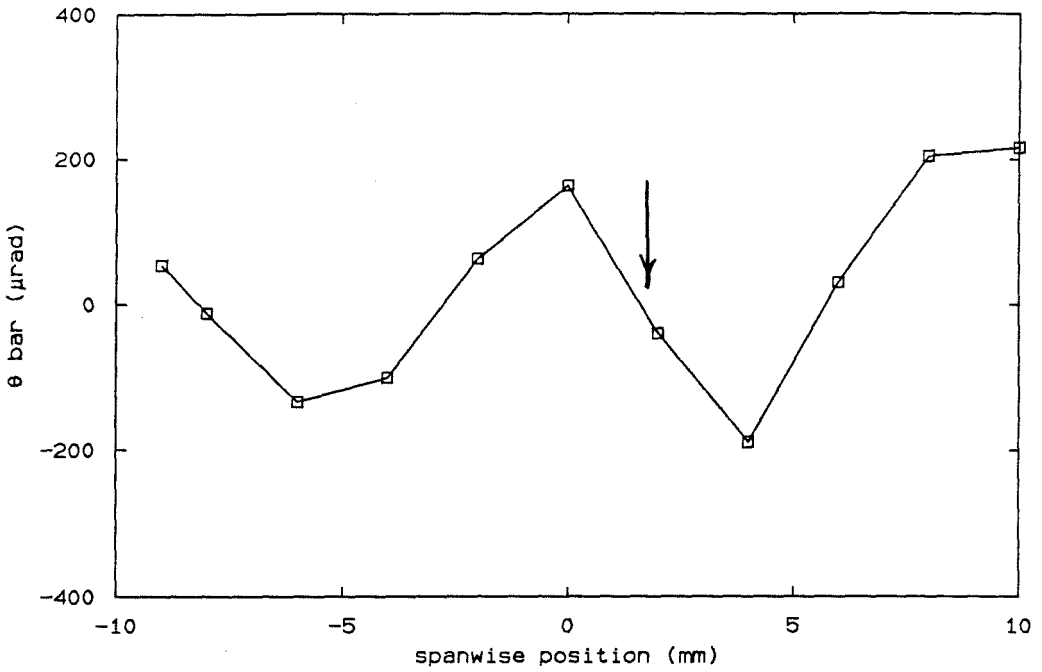

Figure 6.12–Mean Spanwise Deflection (p = 2 bar, u_2 = 3.8m/s,u_1 = 10.0m/s) a) x = 45mm b) x = 88mm c) x = 113mm.

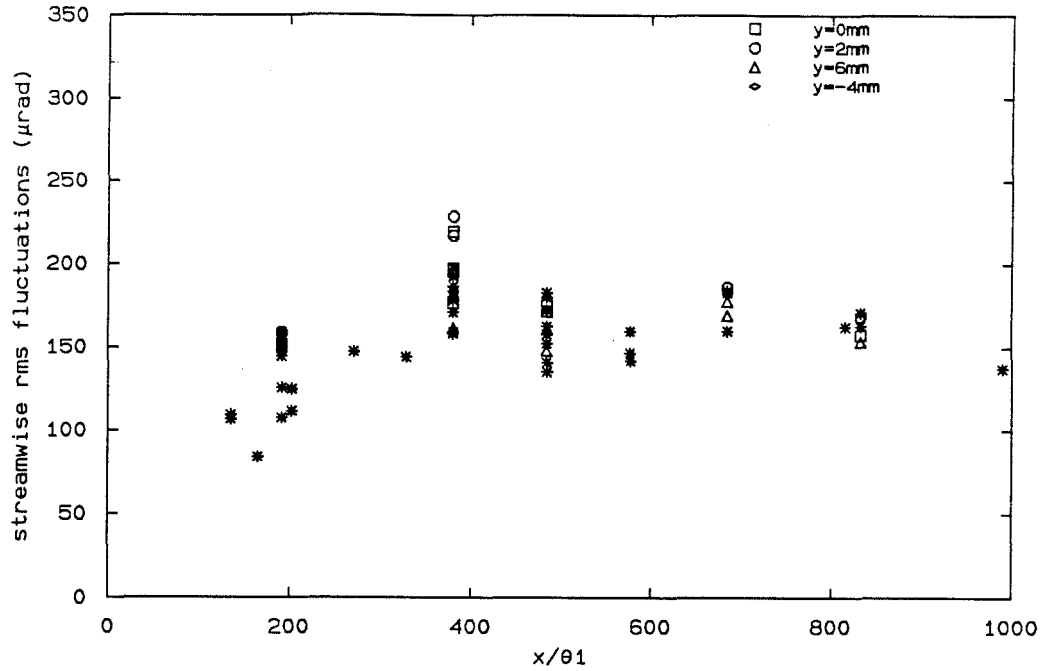

Figure 6.13–Streamwise rms Fluctuations vs x/θ_1 ($*$=other y positions).

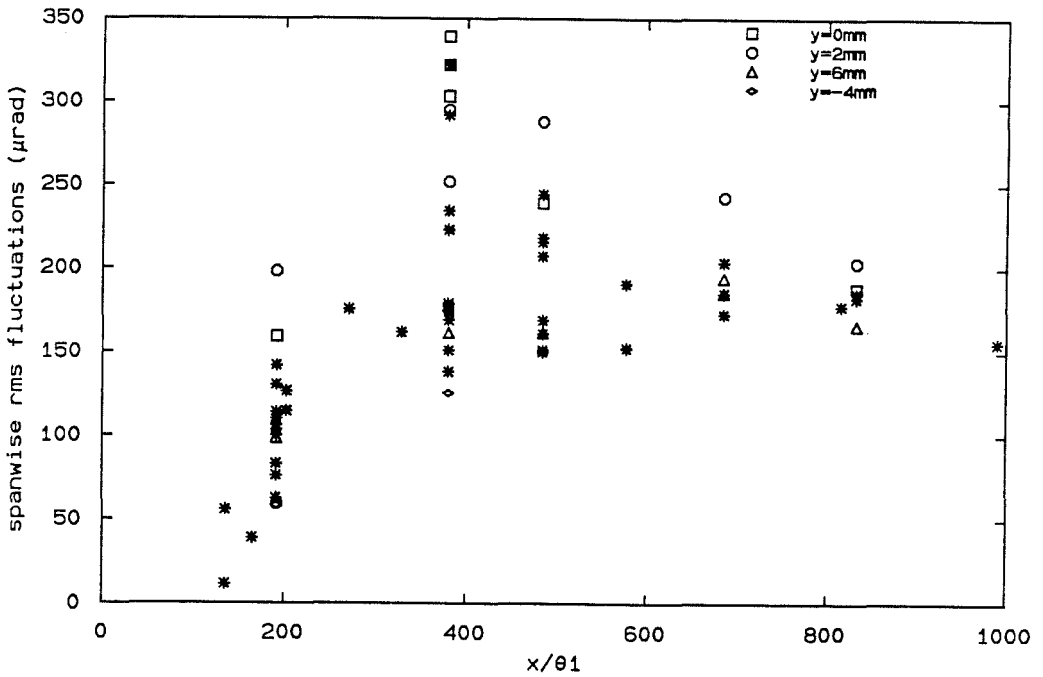

Figure 6.14–Spanwise rms Fluctuations vs x/θ_1 ($*$=other y positions).

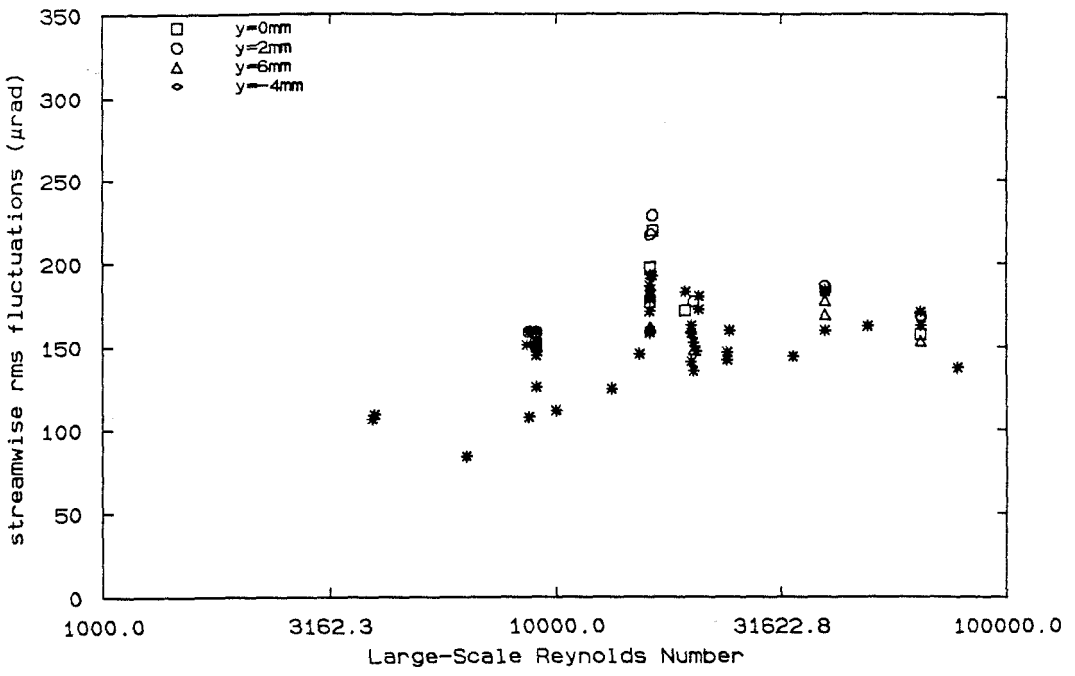

Figure 6.15–Streamwise rms Fluctuations vs Re_δ ($*$=other y positions).

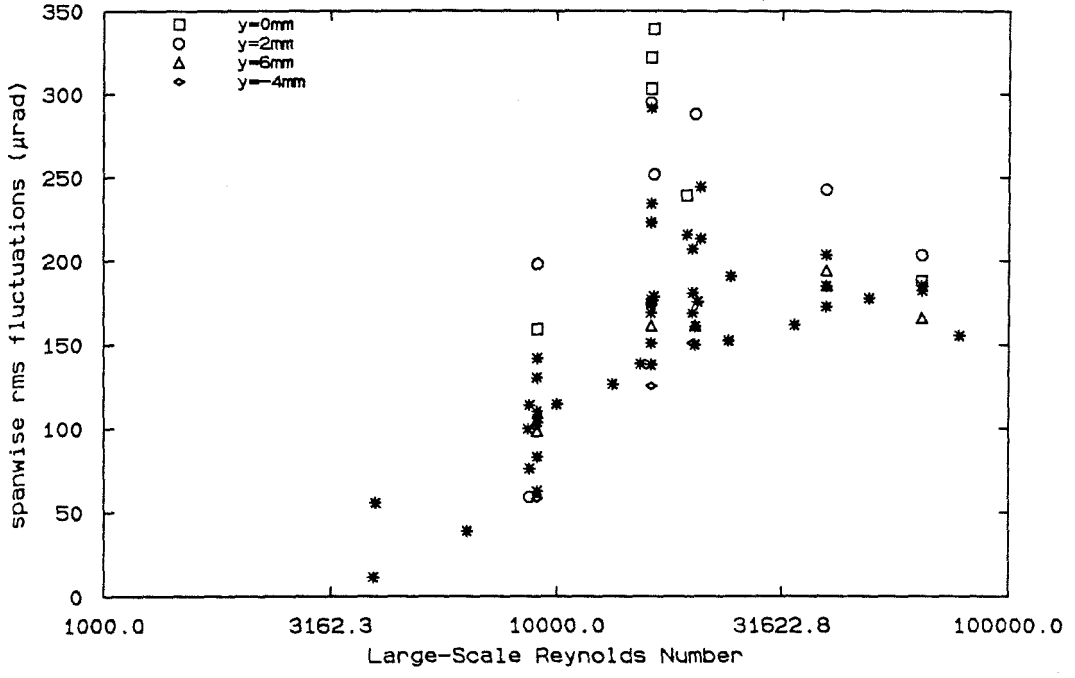

Figure 6.16–Spanwise rms Fluctuations vs Re_δ ($*$=other y positions).

a)

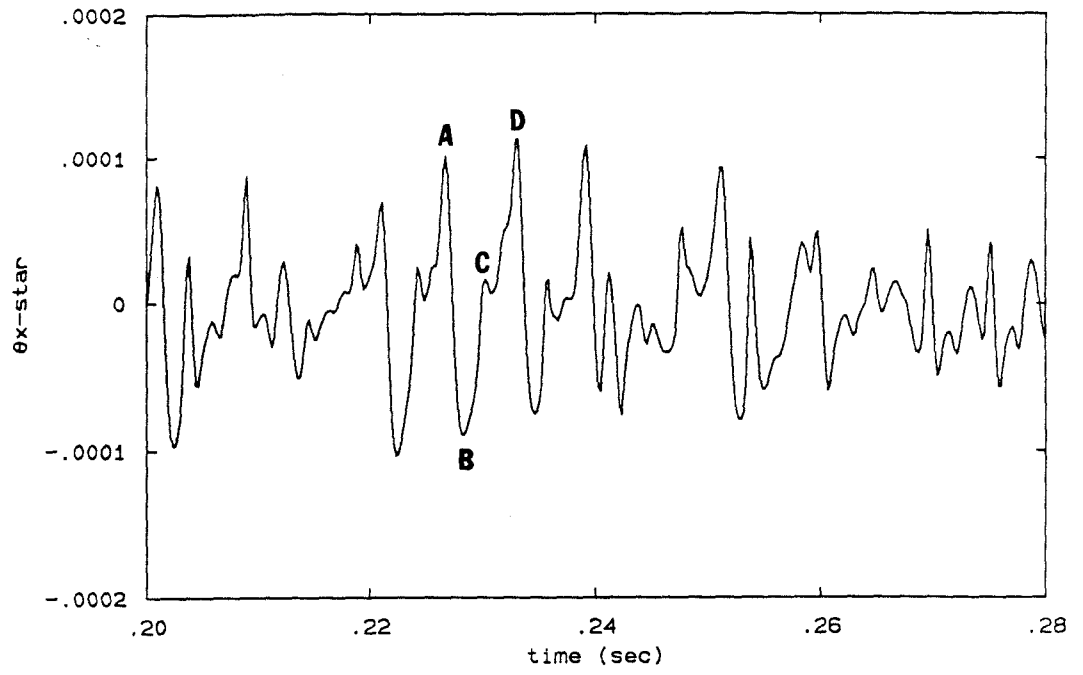

b)

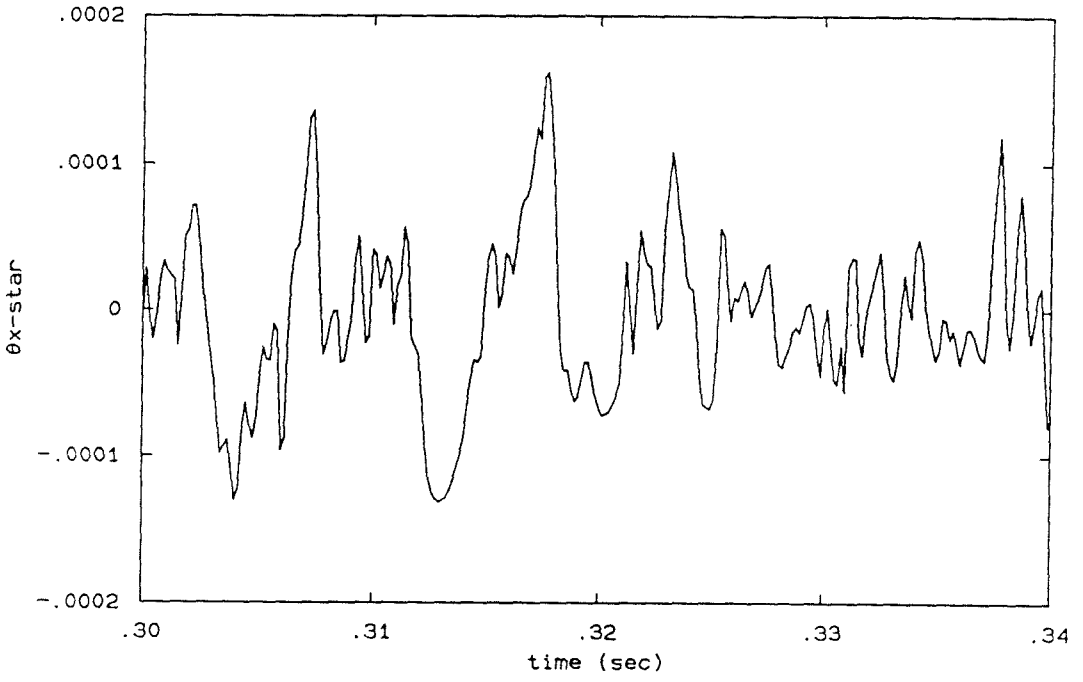

Figure 7.1–Deflection Angle vs Time (N_2/He-Ar,$p = 4$ bar, $x = 29.7$mm) a) $u_2 = 0.9$m/s, $u_1 = 2.5$m/s b) $u_2 = 1.9$m/s, $u_1 = 5.0$m/s.

a)

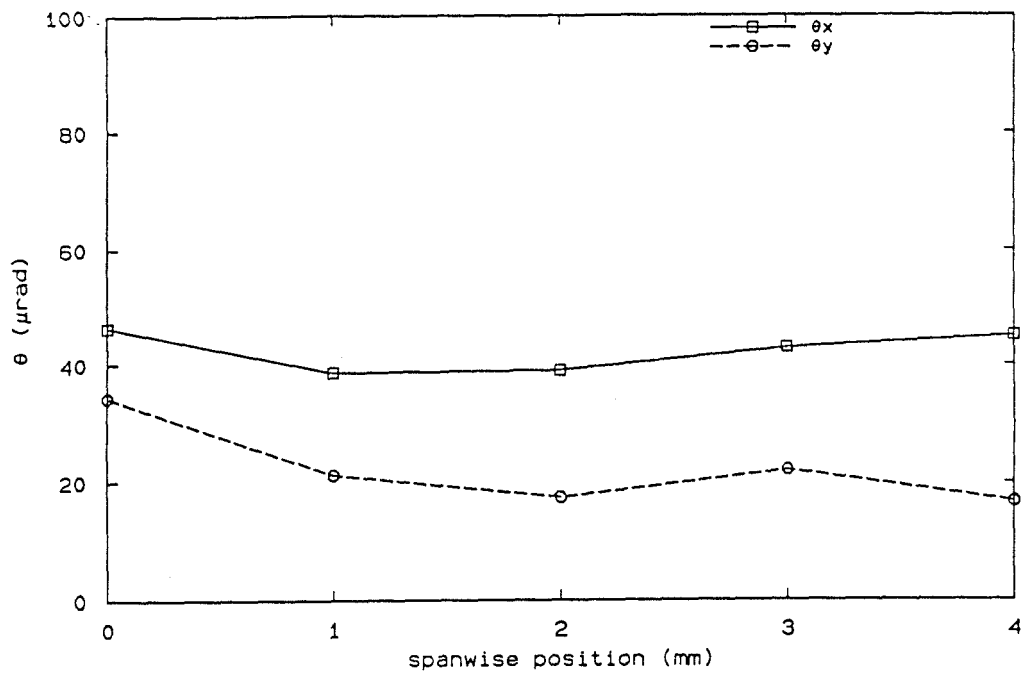

b)

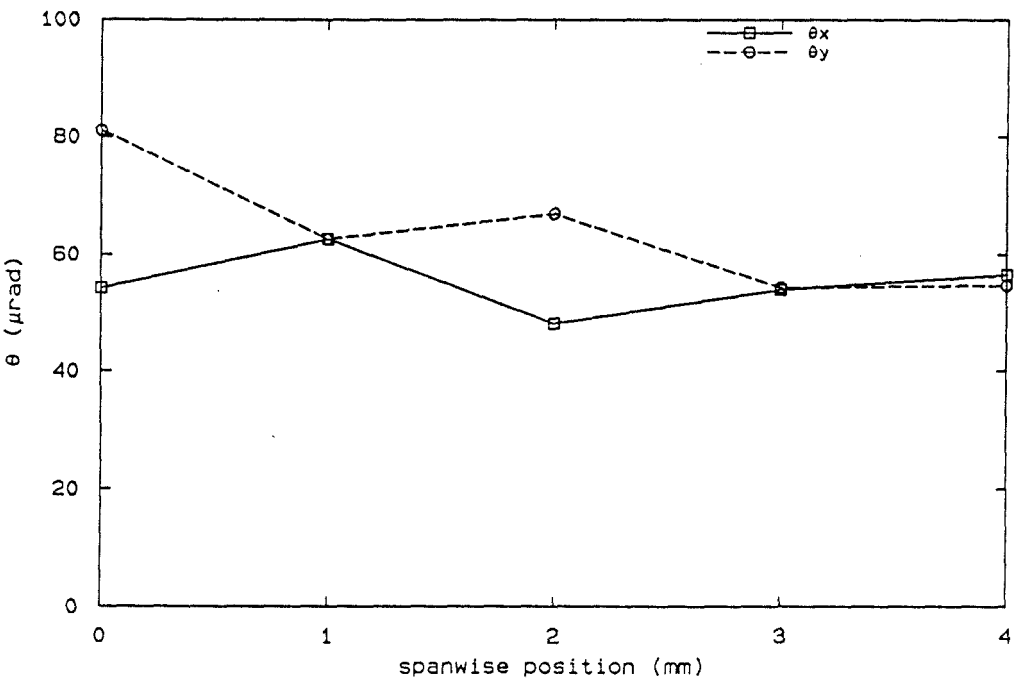

Caption on page 107.

c)

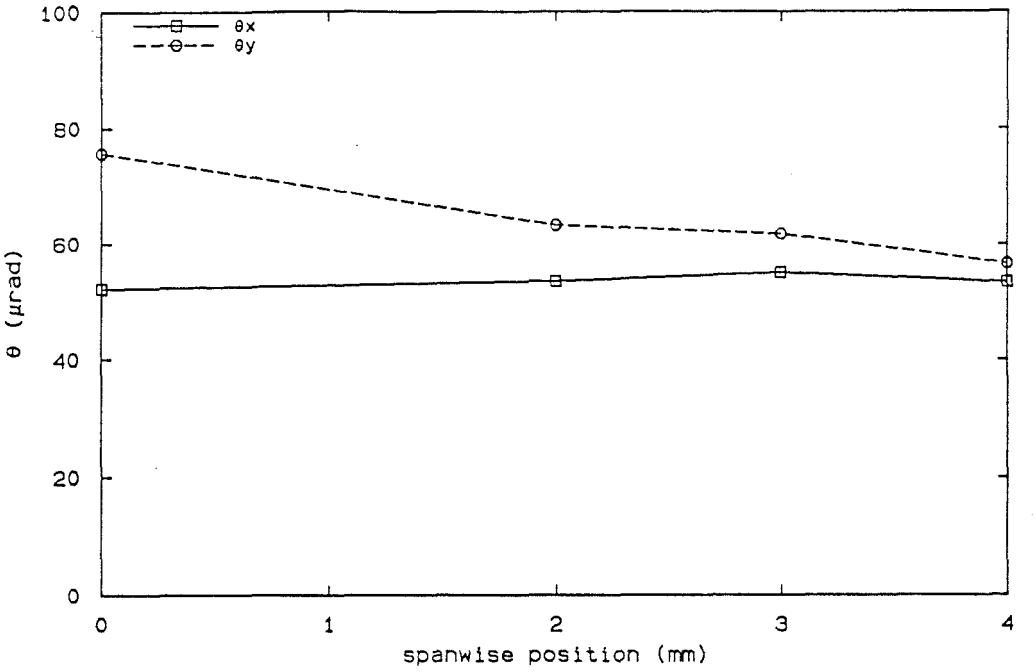

d)

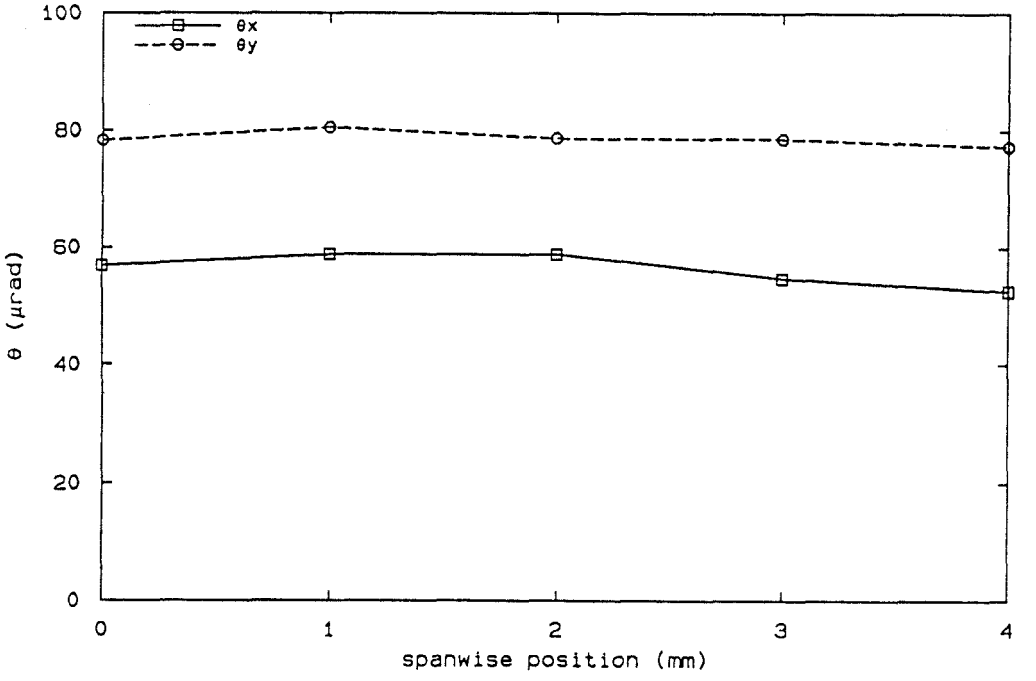

Caption on page 107.

e)

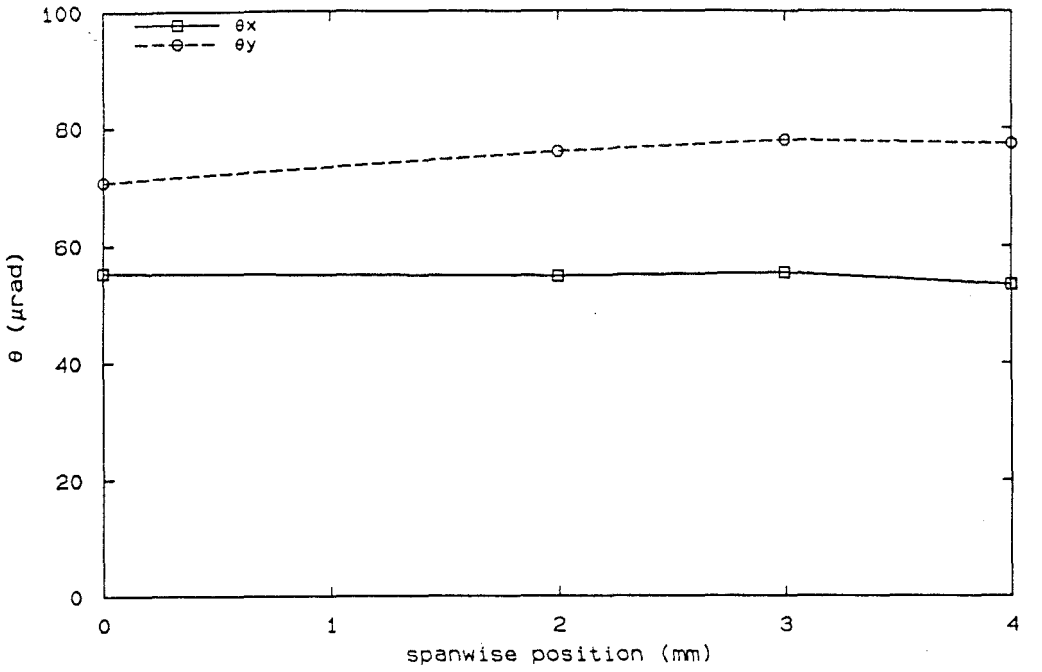

Figure 7.2–RMS Fluctuations vs Spanwise Position ($N_2/He-Ar$) a) $x/\theta_1 =$ 250 b) $x/\theta_1 = 357$ c) $x/\theta_1 = 536$ d) $x/\theta_1 = 1064$ e) $x/\theta_1 = 1355$.

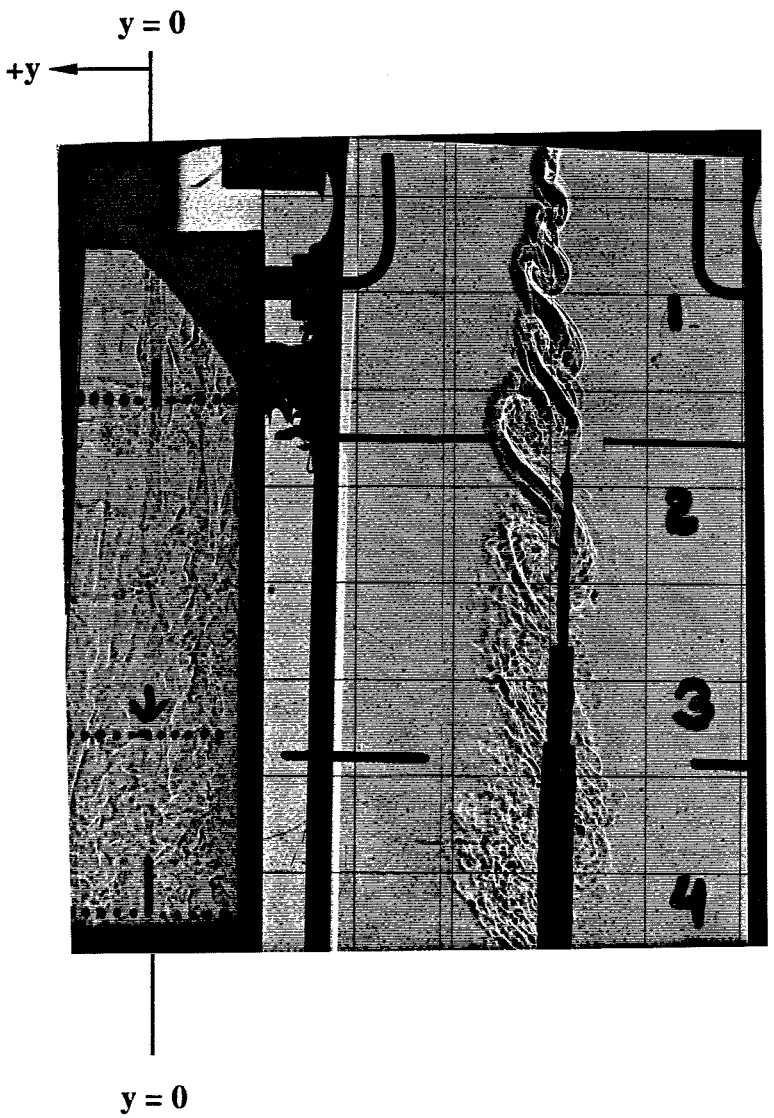

Figure 7.3–Shadowgraph of $N_2/He - Ar$ Turbulent Mixing Layer ($p = 4$ bar, $u_2 = 1.9$ m/s, $u_1 = 5.0$ m/s).

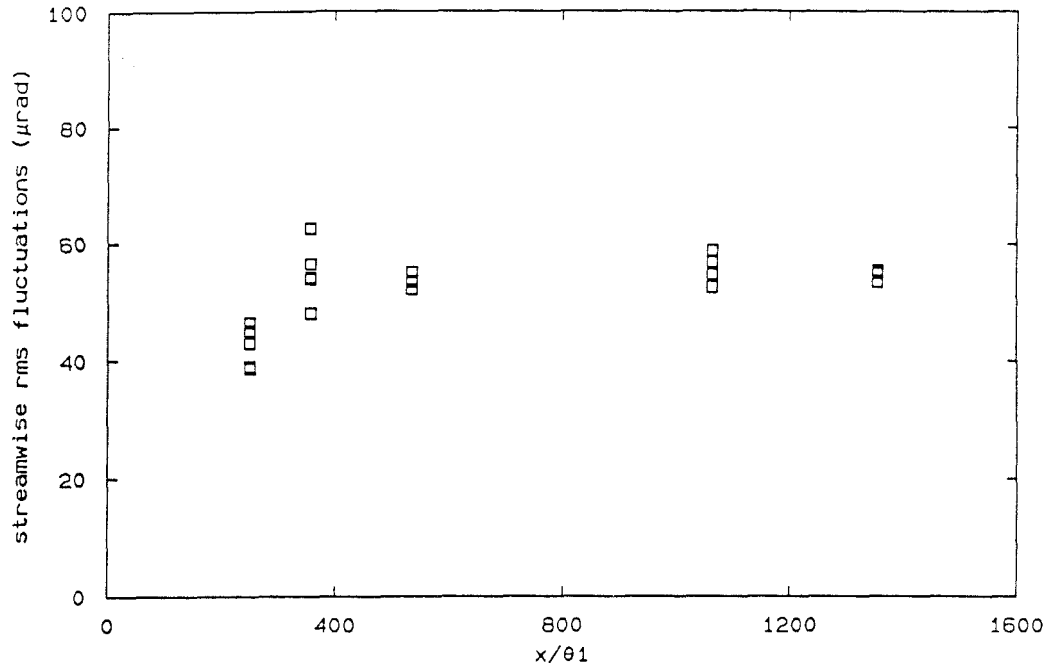

Figure 7.4–Streamwise rms Fluctuations vs x/θ_1 $(N_2/He\text{-}Ar)$.

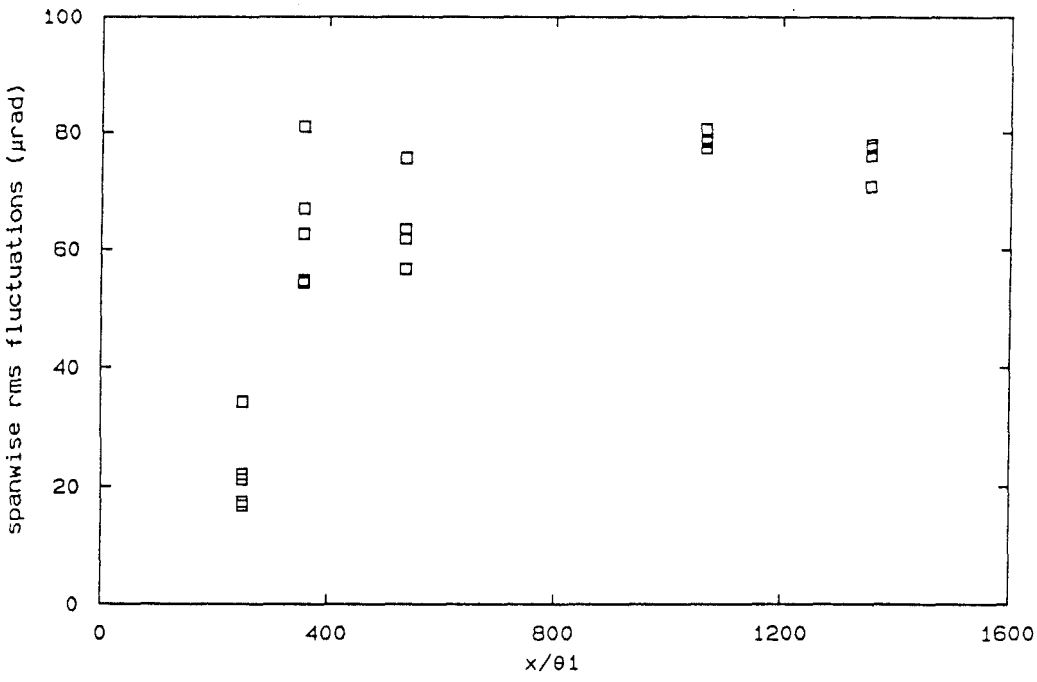

Figure 7.5–Spanwise rms Fluctuations vs x/θ_1 $(N_2/He\text{-}Ar)$.

a)

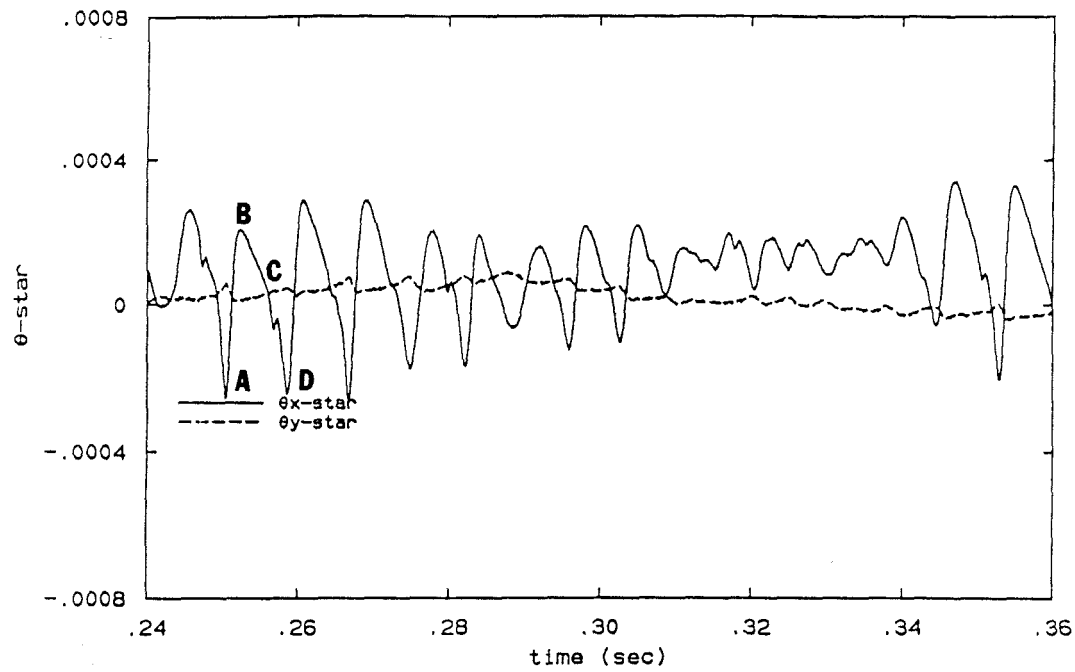

b)

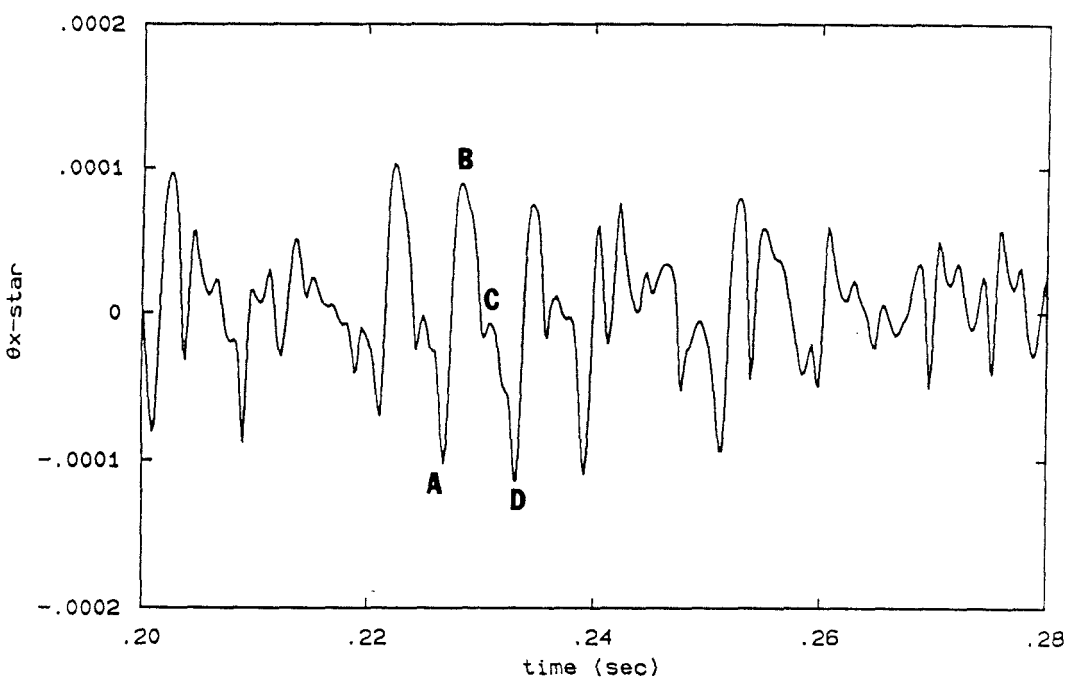

Figure 8.1–Comparison of deflection data for (a) unequal density (b) equal density (flipped) mixing layers.

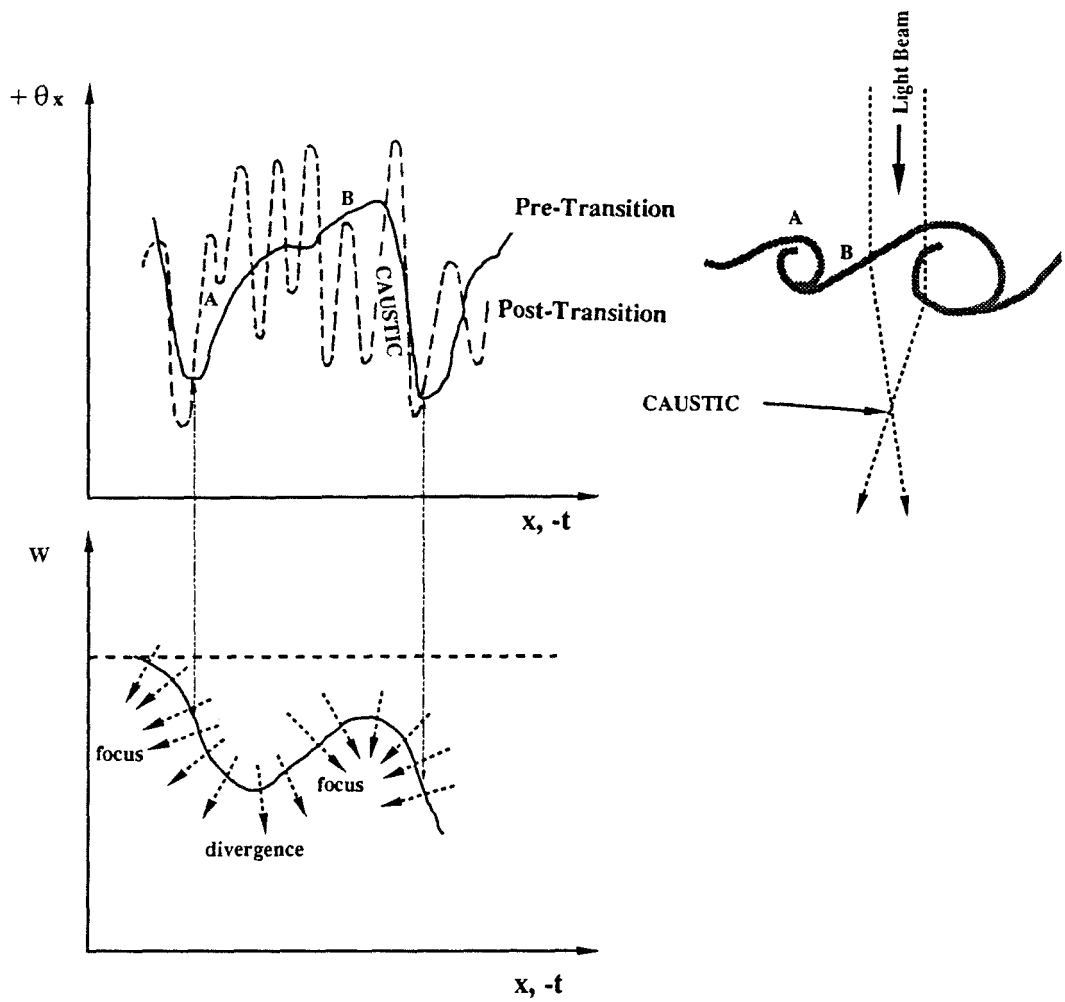

Figure 8.2–Model of spanwise coherent structure effect on a thin light beam ($\Delta\beta > 0$).

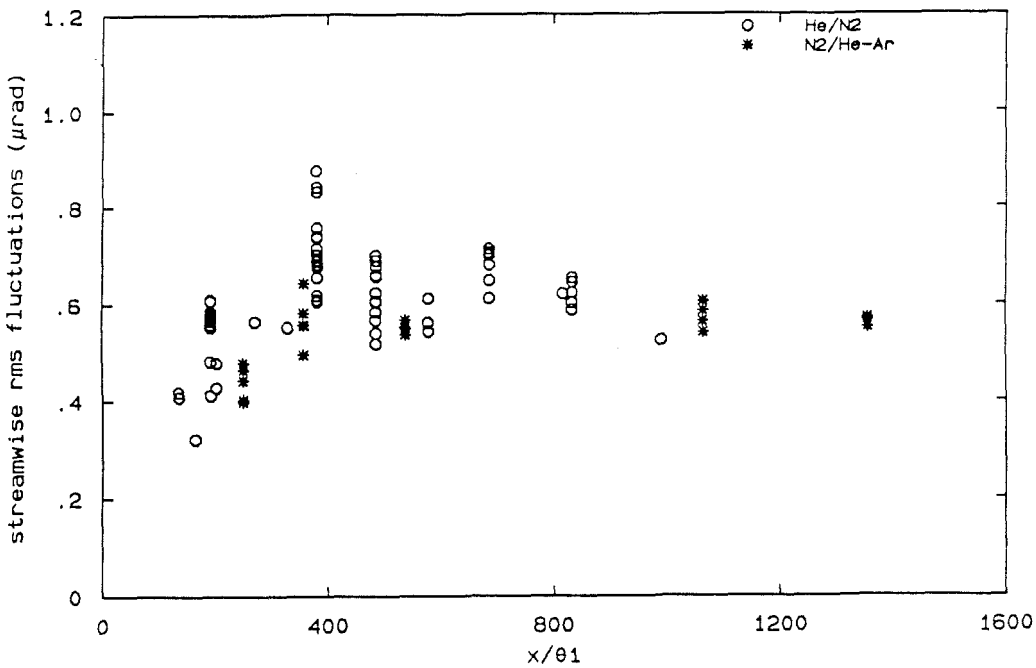

Figure 8.3–Scaled Streamwise rms Fluctuations vs x/θ_1.

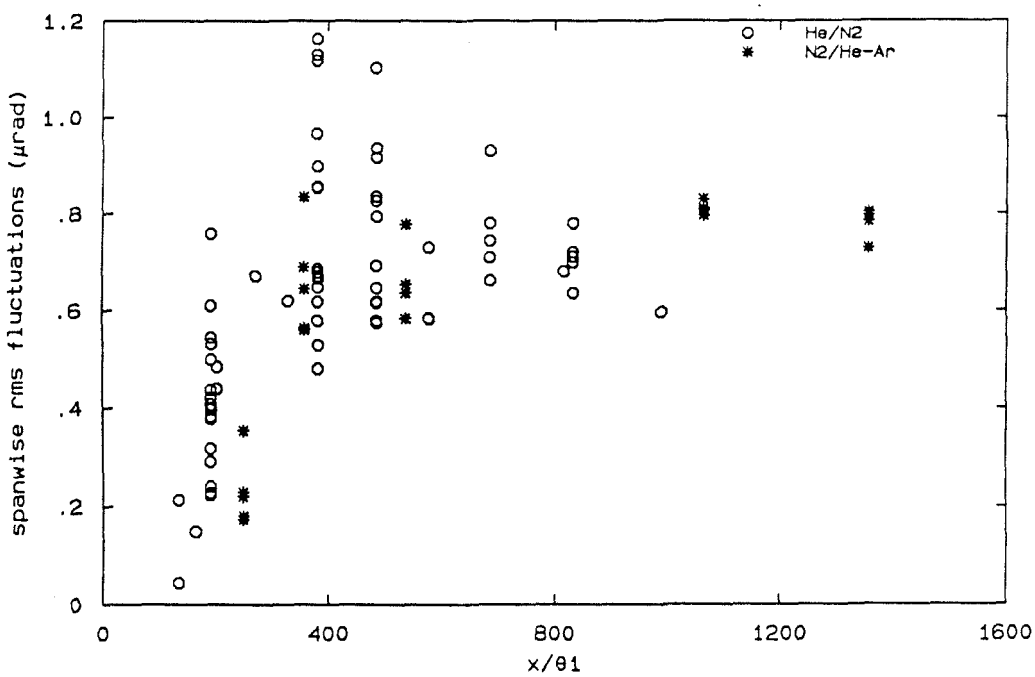

Figure 8.4–Scaled Spanwise rms Fluctuations vs x/θ_1.

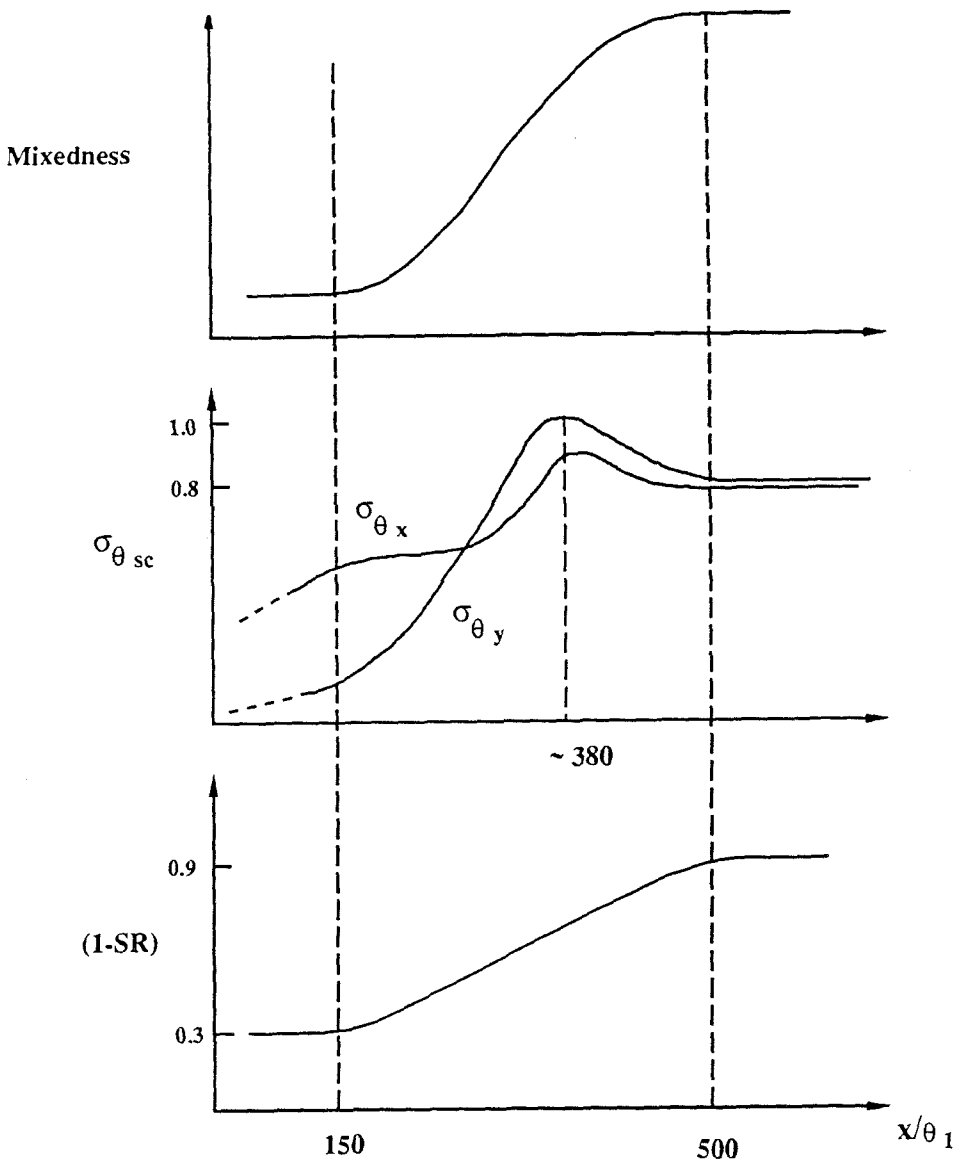

Figure 8.5–Comparison of Mixing, Transmission and Intensity (SR) Transitions.